IJCOE
COASTAL, OFFSHORE AND ENVIRONMENTAL ENGINEERING

Volume 10 | Isssue 4| Nov 2025

WWW.IJCOE.org info@ijcoe.org

www.ijcoe.org

International Journal of Coastal, Offshore and Environmental Engineering (IJCOE) Vol.10/Issue 4/ Nov 2025

International Journal of Coastal, Offshore & Environmental Engineering

Volume 10 | Issue4 | Aug 2025

IJCOE

International Journal of Coastal, Offshore & Environmental Engineering
Since 2015
ISSN: 2980-8721 (online)

In The Name of God

Message from the Editor-in-Chief

The IJCOE journal office was established in 2015,and its first issue was published in 2016. TheIJCOE covers a wide range of research in thefields of oceanography & ocean technology, aswell as marine industries & marine engineering.The editorial board of IJCOE consists of nearly130 of the greatest scientists and researchersfrom over 30 countries worldwide, and thejournal's review board comprises 1,000 membersfrom all five continents. The membership andapplication process for joining the editorial andreview boards of this journal is ongoing. IJCOE isa research-academic quarterly journal that haspublication and distribution permissions fromthe Press Organization and permission topublish scientific-research articles from theMinistry of Science, Research, and Technology(MSRT) with an "A" rating. It also holds a "Q1"rating from the ISC institute with an impactfactor (IF) of approximately 0.43 and isconsidered a "core journal" (prestigious andoutstanding journal). IJCOE is an open-accessjournal and allows the download and receipt ofaccepted articles in full text for free. It respectsand adheres to copyright and COPE regulations.The journal's office operates 24/7, providingservices to researchers. In addition to publishinga regular quarterly journal, IJCOE has 16 specialissues on specific topics in preparation. It alsoprovides conditions for publishing specializedbooks, references, and handbooks. Moreover, itis ready to cooperate with the secretariats ofreputable international conferences to publishtheir selected and outstanding articles. IJCOEevaluates, appraises, and publishes books,articles, and the scientific achievements andfindings of esteemed researchers and scientistsworldwide who are innovating and conductingin-depth research in the "important and strategicfield of the maritime technology & Oceanengineering." It welcomes any form of jointcooperation with universities, research institutes,and related research centers at the national,regional, and international levels, and extends ahand for collaboration.

Classification of Editorial Board in IJCOE

- Editor-in-Chief
- Director-in-Chief
- Deputy Editor
- Executive Managers
- English Text Editor
- Technical Editor
- International Editorial Board
- National Editorial Board
- Editorial Board Associate
- Editorial Board Assistant
- Guest Editorial Board
- Advisory Board
- Administrative Coordinator
- Honorary Board Member
- Methodology Advisor

Author Benefits

- Open Access
- Rapid Publication
- Thorough Peer-Review
- No Copyright Constraints
- Coverage by Leading Indexing Services
- Discounts On Article Processing Charges (APC)
- No Space Constraints, No restriction on the maximum length of the papers, number of figures or colors

INTERNATIONAL JOURNAL OF IJCOE COASTAL, OFFSHORE & ENVIRONMENTAL ENGINEERING

Aims of IJCOE

Hydrodynamics

Marine equipment

Structural mechanics

Ocean environmental predictions

Stochastic calculations Experimental

Automatic Control of Marine Systems

Scope of IJCOE

Marine Hazards

Ocean Acoustics

Naval Architecture

Ocean Engineering

Coastal Engineering

Marine Meteorology

Marine Earth Sciences

Underwater Technology

Marine Renewable Energy

Polar & Arctic Engineering

Marine Renewable Energy

Marine Geography & Geodesy

Marine Environmental Engineering

Automatic Control of Marine Systems

Hydro Physics & Physical Oceanography

Type of papers

- Case Studies
- Book Reviews
- Review Article
- Letters to the Editor
- Methodology Papers
- Editorials and Commentaries
- Response or Rejoinder Papers
- Perspective or Opinion Papers
- Conceptual or Theoretical Papers
- Meta-Analysis and Systematic Reviews
- Short Communications or Brief Reports
- Research Articles (Original Research Papers)

Scientific Research Journal

Ministry of Science, Research And Technology (MSRT)

Jurnal Ranking 2023: A

Ministry Of Science, Research And Technology (ISC)

Citation Impact 2022: 0.429

Quartile 2022 : Q1

Core Collection

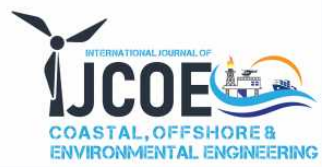

IJCOE is a Member of

Cantact Us

Office 1 | Research Institute of Meteorology and Atmospheric Science

Address | Tehran, Shahid Kharrazi Highway, Pajoohesh Blvd, Research Institute of Meteorology and Atmospheric Science, Sand and Dust Storm International Research Center (SDS-IRC), No. 13, 1st floor.

Phone | +982144787652

Postal code | 13611-14977

website | www.rimac.ac.ir

Office 2 | Iranian National Institute for Oceanography and Atmospheric Science

Address | Tehran, Dr. Fatemi Gharbi St., Shahid Etemadzade St., No. 3, third floor.

Phone | +982166944873

Postal code | 13389 – 14118

website | www.inio.ac.ir

Email | Info@ijcoe.org

Website | www.ijcoe.org

Follow Us

www.ijcoe.org

INTERNATIONAL JOURNAL OF IJCOE COASTAL, OFFSHORE & ENVIRONMENTAL ENGINEERING

Volume & Issue:

Volume 10, Issue 4, Nov 2025

Number of Articles: 6

Content

IJCOE
COASTAL, OFFSHORE & ENVIRONMENTAL ENGINEERING

INTERNATIONAL JOURNAL OF
COASTAL, OFFSHORE & ENVIRONMENTAL ENGINEERING IJCOE Vol.10/No. 4/Autumn 2025 (1-7)

Available online at: www. Ijcoe.org

Interaction of the Breaking and Non-Breaking Solitary Waves and Linear and Nonlinear Slopes Sea Bed by SPH Method

Amin Fathi[1], Cyrus Ershadi[2*]

[1] *a)Assistant Professor, Faculty of Civil Engineering, Hormozgan University, Bandar Abbas , Iran*

E-mail: aminfathi@hormozgan.ac.ir

[2*] *b) Associate Professor, Faculty of Civil Engineering, Hormozgan University, Bandar Abbas , Iran*

Email address: cyrusershadi1@yahoo.co.uk

ARTICLE INFO

Article History:
Received : 21 Mar 2025
Accepted : 30 Dec 2025

Keywords:
linear and nonlinear slopes, solitary waves, fission law, breaking wave, SPH method

ABSTRACT

Investigating solitary waves is critical for predicting the tsunami waves features in the coastal region. The Smooth Particle Hydrodynamic method (SPH) is the Lagrangian meshless method that is commonly used to simulate nonlinear waves and free surface problems. In this study, the SPH method is used to investigate the propagation of the breaking and non-breaking solitary waves over the linear and nonlinear sharp slopes sea bed. The presented SPH model is validated in comparing the experimental and another numerical model. The results show that the presented method prepares powerful tools to simulate the solitary wave propagation over the variable sea bed. Then, the transmitted solitary wave from the linear and nonlinear sharp slopes of the sea bed were compared. The results show that the solitary wave energy loss for waves propagating through the linear slopes is more than that of non-linear slopes. Moreover, the solitary wave transmission coefficient increases with increases in wave height in the linear and nonlinear slope. Also, the transmitted solitary wave height through the nonlinear slope is slightly more than the linear slope. Finally, the breaking Solitary waves when passing through the variable depth in the near shore with nonlinear slopes is investigated by comparing the wave free surface, streamlines, and orbital velocities before and after wave breaking. The results show that the solitary wave horizontal orbital velocity values after the wave breaking are increasing in comparison with before breaking.

1. Introduction

The tsunami is generated after the rapid scale-up turbulence of a volume of ocean water due to underwater disturbances like underwater earthquakes, landslides, and volcanic eruptions. The long waves with small amplitudes (usually less than 1 m of height and more than 100 kilometers of the wavelengths) are formed in the deep ocean water due to underwater disturbance. When this mass of water moves toward the coast, the waves height increases as the water depth decreases near the coast. These massive and dangerous long waves have caused many financial and fatality consequences in coastal regions. For example, the tsunami of 2004 in India with more than 230,000 dead, and the tsunami of 2011 in Japan with more than 20,000 dead and 360 billion dollars in financial consequences can be reviewed [1].

Since the surface profile of a tsunami is similar to that of solitary long waves, these waves have been widely used to simulate and study the physical behavior of tsunami waves in detail since the 1970s. In this regard, the solitary wave are used to study the tsunami run-up on the coastal slope (Di Risio et al., 2009 [2]; Knowles and Yeh, 2018 [3]; Ershadi, et al., 2019 [4]), the interaction between tsunami waves and structures (Fathi and Ketabdari, 2018 [5]; Ko and Yeh[6], 2019; Jensen, 2019 [7]; Vinodh and Tanaka, 2020 [8]; Wei et al., 2021 [9]; lin et al., 2023 [10]), and coastal sediment and morphology (Xiao et al., 2010 [11]; Li et al., 2019 [12]). It should be noted that there are some dissimilarities between the solitary and real tsunami waves in shallow water were noted by Madsen et al. 2008 [13], and Qu et al.[14].

When a solitary wave propagates in shallow water with a variable sea bed, several critical phenomena occur. Some of the solitary wave's energy is reflected, and some is lost due to friction on the seabed. Also, the remainder of wave energy pass over the seabed slope

or underwater obstacles [Liu et al, 1991 [15]; Vaziri et al., 2011 [16]; Papoutsellis et al., 2018 [17]]. Moreover, as solitary waves pass over the variable seabed, small solitary waves are formed from the original wave, which is called the fission phenomenon. Understanding wave fission is important for predicting how waves will behave in shallow or variable-depth waters, which has implications for coastal engineering, marine navigation, and tsunami modeling. So far, many studies have been done on the solitary waves propagating through the variable bed some of which are mentioned below.

Seabra-Santon et al., 1987 investigated the interaction of solitary waves with a varying seabed using the finite difference method in conjunction with the shallow water equations. They compared the numerical results with experimental data [18]. Sriram et al. (2006) studied the same problem (Seabra-Santon et al. study) using the finite element method by solving the nonlinear potential theory [19]. Chowdhury and Sannasiraj (2013) simulated the propagation of solitary waves over both constant and varying seabeds using the SPH method [20]. They showed that the solitary waves split into several solitons when crossing the continental shelf. Tan et al., 2019 presented a numerical model to predict the number and amplitudes of the disintegrated solitons of solitary waves propagating over a step [21]. They also compared the numerical results with the experimental data from Seabra-Santon et al., 1987. Chao et al., 2021 prepared an experimental setup to study the interactions of solitary waves with a Submerged Step using the image-connection technique. They investigated the effect of changing the step height and solitary wave height of the transmission wave features [22]. Fang et al., 2022 studied the interaction of solitary waves and complex bathymetries with the different linear slopes [23]. They showed that two-layer Boussinesq model is a powerful tool for modeling the solitary wave propagation and transformation over the linear sea bed. Lin et al., 2023 prepared laboratory experiments to investigate the breaking of solitary waves propagating through submarine canyons [10]. They used a combination of particle image velocimetry and planar laser-induced fluorescence techniques to measure the free surface solitary wave data.

The extensive literature review presented above shows that so far no numerical or experimental studies have focused on the interaction of solitary waves with nonlinear slope variable seabed depth. In this study, the interaction of the generated solitary waves in NTW using the SPH method and the linear and nonlinear sea bed slopes. After explaining the theoretical formulation of the SPH method in Sec. 2, the presented SPH model is validated in comparing the experimental and another numerical model. Additionally, the solitary wave generated using the SPH method is validated by comparing it with the Boussinesq solitary wave equation. The results demonstrate that the presented SPH model accurately simulates solitary wave propagation through a variable seabed. After model validation, the interaction between the transmitted solitary wave and linear and nonlinear seabed slopes is investigated. The effect of the non-breaking solitary wave height (H) on the wave transmission coefficient (Ct) after propagating through the linear and nonlinear slopes is also studied. Finally, the phenomenon of solitary wave breaking on the nonlinear slope when passing through variable depth in the nearshore region is examined. Streamline and orbital velocities before and after wave breaking are also compared.

2. Smoothed Particle Hydrodynamics method

2.1. Kernel function

The basin equation in the Smoothed Particle Hydrodynamics method for each variable A(r) is shown as follows:

$$A(r) = \int A(r')W(r - r', h)dr' \quad (1)$$

Where, r and r' represent the location of the main and neighboring particles respectively, h is the effective radius of the neighboring particles, and $W(r - r', h)$ is the kernel function that is used to interpolate between the neighboring particles. Several equations are suggested for kernel functions. In this study, the cubic spline function was used, which is defined below:

$$W(r,h) = \begin{cases} \frac{10}{7\pi h^2}\left(1 - \frac{3}{2}q^2 - \frac{3}{4}q^3\right) & 0 < q < 1 \\ \frac{10}{28\pi h^2}(2-q)^3 & 1 < q < 2 \\ 0 & q > 2 \end{cases} \quad (2)$$

Where, q=r/h and $r = r_a - r'$ is the distance between particle a and its neighboring particles.

2.2. The conservation of the mass

The governing equations in the SPH method consist of the continuity and momentum equations as shown below [24]:

$$\frac{1}{\rho}\frac{\partial \rho}{\partial t} + \nabla . u = 0 \quad (3)$$

$$\frac{Du}{Dt} = -\frac{1}{\rho}\nabla P + g + v_0\nabla^2 u + \frac{1}{\rho}\nabla \tau \quad (4)$$

Where ρ is the density, u is the velocity, g = (0, 0, -9.81) is the gravity acceleration, P is the pressure and υ_0 is the kinematic viscosity and τ is the SPS stress tensor.

The discretized form of the above equations as shown below [25] , [26]:

$$\frac{d\rho_a}{dt} = \rho_a \sum_b \frac{m_b}{\rho_b} u_{ab} . \nabla W_{ab} \quad (5)$$

$$\frac{du_a}{dt} = g + \sum_b m_b \left(\frac{P_a}{{\rho_a}^2} + \frac{P_b}{{\rho_b}^2} + \frac{\tau_a}{{\rho_a}^2} + \frac{\tau_b}{{\rho_b}^2}\right) + \sum_b m_b \frac{4\upsilon_0 r \nabla_a W_{ab}}{(r_a + r_b)(|r_{ab}|^2 + \eta^2)} \quad (6)$$

where, $\eta^2 = 0.01 * h^2$, $u_{ab} = u_a - u_b$ is the velocity difference between the interpolation particle a and neighboring particle.

2.3. Equation of State

In this study, the fluid is considered weakly compressible. Therefore, the equation of state (EoS) is used to compute the pressure term ([27]).

$$P = B\left[\left(\frac{P}{\rho_0}\right)^{\gamma} - 1\right] \quad (7)$$

$$B = \frac{C_0 \rho_0}{\gamma} \quad (8)$$

Where B is the constant parameter which is related to Bulk module, $\gamma = 7$ is the polytropic constant and C_0 is the sound velocity in the reference density. It should be noted that c_0 is not the real speed of sound and this value is restricted to be at least 10 and maximum 40 times the maximum fluid value to ensure that the density variations are less than 1%.

2.4. XSPH Method

The Particles movement is modified by monaghan according to the following equation [28].

$$\frac{\partial r_a}{\partial t} = V_a + \varepsilon \sum_b \frac{m_b}{\overline{\rho}_{ab}} V_{ab} W_{ab} \quad (9)$$

In which, ρ_{ab} and u_{ab} is the density and the average velocity between a and b. also, ε is a constant parameter which is located between 0 and 1 and is considered 0.5.

2.5. Solitary wave generation

The solitary wave free surface is defined based on long wave theory on position x and time *t* as following:

$$\eta(x,t) = H sech^2\left[\sqrt{\frac{3H}{4d}}\,(x - ct)\right] \quad (10)$$

$$c = \sqrt{g(H_0 + d_0)} \quad (11)$$

Where, C is the solitary wave velocity, H is wave height, and d_0 is water depth.

The piston type wave-maker is used to generate a solitary wave in shallow water according to bellow equation [29].

$$x(t) = \frac{2H}{d_0 \beta} \frac{d_0 \tanh\left(\frac{\beta c(t-t_0)}{2}\right)}{d_0 + h(1 - \tanh^2\left(\frac{\beta c(t-t_0)}{2}\right))} \quad (12)$$

$$\beta = 2\sqrt{\frac{3H^3}{4{d_0}^2(H + d_0)}} \quad (13)$$

where, x is the position of the piston type wave maker at different times and β is the coefficient of boundary lag. Also, the speed of the wave paddle is obtained from the below equation:

$$u_{x,t} = \frac{\Delta x}{\Delta t} \quad (14)$$

It should be noted that the Wave Maker is modeled with zero speed and displacement particles in the SPH method.

3. Simulation of solitary wave in constant depth

In this section, the generated solitary wave is validated by the analytical Boussinesq equation. In this regard, the simulated wave flume in the SPH method is shown in Fig. 1.

Fig. 1: The simulated wave flume in the SPH method to validate solitary wave generation

The simulated solitary wave free surface at locations, x = 5 and x = 8 is presented in Fig. 2. Also, the percentage difference between the SPH simulation and the Boussinesq equation are shown in Table 1. These results demonstrate that the solitary wave simulated using the SPH method shows good agreement with the Boussinesq equation. Furthermore, Wave velocity based on the Boussinesq equation (Eq. (11)) and SPH method (C=Δx/Δt) are compared. The results indicate that the Wave velocity in Boussinesq models is equal to 1.469 m/s and in the SPH method is 1.473. Therefore, the proposed SPH method demonstrates sufficient accuracy in comparison with the Boussinesq theory.

Fig. 2: Validation of the generated solitary waves by SPH method in comparing Boussinesq models in, a: x = 5 m, b: x = 8 m.

3.2. Solitary wave validation when propagate through the sudden change in bed

When the solitary wave propagates in shallow water with a variable bed, some parts of the solitary wave energy are lost due to reflection and friction on the sea bed. Additionally, as the solitary waves pass over the variable bed, small solitary waves are formed behind the original wave, a phenomenon known as fission. The fission can affect wave energy distribution, which is crucial for designing coastal structures, predicting wave impact, and managing coastal erosion. Understanding how waves break up into smaller waves can help in predicting the behavior of tsunamis and storm surges as they approach shorelines with varying depths. In this section, the simulated solitary wave crossing the variable bed by the presented SPH method is validated against experimental data (Seabra santon et al, 1987 [18]) and compared with other SPH numerical results (Choudhary et al., 2013 [20]). The parameters used in the current SPH model are shown in Table 1.

Table 1: the Parameters used in the presented SPH simulating

Variable Description	Input data
Kernel	Cubic Spline
Time-Stepping Algorithm	Simplistic
Viscosity Treatment	Laminar+SPS
Equation of State	Tait
Box dimension (m)	20, 0.6
Particle spacing (m)	0.005, 0.005
CFL number	0.2

sound speed coefficient	20

The experimental wave flume used by Seabra Santon et al, with a length of 16 m, an initial water depth of 20 cm, a secondary water depth of 10 cm, and a solitary wave height of 3.65 cm, is shown in Fig. 3. The numerical wave set up by the presented SPH method is shown in Fig. 4. As depicted in this figure, several small solitary waves are formed as the main solitary wave propagates over the variable bed. Also, the solitary wave free surface generated by the presented SPH method is compared with the experimental results by Seabra Santon et al. (1987) and numerical SPH results by Choudhary et al. (2013) in Fig. 5. This comparison demonstrates that the presented SPH model achieves high accuracy in simulating solitary waves crossing a variable bed.

Fig. 3: The experimental wave flume used by Seabra santon et al.

Fig. 4: Simulating the solitary waves passing the variable bed using the presented SPH method

Fig. 5: comparing the presented results with the experimental results by Seabra Santon et al. (1987) and numerical SPH results by Choudhary et al. (2013)

4. Comparison of the solitary wave propagation through the curve and linear slope

In this section, the propagation of solitary waves over linear and nonlinear variable sea beds is compared. The simulated solitary waves and the corresponding wave flumes with linear and nonlinear slopes are illustrated in Fig. 6. The wave flumes have a total length of 10 m, with an initial water depth of 20 cm, a secondary water depth of 10 cm, and a solitary wave height of 4.5 cm.

Fig. 6: The simulated solitary wave passing through a: linear slope, b: nonlinear slope

The solitary wave free surface while passing over the linear and nonlinear slope beds is compared in Fig. 7. This figure indicates that the area below the passing solitary wave free surface over the nonlinear slope is slightly larger than that of the linear slope. Consequently, it can be concluded that wave energy loss for waves propagating over linear slopes is greater than for those propagating over nonlinear slopes. The orbital velocities in X direction at the solitary wave crest in X=2.5m and X=3m for the linear and nonlinear slops are compared in Fig. 8. It is observed that the orbital velocities at the solitary wave crest while passing over linear slopes are higher, indicating a greater likelihood of wave breaking on linear slopes compared to nonlinear slopes. The reason for this is that the wave's shoaling process is less abrupt compared to linear slopes. The depth changes more gradually, allowing the wave to adjust smoothly. Consequently, the increase in orbital velocities near the crest is less pronounced, as the wave's energy is distributed over a larger area. As a result, the likelihood of wave breaking is reduced compared to linear slopes

Fig. 7: Comparison the solitary wave free surface when passing through the linear and nonlinear slope

Fig. 8: The orbital velocities in X direction at the solitary wave crest a: X=2.5m, b: X=3m

4.1. The solitary wave transmission coefficient

In this section, the effect of the solitary waves height (H) on the wave transmission coefficient (Ct) after passing through the linear and nonlinear slops is investigated. Figure 9 and Table 2 illustrate the relationship between solitary wave height and the transmission coefficient. These results indicate that the transmission coefficient increases with increasing wave height for both linear and nonlinear slopes. This finding suggests that the impact of water depth variations on incident solitary waves diminishes as wave height increases. Additionally, Figure 9 demonstrates that the transmission coefficient for solitary waves passing over nonlinear slopes is slightly higher than for linear slopes. The interaction of the wave with a nonlinear slope can create complex boundary layer effects that might reduce energy dissipation compared to a linear slope. This reduction in dissipation can lead to a higher transmission coefficient. While, linear slopes might have simpler boundary layer interactions that result in slightly higher energy loss.

Table 2: The solitary wave effect on the transmission coefficient

d1 (cm)	H (m)	Ct for Linear slope	Ct for Nonlinear slope
20	6	.862	.874
20	8	.881	.892
20	9.5	.907	.922

Fig. 9: Comparison of the transmission coefficient of passing solitary wave through the linear and nonlinear slope

4.2. Breaking Solitary Wave with Changing Water Depth

Solitary waves break when the water depth decreases significantly due to changes in sea bed level. its study is essential for advancing our understanding of coastal processes, improving hazard prediction and mitigation, and designing sustainable coastal infrastructure. In this section, the phenomenon of breaking solitary waves on a nonlinear slope while passing through variable depths near the shore is investigated.

The wave flume used to simulate solitary wave breaking near the shore has a length of 10 m, an initial water depth of 50 cm, a secondary water depth of 10 cm, and a solitary wave height of 15 cm, as shown in Fig. 10. When the solitary wave propagates over steep slopes, parts of its energy are lost due to reflection, fission, and friction, while the remaining energy is dissipated during wave breaking. The solitary wave

free surface both before and after breaking is shown in Fig. 11.

Fig. 10: The simulated wave flume in SPH model

Fig. 11: The solitary wave free surface before and after wave breaking

To investigate the wave-breaking phenomenon more precisely, the streamlines and orbital velocities in the X and Y directions are studied before and after the breaking. In this regard, the streamlines before and after the breaking are compared in Fig. 12. It should be noted that the angle of the streamline arrow with horizontal axis $\alpha = \tan^{-1} u/v$ in where u and v are horizontal and vertical orbital velocities. The orbital velocities in the X and Y directions, studied before and after the break, are compared in Fig. 13 and Fig. 14, respectively. Figure 13 shows that the horizontal velocity at the solitary wave crest is at a maximum. Additionally, the horizontal velocity values of the solitary wave increase after wave breaking compared to before the break. It is due to energy redistribution, momentum transfer, wave transformation, and nonlinear interactions.

Fig. 12: The streamline solitary waves, a before wave breaking, b: after wave breaking

Fig. 13: The solitary waves orbital velocity in x direction, a: before wave breaking, b: after wave breaking

Fig. 14: The solitary waves orbital velocity in x direction, a: before wave breaking, b: after wave breaking

5. Conclusion

In this study, solitary waves were generated in a Numerical Tank Wave (NTW) using the SPH method to investigate their interaction with linear and nonlinear slope sea beds. The presented SPH model was validated by comparing the results with experimental data and other numerical models. Additionally, the generated solitary wave using the SPH method was validated by comparing it with the Boussinesq solitary wave equation. The results demonstrated that the presented method accurately simulates solitary waves propagating through variable sea beds. Subsequently, the transmitted solitary waves from linear and nonlinear sea bed slopes were compared. The effect of solitary wave height (H) on the wave transmission coefficient (Ct) after propagating through linear and nonlinear slopes was also investigated. Finally, the phenomenon of breaking solitary waves on nonlinear slopes, while passing through variable depths near the shore, was examined. Also, the streamlines and orbital velocities before and after solitary wave breaking were compared. The main results of this study are summarized as follows:

1) The solitary wave energy loss for waves propagating through linear slopes is greater than (about 3%) that for nonlinear slopes.
2) Since the orbital velocities at the solitary wave crest passing through the linear slopes are greater, the possibility of waves breaking on linear slopes is greater than the nonlinear slopes.
3) The transmission coefficient increases with increasing wave height in both linear and nonlinear slopes.
4) The transmission coefficient for solitary waves passing through nonlinear slopes is slightly higher (about 5%) than that for linear slopes.
5) The solitary wave horizontal velocity values after wave breaking increase (more than 60 %) compared to those before breaking.

6. References

1 Mimura, N., Yasuhara, K., Kawagoe, S., Yokoki, H., & Kazama, S. (2011). Damage from the Great East Japan Earthquake and Tsunami-a quick report. Mitigation and adaptation strategies for global change, 16, 803-818.

2 Di Risio, M., De Girolamo, P., Bellotti, G., Panizzo, A., Aristodemo, F., Molfetta, M. G., & Petrillo, A. F. (2009). Landslide-generated tsunamis runup at the coast of a conical island: New physical model experiments. Journal of Geophysical Research: Oceans, 114(C1).

3 Chao, W. T., Liang, S. J., Young, C. C., & Ting, C. L. (2021). Interactions of Solitary Wave with a Submerged Step: Experiments and Simulations. Water, 13(9), 1302.

4 Ershadi, C., Fathi, A., Sharifi, S., & Jafarzadeh, E. (2018). Run-up Estimation Due to Interaction Solitary Wave with Nonlinear Slope Beaches Using SPH Method. Journal of Oceanography, 9(35), 29-37.

5 Fathi, A., & Ketabdari, M. J. (2018). Modeling of emerged semi-circular breakwater performance against solitary waves using SPH method. Journal of the Brazilian Society of Mechanical Sciences and Engineering, 40(6), 290.

6 Ko, H. T. S., & Yeh, H. (2019). Solitary waves perturbed by a broad sill. Part 1. Propagation across the sill. Journal of Fluid Mechanics, 880, 916-934.

7 Jensen, A. (2019). Solitary wave impact on a vertical wall. European journal of mechanics-B/Fluids, 73, 69-74.

8 Vinodh, T. L. C., & Tanaka, N. (2020). A unified runup formula for solitary waves on a plane beach. Ocean Engineering, 216, 108038.

9 Chao, W. T., Liang, S. J., Young, C. C., & Ting, C. L. (2021). Interactions of Solitary Wave with a Submerged Step: Experiments and Simulations. Water, 13(9), 1302.

10 Lin, J., Hu, L., He, Y., Mao, H., Wu, G., Tian, Z., & Zhang, D. (2023). Verification of solitary wave numerical simulation and case study on interaction between solitary wave and semi-submerged structures based on SPH model. Frontiers in Marine Science, 10, 1324273.

11 Xiao, H., Young, Y. L., & Prévost, J. H. (2010). Hydro-and morpho-dynamic modeling of breaking solitary waves over a fine sand beach. Part II: Numerical simulation. Marine Geology, 269(3-4), 119-131.

12 Li, J., Qi, M., & Fuhrman, D. R. (2019). Numerical modeling of flow and morphology induced by a solitary wave on a sloping beach. Applied Ocean Research, 82, 259-273.

13 Madsen, P. A., Fuhrman, D. R., & Schäffer, H. A. (2008). On the solitary wave paradigm for tsunamis. Journal of Geophysical Research: Oceans, 113(C12).

14 Qu, K., Ren, X. Y., & Kraatz, S. (2017). Numerical investigation of tsunami-like wave hydrodynamic characteristics and its comparison with solitary wave. Applied Ocean Research, 63, 36-48.

15 Liu, P. L. F., Synolakis, C. E., & Yeh, H. H. (1991). Report on the international workshop on long-wave run-up. Journal of Fluid Mechanics, 229, 675-688.

16 Vaziri, N., Chern, M. J., & Borthwick, A. G. (2011). A pseudospectral σ-transformation model of solitary waves in a tank with uneven bed. Computers & fluids, 49(1), 197-202.

17 Papoutsellis, C. E., Charalampopoulos, A. G., & Athanassoulis, G. A. (2018). Implementation of a fully nonlinear Hamiltonian Coupled-Mode Theory, and application to solitary wave problems over bathymetry. European Journal of Mechanics-B/Fluids, 72, 199-224.

18 Seabra-Santos, F. J., Renouard, D. P., & Temperville, A. M. (1987). Numerical and experimental study of the transformation of a solitary wave over a shelf or isolated obstacle. Journal of Fluid Mechanics, 176, 117-134.

19 Sriram, V., Sannasiraj, S. A., & Sundar, V. (2006). NWF: propagation of tsunami and its interaction with continental shelf and vertical wall. Marine Geodesy, 29(3), 201-221.

20 De Chowdhury, S., & Sannasiraj, S. A. (2013, June). Numerical simulation of 2D wave impact pressure using SPH schemes. In ISOPE International Ocean and Polar Engineering Conference (pp. ISOPE-I). ISOPE.

21 Tan, D. L., Zhou, J. F., & Wang, X. (2020). Fission law of solitary waves propagating over sharply variable topography. Journal of Hydrodynamics, 32(4), 727-734.

22 Chao, W. T., Liang, S. J., Young, C. C., & Ting, C. L. (2021). Interactions of Solitary Wave with a Submerged Step: Experiments and Simulations. Water, 13(9), 1302.

23 Fang, K., Liu, Z., Wang, P., Wu, H., Sun, J., & Yin, J. (2022). Modeling solitary wave propagation and transformation over complex bathymetries using a two-layer Boussinesq model. Ocean Engineering, 265, 112549.

24 Monaghan, J. J. (1992). Smoothed particle hydrodynamics. In: Annual review of astronomy and astrophysics. Vol. 30 (A93-25826 09-90), p. 543-574., 30, 543-574.

25 Dalrymple, R. A., and Rogers, B. D. (2006). Numerical modeling of water waves with the SPH method. Coast. Eng. 53, 141–147. doi: 10.1016/j.coastaleng.2005.10.004

26 Cunningham, L. S., Pringgana, G., and Rogers, B. D. (2014). Tsunami wave and structure

interaction: an investigation with smoothed-particle hydrodynamics. Proc. Inst. Civ. En-Eng. 167, 126–138. doi: 10.1680/eacm.13.00028

27 Batchelor, G.K., (1973). An Introduction to Fluid Dynamics. Cambridge UK.

28 Monaghan, J. J. (1989). On the problem of penetration in particle methods. Journal of Computational physics, 82(1), 1-15.

29 Katell, G., & Eric, B. (2002). Accuracy of solitary wave generation by a piston wave maker. Journal of hydraulic research, 40(3), 321-331.

INTERNATIONAL JOURNAL OF
COASTAL, OFFSHORE & ENVIRONMENTAL ENGINEERING IJCOE Vol.10/No. 4/ Autumn 2025 (8-18)

Available online at: www. Ijcoe.org

Vibration Control of a Composite Panel Carrying Concentrated Masses Under Different Boundary Conditions

Mohsen Kouhi[1], Alireza Mojtahedi[2*], Mehran Dadashzadeh[1], Shabnam Ebrahimi[3]

[1] *Ph.D. candidate, Dept. of Water Resources Eng., Faculty of Civil Engineering, University of Tabriz, Iran.*
[2*] *Professor, Dept. of Water Resources Eng., Faculty of Civil Engineering, University of Tabriz, Iran.*
[3] *M.Sc., Dept. of Mechanical Eng., Sahand University of Technology, Tabriz, Iran*

ARTICLE INFO

Article History:
Received : 21 Mar 2025
Accepted : 25 Dec 2025

Keywords:
Composite panel
Vibration behavior
Concentrated mass effect
Updated FE model
Vibration control

ABSTRACT

Composite panels are commonly used structural forms in marine environments, subjected to complex dynamic loads and vibration forces due to harsh operational conditions. Understanding their vibrational behavior is crucial for ensuring structural reliability and performance. The presence of localized mass variations, such as concentrated masses from attached equipment or marine growth, significantly influences their dynamic response. This study investigates the impact of concentrated masses on the vibrational characteristics of a composite panel under fixed and pinned boundary conditions through comprehensive experimental and numerical analyses. A finite element (FE) model was developed and updated based on experimental modal analysis results. The findings reveal that the location and magnitude of concentrated masses play a critical role in altering mode shapes and reducing natural frequencies. The introduction of concentrated masses leads to a systematic frequency shift, with greater reductions observed for higher mass magnitudes. The validated FE model enables an extended parametric analysis, reducing the dependency on extensive experimental testing. These insights provide a foundation for optimizing vibration control strategies in composite marine structures, contributing to improved design methodologies for enhanced structural integrity and performance.

1. Introduction

Composite materials are engineered from two or more distinct constituents, each contributing unique properties to the final product. The resulting composite structure typically exhibits enhanced physical and mechanical characteristics compared to the individual components [1]. Composite materials have attracted significant interest in recent years and are now commonly considered a viable alternative to traditional materials like metals and wood. They have been vastly adopted in the marine industry over time [2,3]. The increasing utilization of composites can largely be attributed to the numerous advantages composites offer, such as high specific strength and stiffness, enhanced damage tolerance, as well as superior resistance to fatigue and corrosion. These advantages make them ideal for watercraft, submersibles, offshore structures, and other components used in marine construction [4,5].

One of the most common structural forms for composites is the panel type [6]. Composite panels serve as essential structural components across various engineering applications particularly in marine settings [7,8]. Depending on their intended use and taking into account their operation in harsh marine and offshore conditions, composite panels utilized in these applications might experience various dynamic and vibration forces [9]. Intense vibration can significantly impact the safety and reliability of these thin-walled structures. Therefore, evaluating the dynamic and vibrational properties of marine and offshore composite panels and assessing their behavior under vibration loads is very important and has become challenging for engineers [10].

In many engineering structures, particularly those of a panel-type design, local mass variations frequently appear as concentrated mass connections [11]. Concentrated masses may develop in marine and offshore structures because of the weight of detachable equipment utilized and, in certain situations, due to the accumulation of marine growth [12]. These concentrated masses can significantly impact the

structural behavior and vibration response under different loading conditions [13]. Mass is a critical factor influencing the dynamic characteristics and vibration behavior of the structures [14]. Alterations in the local mass distribution at specific locations within a structure can result in significant shifts in its natural frequencies. Consequently, variations in mass can substantially alter the behavior of the structure under vibrational loads, causing changes in the modal parameters and the overall vibration response [15]. This could lead to unexpected deformations that differ from those predicted during the design phase [16]. Furthermore, in the context of composite structures, which are often engineered to achieve specific performance metrics, the effects of local mass variations can be even more pronounced [17]. These materials are typically designed to optimize strength-to-weight ratios, stiffness, and other mechanical properties. Therefore, understanding how local mass variations affect vibration behavior is critical for ensuring that their performance aligns with design expectations and that they meet safety and functional requirements [18]. Chaubey et al. [19] conducted a study on the free vibration analysis of various types of laminated composite shells with concentrated mass by creating a finite element (FE) formulation that utilizes third-order shear deformation theory (TSDT). Yang and Oyadiji [20] studied delamination in composite beams, caused by concentrated mass loading which affects the variations in modal frequency. Eken et al. [21] formulated the dynamic stability of thin-walled composite beams in rotation with rigid bodies. Hossain et al. [22] investigated the vibrations of composite plates with concentrated mass, examining how varying amounts of concentrated mass and their locations affected the eigenfrequencies of the plates. Zhong et al. [23] studied the stability of rectangular composite plates subjected to an arbitrary mass, specifically analyzing how concentrated mass and its spatial distribution influenced the plate's frequency response. Mandal and Haldar [24] assessed the free vibrations of composite plates and panels featuring concentrated mass at the center, considering various boundary conditions. Vatin et al. [25] investigated the vibrations of a composite plate with concentrated masses in a nonlinear geometric context, exploring the effects of concentrated mass values, their locations, property variations of the composite materials, and other parameters on the frequency response of vibrations.

This study investigates the influence of concentrated masses on the dynamic behavior and vibrational response of a composite panel under fixed and pinned boundary conditions. The primary objective is to examine how the location and magnitude of these masses affect mode shapes and natural frequencies, providing critical insights into vibration control strategies for composite structures. To achieve this, an integrated experimental and numerical approach was adopted. Experimental modal analysis was conducted to capture the vibrational characteristics of the panel under various mass configurations, while a FE model was developed and updated based on these results. The updated FE model was then employed to extend the parametric analysis, enabling a detailed assessment of frequency shifts and mode shape variations across different mass scenarios. Furthermore, the sensitivity of the panel's dynamic response to support conditions was analyzed, revealing distinct trends in frequency reduction and vibrational behavior alterations. The findings demonstrate that the positioning and magnitude of concentrated masses significantly impact the structural dynamics, leading to notable shifts in natural frequencies and mode deformation patterns. These insights contribute to the development of more effective vibration control methodologies, ultimately enhancing the structural performance and reliability of composite marine components.

2. Methodology

2.1. Modal Analysis and Experimental Tests

Modal analysis is a highly effective method for assessing and identifying the dynamic characteristics of a structure, such as natural frequencies, mode shapes, and damping ratios, and includes both theoretical and experimental techniques [26]. In recent years, with the trend towards designing structures with less weight and higher strength, modal analysis has gained a special place in vibration analysis and studying the dynamic behavior of various structures [27]. The main objective of modal analysis is to obtain more accurate dynamic characteristics of a structure using analytical, numerical, and experimental or combined methods. In this study, experimental and numerical modal analysis was used to investigate the effect of added concentrated masses on the vibration behavior and dynamic characteristics of a composite panel structure [28].

In order to perform experimental modal analysis, a physical model of the composite panel was fabricated using hand layup and vacuum bagging mold process. The materials selected and the method of fabrication were determined according to DNV guidelines and specifications for building composite structures intended for marine and offshore applications [29]. In the fabricated composite panel, woven glass fibers were used for the reinforcement phase and a mixture of polyester resin and hardener with a weight ratio of 70 and 30 for the matrix phase. To construct the model under study, 10 layers of glass fibers were used with the stacking sequence of $[0,90]_s$ to achieve a final thickness of 2 mm. The final dimensions of the composite panel after cutting were $750mm \times 800mm \times 2mm$.

There are several methods available for conducting modal testing, with the shaker test being the most widely used. In this approach, a shaker excites the structure using a specific signal, and the response of the structure is captured as time histories using sensors

such as accelerometers [30]. The frequency response functions (FRFs) are then derived by applying the fast Fourier transform to the recorded time history responses, allowing for the calculation of the structure's natural frequencies [31]. Since the modal parameters of the structure are influenced by mechanical characteristics like mass and stiffness, any alterations to these characteristics will lead to corresponding changes in the modal parameters [32,33].

To perform the experimental modal analysis, the physical model of the composite panel was excited by a shaker under both fixed and pinned support conditions. The excitation force applied to the model was a sinusoidal signal with a zero mean. Acceleration time history data were recorded at several points of the model using accelerometers. These data were transferred to the Pulse software for processing. The experimental modal analysis was conducted under two different scenarios to comprehensively assess the effects of concentrated masses on structural behavior. The first scenario involved the analysis without any added concentrated masses, allowing for a baseline understanding of the system's modal characteristics. The second scenario included alterations to the local mass by adding concentrated masses to evaluate their influence on the dynamic response of the structure. Furthermore, the analysis incorporated both fixed and pinned support conditions, which enabled a thorough investigation of how different boundary conditions affect the modal response. The vibrational response was measured at multiple points throughout the composite panel to establish a detailed representation of its dynamic performance under various test conditions. The concentrated masses were applied in the center of the panel with two weights of 100g and 200g. Figure 1 shows the overview and method of performing the experimental modal analysis, as well as the location of the excitation point, accelerometers, and added concentrated masses.

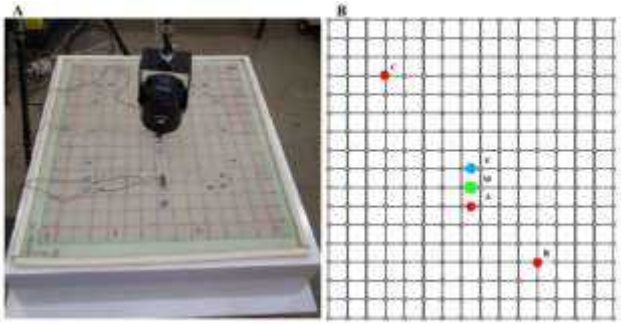

Figure 1. Experimental modal analysis: A) overview of the experimental test; B) location of excitation point, accelerometers, and added concentrated masses

The data obtained from the experimental modal analysis and pulse software processing for the composite panel were recorded as time history responses and FRFs. The required data were measured at three points A, B and C in the state of no added concentrated masses and with excitation at point E on the composite panel model. Then, by applying 100g and 200g weights at point M on the composite panel as concentrated masses, the response of the structure was also collected.

2.2. Finite Element Model of the Composite Panel

An FE model of the composite panel was developed using ABAQUS software, with similar geometry to the physical model, to ensure valid comparisons between simulated and experimental data (Figure 2). The model was designed with layered configurations to simulate the fiber orientations and stacking sequence. Pinned and fixed boundary conditions were applied to the model. A meshing strategy was employed that resulted in 6,375 quadrilateral elements, which were chosen to provide a balance between computational efficiency and the accuracy of the results.

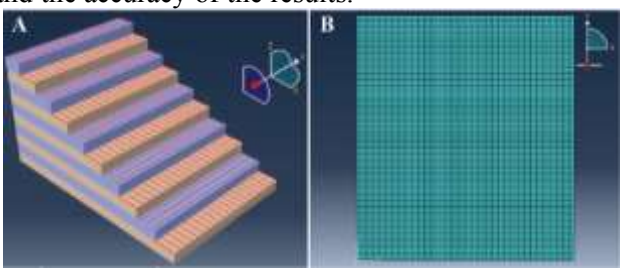

Figure 2. FE modeling of the composite panel via ABAQUS: A) Fibers orientation; B) Meshing

Material properties of the composite panel were obtained based on characteristics of the constituent material used in fabrication which are presented in Table 1. To calculate the material properties of the composite panel the rule of mixtures equations were used.

Table 1. Mechanical properties of the composite panel's constituent material

		Reinforcement phase		Matrix phase	
Material properties	**Unit**	**Symbol**	**Value**	**Symbol**	**value**
Elastic modulus	GPa	E_f	30.1	E_m	3.5
Poisson ratio	-	υ_f	0.2	υ_m	0.35
Shear modulus	GPa	G_f	10	G_m	2
Volume fraction	%	V_f	70	V_m	30

According to the rule of mixtures, the elastic modulus, shear modulus, and Poisson ratio can be calculated using these equations:

$$E_c = E_f V_f + E_m(1 - V_f) \quad (1)$$

$$G_c = \frac{G_f G_m}{G_m V_f + G_f V_m} \quad (2)$$

$$\upsilon_c = V_f \upsilon_f + V_m \upsilon_m \quad (3)$$

where E_c, G_c, and υ_c are the elastic modulus, shear modulus, and Poisson ratio of the composite, respectively. The equations used for predicting the mechanical properties of composites are well-documented and established, allowing for accurate

estimation based on the properties of the constituent materials [34]. This predictive capability is valuable for the design and optimization of composite materials in practical applications [35]. By employing these equations, it would be possible to assess the performance of composites without the need for extensive experimental testing, saving time and resources in the development phase. The estimated mechanical properties of the composite panel are outlined in Table 2. This information was used in the modeling of the composite panel.

Table 2. Mechanical properties of the composite panel

Material properties	Unit	Symbol	Value
Density	Kg/m^3	ρ	1500
Longitudinal Elastic Modulus	GPa	E_1	22.4
Transverse Elastic Modulus	GPa	E_2	22.4
Poisson ratio	-	υ_{12}	0.23
Shear Modulus in the 1-2 Plane	GPa	G_{12}	4.7
Shear Modulus in the 2-3 Plane	GPa	G_{23}	2.6
Shear Modulus in the 1-3 Plane	GPa	G_{13}	3.6

2.3. Numerical Modal Analysis

The numerical modal analysis process involves developing and refining a comprehensive mathematical model that effectively represents the structural system. This is achieved through the application of FE analysis, which enables the examination of the system's equations of motion under different boundary conditions and loadings [36]. For the model under investigation, numerical modal analysis was performed using ABAQUS software.

The primary goal of this analysis was to validate the FE model by calculating numerical frequencies and subsequently comparing these values with corresponding experimental results obtained through physical testing. This comparison is essential as it serves to highlight differences between the experimental and the predicted results. To enhance the accuracy of the FE model, modifications and updates were made based on the findings from this comparison, ensuring that the numerical model reflects a more realistic representation of the structural behavior. Given that conducting experimental modal analysis is costly and very time-consuming, particularly when dealing with different locations and magnitudes of concentrated masses applied to the model, the updated FE model was utilized to overcome these challenges. This approach not only simplified the analysis process but also enabled a comprehensive evaluation of the composite panel's behavior across a range of conditions, without the need for extensive physical testing.

3. Results and Discussion

Following the modal analysis, the impact of sensor positioning and support conditions on the quality and accuracy of the measured data was assessed using coherence functions. Figure 3 presents the coherence functions for the acceleration time history responses of the composite panel, evaluated under fixed and pinned support conditions at three locations: A, B, and C.

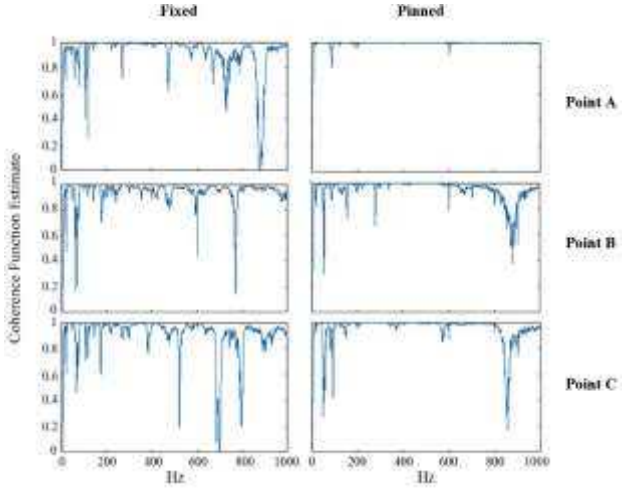

Figure 3. Coherence functions of acceleration time history responses of the composite panel

As illustrated in Figure 3, the coherence function tends to decay more significantly as the sensors are positioned farther from the excitation point and closer to the supports. This trend is attributed to the reduction in vibration amplitude at locations near the supports. Since the coherence function indicates the relationship between the response signal and the input excitation force signal, a decrease in amplitude and excitation strength results in the coherence value shifting from one to zero [26]. This phenomenon is distinctly evident in the presented coherence functions. Moreover, the decay in coherence is more pronounced under fixed support conditions, as the fixed support imposes greater restrictions on the amplitude of the excitation signal compared to the pinned support.

Based on the coherence functions, it can be concluded that positioning the sensor near the excitation point yields a more accurate and higher-quality response. Therefore, in the modal analysis of the composite panel with added concentrated masses, to achieve a more precise evaluation, the accelerometers were placed at point B, closer to the excitation point, to ensure the collection of higher-quality data. Figure 4 shows the coherence functions of the acceleration time history responses for the composite panel carrying concentrated masses at the center of the panel.

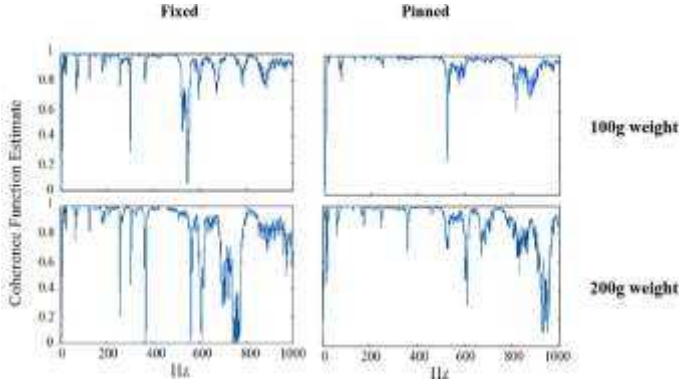

Figure 4. Coherence functions of acceleration time history responses of the composite panel carrying concentrated masses

According to Figure 4, it is evident that added masses result in coherence functions trending closer to zero. This decline indicates a reduction in the vibrational coherence of the system, suggesting that the added masses disrupt the energy distribution across the composite panel. Moreover, as the magnitude of these concentrated masses increases, the decay of the coherence functions becomes more pronounced, highlighting a more significant impact on vibrational behavior. To assess the impact of concentrated masses on the vibration behavior of the composite panel, the natural frequencies both with and without concentrated masses were calculated. Additionally, the analysis considered two different support conditions (fixed and pinned) to provide a more thorough understanding of how the support conditions affect the panel's vibration behavior. The results are summarized in Table 3.

Table 3. Natural frequencies resulted from experimental modal analysis (Hz)

Support condition	Mode	No mass	100g mass	200g mass
Fixed	1	35.5	33.42	28.66
	2	65	61.95	57.38
	3	73	70.46	66.94
	4	104	100.1	95.42
Pinned	1	21.3	18.23	16.87
	2	48.47	46.68	46.04
	3	55.56	54.36	53.68
	4	82.45	81.89	79.94

The natural frequencies of the numerical model were also calculated using the initial FE model without applying concentrated masses. The results of the numerical modal analysis were compared with the experimental findings to validate and assess the accuracy. The results of numerical modal analysis are presented in Table 4.

Table 4. Natural frequencies resulted from numerical modal analysis using initial FE model (Hz)

Support condition	Mode	No mass	100g mass	200g mass
Fixed	1	20.65	17.89	15.89
	2	38.74	38.51	38.33
	3	45.93	45.54	45.20
	4	59.72	59.65	57.39
Pinned	1	10.31	9.37	8.63
	2	24.89	24.12	23.94
	3	29.82	29.41	28.56
	4	41.24	41.23	41.14

As observed in Tables 3 and 4, there are notable differences between the experimental findings and the results obtained from numerical simulations. These differences arise primarily from the simplifications and assumptions made during the numerical modeling process, which may not fully capture the complexities of the actual behavior of the composite panel. To address these differences and enhance the accuracy of the analyses, the FE model of the composite panel was updated. This updated model incorporates more realistic parameters and refined assumptions to better align the simulation results with the experimental data. The calculated natural frequencies, as derived from this updated model, are summarized in Table 5, providing a clearer understanding of the dynamic characteristics of the composite panel. This updated model allows for improved predictive capabilities and a more reliable representation of the panel's behavior under various conditions.

Table 5. Natural frequencies resulted from numerical modal analysis using updated FE model (Hz)

Support condition	Mode	No mass	100g mass	200g mass
Fixed	1	35.35	28.74	24.77
	2	66.38	65.08	64.72
	3	78.98	76.34	75.64
	4	110	100.1	93.31
Pinned	1	20.13	17.17	15.15
	2	47.77	47.51	47.31
	3	56.53	56.10	55.73
	4	80.53	80.06	73.21

A thorough comparison of the frequencies obtained from the experimental modal analysis with those calculated using the updated numerical model demonstrates only a minimal discrepancy. This finding highlights the accuracy and reliability of the updated model. The enhanced model not only confirms the validity of the numerical results but also allows for a comprehensive evaluation of the composite panel's performance under a range of conditions. Importantly, this capability reduces the need for conducting numerous physical tests, enabling efficient analysis and insights into the behavior of the composite material across different scenarios and conditions.

In order to thoroughly evaluate the behavior of the composite panel carrying a concentrated mass and to achieve an insight into the vibration control of this type

of structure, its frequency responses were calculated under different conditions. The updated FE model was implemented for this purpose. In this regard, concentrated masses with different magnitudes in various locations on the composite panel were applied. The modal analysis was performed under fixed and pinned support conditions to obtain the natural frequencies and extract the mode shapes at each scenario. The positioning of the applied concentrated masses is illustrated in Figure 5. The arrangement of mass locations was selected in such a way as to enable the assessment of their influence both in proximity to the center of the plate and near the supports.

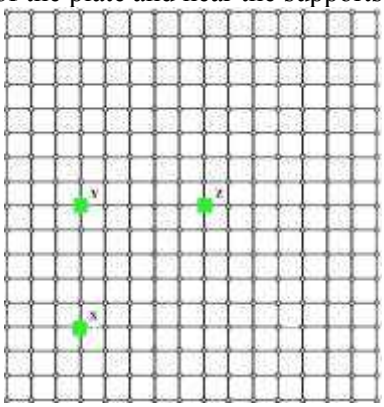

Figure 5. Schematic illustration of the positioning of concentrated masses in the updated FE model

Concentrated masses with different magnitudes were applied to the numerical model using the inertia tool in ABAQUS by defining point mass on the specified locations of the composite panel model. Subsequent to the selection of the required set, the ABAQUS solver was used to perform the numerical modal analysis with various conditions of concentrated masses locations and magnitudes. The frequency responses and mode shapes were derived for each condition. Mode shapes of the composite panel carrying concentrated masses are presented in Table 6 and Table 7 under fixed and pinned support conditions, respectively.

Table 6. Mode shapes and natural frequencies of the model carrying concentrated mass under fixed support condition

Concentrated mass condition	Mode 1		Mode 2		Mode 3		Mode 4	
	Mode shape	Frequency (Hz)	Mode shape	Frequency (Hz)	Mode shape	Frequency (Hz)	Mode shape	Frequency (Hz)
No concentrated mass	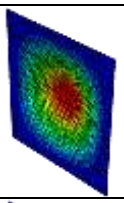	34.93	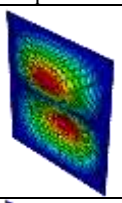	65.6	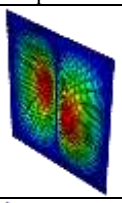	77.22	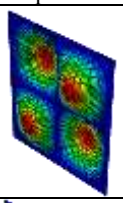	102.52
100g concentrated mass at point A	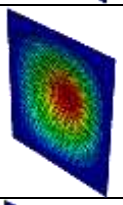	34.77	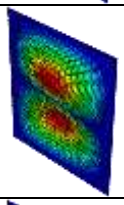	63.48	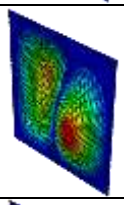	74.8	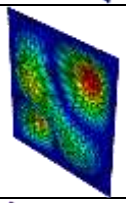	89.68
200g concentrated mass at point A	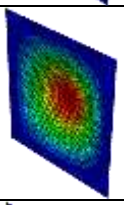	34.56	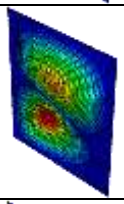	58.18	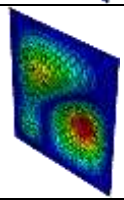	71.14	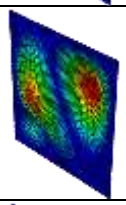	82.68
100g concentrated mass at point B	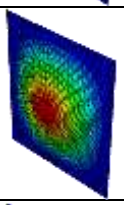	33.52	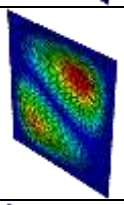	64.74	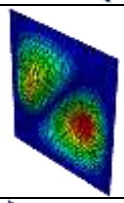	67.06	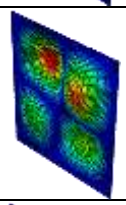	101.26
200g concentrated mass at point B	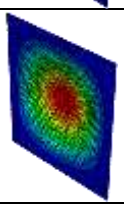	31.91	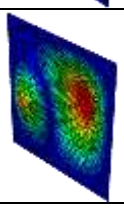	57.73	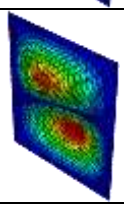	65.86	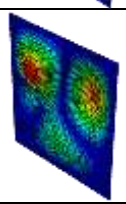	98.54

100g concentrated mass at point C	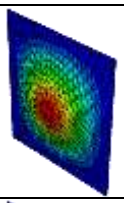	28.74	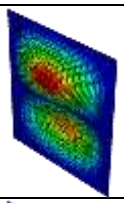	65.08	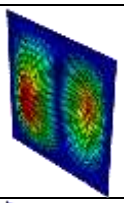	76.34	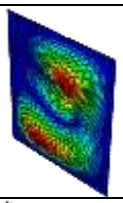	100.1
200g concentrated mass at point C	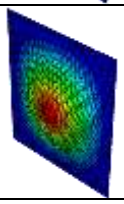	24.77	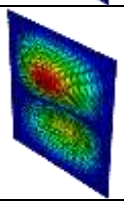	64.72	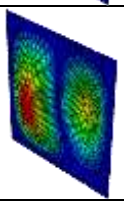	75.64	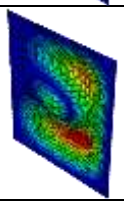	90.3

Table 7. Mode shapes and natural frequencies of the model carrying concentrated mass under pinned support condition

Concentrated mass condition	**Mode 1**		**Mode 2**		**Mode 3**		**Mode 4**	
	Mode shape	Frequency (Hz)	Mode shape	Frequency (Hz)	Mode shape	Frequency (Hz)	Mode shape	Frequency (Hz)
No concentrated mass	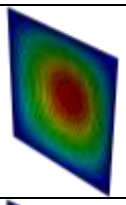	20.13	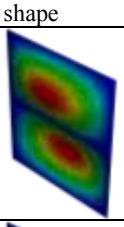	47.77	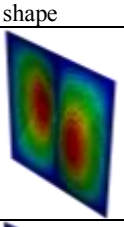	56.53	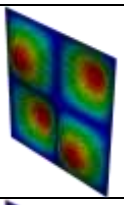	80.53
100g mass at A	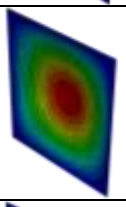	19.75	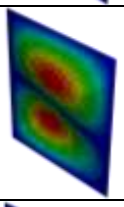	43.99	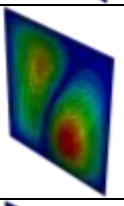	53.96	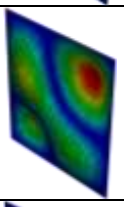	69.92
200g mass at A	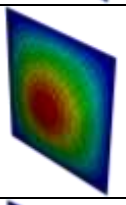	19.32	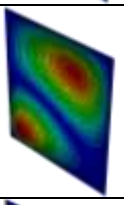	39.19	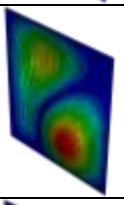	52.61	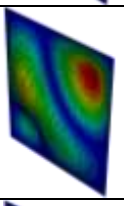	65.79
100g mass at B	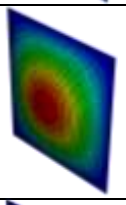	18.88	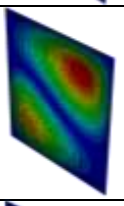	47.1	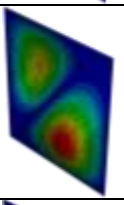	48.83	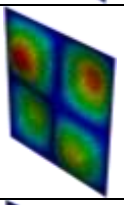	79.94
200g mass at B	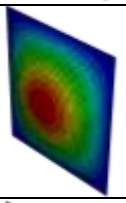	17.7	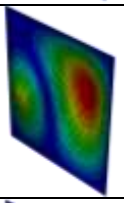	42.71	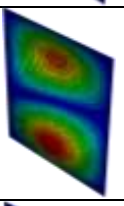	47.99	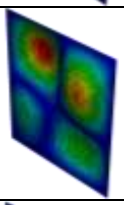	79.06
100g mass at C	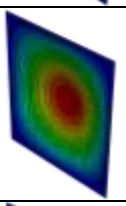	17.17	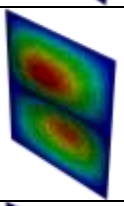	47.51	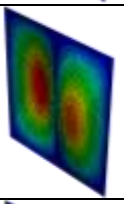	56.1	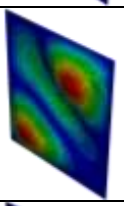	80.06
200g mass at C	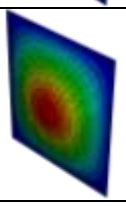	15.15	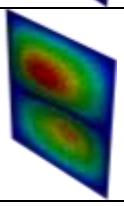	47.31	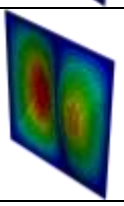	55.73	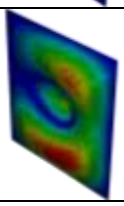	73.21

The mode shapes and natural frequencies of the composite panel without any added concentrated masses were derived. These data were used to establish a baseline for subsequent comparative analysis. These

mode shapes, along with their corresponding natural frequencies, are inherent to the material properties of the composite panel and its boundary conditions. To evaluate the sensitivity of these modal parameters to added concentrated masses at various locations with different magnitudes on the composite panel, the resultant frequency variations were calculated. The frequency variations of the composite panel induced by the applied concentrated masses are listed in Table 8 and Table 9 for fixed and pinned support conditions, respectively.

Table 8. Frequency variations under fixed support condition

Concentrated mass condition	Mode 1	Mode 2	Mode 3	Mode 4
100g mass at A	0.16	2.12	2.42	12.84
200g mass at A	0.36	7.43	6.10	19.83
100g mass at B	1.40	4.86	10.16	2.26
200g mass at B	3.02	7.87	11.36	3.98
100g mass at C	6.18	0.52	0.87	2.42
200g mass at C	10.15	0.88	1.58	9.22

Table 9. Frequency variations under pinned support condition

Concentrated mass condition	Mode 1	Mode 2	Mode 3	Mode 4
100g mass at A	0.38	3.78	2.57	10.61
200g mass at A	0.81	8.58	3.92	14.74
100g mass at B	1.25	0.67	7.7	0.59
200g mass at B	2.43	5.06	8.54	1.47
100g mass at C	2.96	0.26	0.43	0.47
200g mass at C	4.98	0.46	0.8	7.32

The mode shapes and frequency variations of the composite plate were analyzed under both fixed and pinned support conditions, revealing significant impacts of concentrated masses on the panel's vibration characteristics. Adding 100 and 200 grams of weight at various points (X, Y, and Z) alters these mode shapes, with noticeable decreases in natural frequencies.

For fixed support, concentrated masses at point X (near the corner) introduce localized stiffness, slightly reducing lower modes' frequencies and effectively damping higher-frequency vibrations. By increasing the weight of the concentrated mass at this point, the effect on the mode shapes was more pronounced. The additional mass further reduces the natural frequencies, particularly for modes with deformation near the corner. At this point, mode four frequency reduction and mode shape variation were the most. At point Y, added concentrated masses influence the global stiffness and inertia of the plate. This causes a more uniform shift in the mode shapes, affecting both lower and higher modes. Higher frequency reductions are observed for Mode three. Weights at point Z (center) cause reductions in natural frequencies across all modes. The central mass primarily affects the fundamental mode, leading to a noticeable decrease in the natural frequency. Since the concentrated mass was located at the center of the plate, mode one and mode four experienced the most reduction in frequency. By increasing the weight, mode shape variations were more pronounced, particularly at mode four.

Pinned support conditions, allowing rotational freedom, show a similar trend but with generally less pronounced effects. Frequency variations confirm these observations: added masses decrease natural frequencies, with point X significantly affecting higher modes, while points Y and Z influence both lower and higher modes with more impact on lower modes.

The magnitude and location of concentrated masses have a substantial impact on the composite plate's natural frequencies and mode shapes. For instance, the closer the mass is to the center, the greater the reduction in the first mode's frequency, indicating a critical sensitivity to central loading. Higher mass values further decrease frequencies, emphasizing the cumulative effect of mass and location on the plate's vibration characteristics.

Adding weights at different points on the panel demonstrates that localized mass can effectively alter the vibration characteristics. Points closer to the corner (X) show localized damping effects, reducing higher-frequency vibrations more effectively. Weights added near the center (Y and Z) influence the global stiffness and inertia of the plate, leading to a more uniform reduction in natural frequencies and effective damping across all modes. For effective vibration control, the distribution of added masses can be optimized based on the desired damping effects. Central masses provide more uniform damping, while localized masses can target specific higher-frequency modes. Different modes react differently to mass placement and support conditions. For instance, Mode four is highly sensitive to corner placements (Point X) under fixed support, while lower modes are more affected by central placements (Point Z). This allows for targeted vibration control strategies based on mode sensitivity. The support condition (fixed vs. pinned) alters the frequency response characteristics. Fixed support conditions generally show higher frequency values compared to pinned, implying that the stiffness of the support condition plays a crucial role in determining the vibrational behavior.

4. Conclusion

This study provides a comprehensive investigation into the effects of concentrated masses on the dynamic response and vibration control of composite panels under varying boundary conditions. The findings underscore the critical role of sensor placement and support conditions in ensuring the accuracy and reliability of modal analysis data. Coherence function analysis reveals that the decay in coherence is more pronounced when sensors are positioned further from the excitation point and closer to the supports, with this

effect being particularly significant under fixed support conditions. These observations highlight the necessity of optimal sensor positioning to enhance measurement precision in experimental modal analysis. Furthermore, the introduction of concentrated masses leads to a systematic decay in coherence functions, with higher mass magnitudes exacerbating this effect, further influencing the panel's vibrational response.

A comparative assessment of experimental and numerical modal analysis results identifies discrepancies arising from the inherent simplifications in numerical modeling. To address these inconsistencies, the finite element (FE) model was updated, incorporating more realistic parameters that better align with experimental observations. The updated FE model demonstrates strong agreement with experimental results, validating its accuracy and reliability. This enhancement not only improves predictive capabilities but also minimizes the dependency on extensive physical testing, offering a cost-effective and efficient approach for evaluating the vibrational characteristics of composite structures.

The study also highlights the significant influence of concentrated mass location and magnitude on the modal characteristics of the composite panel. Masses positioned near the center induce substantial reductions in natural frequencies, particularly affecting lower-order modes, while those placed near the edges exhibit a localized stiffening effect, altering higher-mode vibrations. Additionally, fixed support conditions yield higher natural frequency values compared to pinned supports, reinforcing the crucial role of boundary constraints in governing vibrational behavior.

These findings have important implications for vibration control strategies in composite structures. The ability to strategically manipulate mass distribution provides an effective means of tuning vibrational characteristics and optimizing damping performance. The study offers valuable insights into the interplay between mass placement, boundary conditions, and modal behavior, contributing to the development of advanced vibration control methodologies for composite marine and offshore structures.

References

[1] Sathish, S., Murugesan, C. K., Ramkumar, R. (2015). Study of Mechanical Characteristics on Hybrid Composites Using Sisal Fiber and Banana Fiber. International Journal for Research in Applied Science & Engineering Technology, 3(6), 21-26.

[2] Dolbachian, L., Harizi, W., & Aboura, Z. (2024). Experimental Linear and Nonlinear Vibration Methods for the Structural Health Monitoring (SHM) of Polymer-Matrix Composites (PMCs): A Literature Review. Vibration, 7(1), 281-325. https://doi.org/10.3390/vibration7010015

[3] Mieloszyk, M., Majewska, K., & Ostachowicz, W. (2021). Application of Embedded Fibre Bragg Grating Sensors for Structural Health Monitoring of Complex Composite Structures for Marine Applications. Marine Structures, 76, 102903. https://doi.org/10.1016/j.marstruc.2020.102903

[4] Rubino, F., Nisticò, A., Tucci, F., & Carlone, P. (2020). Marine Application of Fiber Reinforced Composites: A Review. Journal of Marine Science and Engineering, 8(1), 26. https://doi.org/10.3390/jmse8010026

[5] Saadatmorad, M., Jafari-Talookolaei, R. A., Pashaei, M. H., & Khatir, S. (2022). Damage Detection in Rectangular Laminated Composite Plate Structures Using a Combination of Wavelet Transforms and Artificial Neural Networks. Journal of Vibration Engineering & Technologies, 10(5), 1647-1664. https://doi.org/10.1007/s42417-022-00471-6

[6] Barbero, E. J. (2018). *Introduction to Composite Materials Design* (3rd Editio). Boca Raton.

[7] Hollaway, L. C. (2010). A Review of the Present and Future Utilization of FRP Composites in the Civil Infrastructure with Reference to Their Important In-Service Properties. Construction and Building Materials, 24(12), 2419-2445. https://doi.org/10.1016/j.conbuildmat.2010.04.062

[8] Davies, P. (2024). Evaluation of New Composite Materials for Marine Applications. Applied Composite Materials, 31(6), 1933-1954. https://doi.org/10.1007/s10443-024-10232-1

[9] Huang, J., Tang, Y., Li, H., Pang, F., & Qin, Y. (2021). Vibration Characteristics Analysis of Composite Floating Rafts for Marine Structure Based on Modal Superposition Theory. Reviews on Advanced Materials Science, 60(1), 719-730. https://doi.org/10.1515/rams-2021-0043

[10] Zhu, C., Yang, J., Li, G., & Ruan, S. (2024). Vibration Suppression of Stiffened Laminated Composite Panels with Variable Angle Tow Fibers. Mechanics of Composite Materials, 60, 843-862. https://doi.org/10.1007/s11029-024-10230-1

[11] Zhou, K. (2024). Effects of the Concentrated Mass and Elastic Support on Dynamic and Flutter Behaviors of Panel Structures. International Journal of Mechanics and Materials in Design, 20(2), 373-392. https://doi.org/10.1007/s10999-023-09680-7

[12] Mojtahedi, A., Dadashzadeh, M., & Kouhi, M. (2024). Developing a Predictive Method Based on the Vibration Behavior of a Naval Ship Hull Model Using Hybrid Fuzzy Meta-Heuristic Algorithms. Ocean Engineering, 311, 118994. https://doi.org/10.1016/j.oceaneng.2024.118994

[13] Zhu, G., & Zhu, G. (2025). Chaos Phenomena in Nonlinear Vibration of Cantilever Beam with

Concentrated Mass Under the Effect of Fluid Flow. Proceedings of the Indian National Science Academy, 1-10. https://doi.org/10.1007/s43538-025-00392-4

[14] Zhang, Y. (2011). Eigenfrequency Computation of Beam/Plate Carrying Concentrated Mass/Spring. Journal of Vibration and Acoustics, 133(2), 021006. https://doi.org/10.1115/1.4002121

[15] Amabili, M. (2010). Geometrically Nonlinear Vibrations of Rectangular Plates Carrying a Concentrated Mass. Journal of Sound and Vibration, 329(21), 4501-4514. https://doi.org/10.1016/j.jsv.2010.04.024

[16] Garavaglia, E., & Tedeschi, C. (2022). Analysis of the mass and deformation variation rates over time and their influence on long-term durability for specimens of porous material. *Sustainable Structures*, *2*(1), 1-19. https://doi.org/10.54113/j.sust.2022.000014

[17] Aznaw, G. M. (2025). Advances in Composite Structures: A Systematic Review of Design, Performance, and Sustainability Trends. Composite Materials, 9(1), 1-17. https://doi.org/10.11648/j.cm.20250901.11

[18] Zhang, X., Zhou, L., Cai, X., Zheng, X., Liu, W., Wang, G., Tan, D., Luo, X., & Dong, M. (2024). Heterogeneous Structures and Morphological Transitions of Composite Materials and Its Applications. Advanced Composites and Hybrid Materials, 7(6), 251. https://doi.org/10.1007/s42114-024-01065-4

[19] Chaubey, A. K., Kumar, A., & Chakrabarti, A. (2018). Vibration of Laminated Composite Shells with Cutouts and Concentrated Mass. AIAA Journal, 56(4), 1662-1678. https://doi.org/10.2514/1.J056320

[20] Yang, C., & Oyadiji, S. O. (2016). Detection of Delamination in Composite Beams Using Frequency Deviations Due to Concentrated Mass Loading. Composite Structures, 146, 1-13. https://doi.org/10.1016/j.compstruct.2015.12.002

[21] Eken, S., Cihan, M., & Kaya, M. O. (2021). Vibration and Stability Analysis of a Spinning Thin-Walled Composite Beam Carrying a Rigid Body. Archive of Applied Mechanics, 91, 809-822. https://doi.org/10.1007/s00419-020-01790-4

[22] Hossain, N., Islam, M. S., Ahshan, K. H. N., & Hossain, M. Z. (2015). Effects on Natural Frequency of a Plate Due to Distributed and Positional Concentrated Mass. Journal of Vibroengineering, 17(7), 3751–3759.

[23] Zhong, Z., Liu, A., Pi, Y. L., Deng, J., Lu, H., & Li, S. (2019). Analytical and Experimental Studies on Dynamic Instability of Simply Supported Rectangular Plates with Arbitrary Concentrated Masses. Engineering Structures, 196, 109288. https://doi.org/10.1016/j.engstruct.2019.109288

[24] Mandal, A., Ray, C., & Haldar, S. (2020). *Free Vibration Analysis of Laminated Composite Plates and Shells Subjected to Concentrated Mass at the Center*. In Recent Advances in Theoretical, Applied, Computational and Experimental Mechanics: Proceedings of ICTACEM 2017. Springer Singapore, 49-57. https://doi.org/10.1007/978-981-15-1189-9_5

[25] Vatin, N., Abdikarimov, R., & Khodzhaev, D. (2021). *Vibrations of a Geometrically Nonlinear Viscoelastic Shallow Shell with Concentrated Masses*. International Scientific Conference "Construction Mechanics, Hydraulics and Water Resources Engineering", 264, 02046, EDP Sciences. https://doi.org/10.1051/e3sconf/202126402046

[26] Mojtahedi, A., Hokmabady, H., Kouhi, M., & Mohammadyzadeh, S. (2022). A Novel ANN-RDT Approach for Damage Detection of a Composite Panel Employing Contact and Non-Contact Measuring Data. Composite Structures, 279, 114794. https://doi.org/10.1016/j.compstruct.2021.114794

[27] Zahid, F. B., Ong, Z. C., & Khoo, S. Y. (2020). A Review of Operational Modal Analysis Techniques for In-Service Modal Identification. Journal of the Brazilian Society of Mechanical Sciences and Engineering, 42(8), 398. https://doi.org/10.1007/s40430-020-02470-8

[28] Janeliukstis, R., Mironovs, D., & Safonovs, A. (2022). Statistical Structural Integrity Control of Composite Structures Based on an Automatic Operational Modal Analysis—A Review. Mechanics of Composite Materials, 58, 181-208. https://doi.org/10.1007/s11029-022-10026-1

[29] DNV GL. (2015). Rules for Classification High Speed and Light Craft Part 3 Structures, Equipment Chapter 4 Hull Structural Design, Fibre Composite and Sandwich Constructions.

[30] Roig, R., Sánchez-Botello, X., & Escaler, X. (2023). Assessment of Novel Modal Testing Methods for Structures Rotating in Water. Applied Sciences, 13(5), 2895. https://doi.org/10.3390/app13052895

[31] Avitabile, P. (2001). Experimental Modal Analysis. Sound and Vibration, 35(1), 20-31.

[32] Pelayo, F., Skafte, A., Aenlle, M. L., & Brincker, R. (2015). Modal analysis based stress estimation for structural elements subjected to operational dynamic loadings. *Experimental Mechanics*, *55*, 1791-1802. https://doi.org/10.1007/s11340-015-0073-6

[33] Cao, X., Li, W., He, H., & Han, W. (2025). Modification of the Structure Dynamic Model for Spiral Bevel Gear Based on Modal Experiment.

Journal of Mechanical Science and Technology, 39, 531–539. https://doi.org/10.1007/s12206-025-0104-x

[34] Cai, C., Wang, B., Yin, W., Xu, Z., Wang, R., & He, X. (2022). A New Algorithm to Generate Non-Uniformly Dispersed Representative Volume Elements of Composite Materials with High Volume Fractions. Materials & Design, 219, 110750. https://doi.org/10.1016/j.matdes.2022.110750

[35] Banerjee, S., & Sankar, B. V. (2014). Mechanical Properties of Hybrid Composites Using Finite Element Method Based Micromechanics. Composites Part B: Engineering, 58, 318-327. https://doi.org/10.1016/j.compositesb.2013.10.065

[36] Prasad, K. V. S. R., & Singh, V. (2022). Numerical Investigation and Experimental Modal Analysis Validation to Mitigate Vibration of Induction Machine Caused Due to Electrical and Mechanical Faults. Journal of Electrical Engineering & Technology, 17(4), 2259-2273. https://doi.org/10.1007/s42835-022-01049-8

INTERNATIONAL JOURNAL OF
COASTAL, OFFSHORE & ENVIRONMENTAL ENGINEERING IJCOE Vol.10/No. 4/ Autumn 2025 (19-27)

Available online at: www. Ijcoe.org

Numerical Investigation on Dynamics of DeepCWind Floating Offshore Wind Turbine (FOWT) Platform

Mohammad Ahmadi[1], Mahdi Yousefifard[2], Hashem Nowruzi[3*]

[1] *MSc student, Mechanical Engineering Department, Babol Noshirvani University of Technology; mohammad.ahmadih2r@gmail.com*
[2] *Assistant professor,Mechanical Engineering Department, Babol Noshirvani University of Technology; h.nowruzi@nit.ac.ir*
[3*] *Assistant professor, Mechanical Engineering Department, Babol Noshirvani University of Technology; yousefifard@nit.ac.ir*

ARTICLE INFO

Article History:
Received : 17 Apr 2025
Accepted : 06 Jan 2026

Keywords:
FOWT
CFD
Heave and pitch motions
FPSO
OpenFOAM

ABSTRACT

Renewable energies are a crucial component of sustainable development. Offshore wind energy is an interesting clean energy alternative to fossil fuels. In floating offshore wind turbines (FOWTs), a lower floating platform couples/integrates with the upper wind turbine, and the motion of each component influences the other. Therefore, understanding the dynamic behaviors of FOWT platforms is necessary for designing them in real sea states. The present paper numerically investigates the heave and pitch dynamic motions of the DeepCWind FOWT platform at three different offsets between the columns, all under regular waves. To this accomplishment, a 3D RANS-VOF model is implemented in the open-source CFD platform of OpenFOAM. The current numerical simulations of heave and pitch motions of the sandglass-type platform with appropriate accordance are validated against the existing experimental data. The main results show that increasing the offsets between the FOWT platform columns (wide model) significantly reduces the heave and pitch motions. However, the effects of decreasing the distance between the columns (i.e., a tight model) on heave and pitch motions are insignificant compared to the original model.

1. Introduction

Emphasizing renewable energy is a crucial aspect of sustainable development. Consequently, there exists an unequivocal necessity to innovate technologies for the production of renewable energy [1]. The advancement of solar and onshore wind energy has demonstrated considerable efficacy in electricity generation, positioning these sources in competition with conventional production methods such as coal, gas, fuel, and nuclear energy [2]. Recently, despite comprising merely 0.3% of global electricity generation, the growth of offshore wind energy has emerged as a significant enhancement to the energy mix. Offshore wind energy enables the deployment of larger turbines compared to onshore turbines and benefits from a more consistent and robust wind resource, achieving a capacity factor of 40-50% [3]. The International Energy Agency (IEA) reports that offshore wind energy has the potential to satisfy global energy demand 11 times by 2040. To attain this capacity, it is essential to expand installations to deeper water depths. Fixed offshore platforms possess depth constraints.

Consequently, the resolution for utilizing the extensive wind resources of the oceans at greater depths is to transition from fixed platforms to floating structures. The initiation and progression of extensive commercial floating wind projects necessitates enhanced knowledge of turbine power generation. A significant technological challenge in floating offshore wind turbines (FOWTs) is the dynamic behavior of the platform, which induces additional rotor movement and may influence the average power output over time, thereby impacting electricity generation [4]. Consequently, the design of a floating support platform with enhanced dynamic motion may optimize the aerodynamic efficiency of the FOWT. Currently, prevalent support structures have been established, categorized into four primary types: spar-buoy, tension-leg platform (TLP), semi-submersible, and barge. Each category of these structures employs one

of three methods—weights, mooring lines, buoyancy, or a combination thereof—to attain static stability. For a more thorough assessment, one may consult [5]. The semi-submersible platform represents a highly advanced concept in this sector, predominantly utilized in the oil and gas industry, and it appears to possess a marginal advantage in the market for floating offshore wind turbines. This technology predominantly obtains its stability from buoyancy. These platforms possess a considerable advantage due to their catenary anchor lines being more economical than TLP, along with a comparatively simpler installation process. The turbine can be positioned adjacent to the dock, and the floating structure may be towed to its site or returned to shore for maintenance or decommissioning. The primary constraint is its intricate geometry, which complicates construction. This necessitates a considerable quantity of structural mass [6]. The most sophisticated initiative in this category is the WindFloat concept, developed by Principle Power (PP) [7]. In 2011, Principle Power (PP) successfully installed a prototype in Portugal, operated it for four years, decommissioned it, and then reinstalled it in Scotland in 2018. Globally, companies are developing numerous commercial-scale wind farm projects using Windfloat technology. Other companies have introduced semi-submersible concepts at a stage that precedes development. Figure 1 depicts several of them. The research community extensively utilizes the open-source semi-submersible design, DeepCWind, to enhance comprehension of the physics of FOWT and to communicate findings.

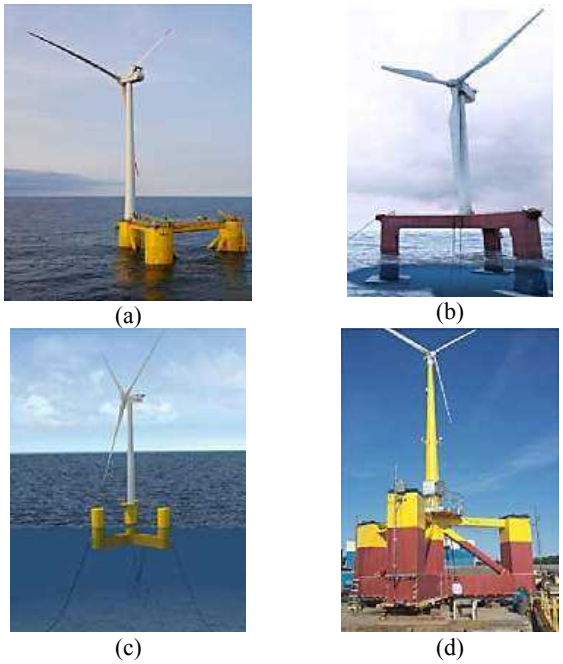

Figure 1. Semi-submersible concepts for floating offshore wind turbines: (a) WindFloat (Principle Power) (b) Tri-Floater (GustoMSC) (c) Naval Energies Technology (d)Maine University Technology [8]

The hydrodynamic, aerodynamic, or aero-hydro-servo analysis of FOWTs has been the subject of numerous experimental and numerical studies. Benitez and his colleagues [9] studied the hydrodynamics of FOWTs by running numerical simulations on the semi-submersible platform DeepCwind in 2015 to find out how different geometric parameters affected the hydrodynamic coefficients. They specifically looked at drag behavior, free surface effects, and the multi-member configuration of the semi-submersible structure. Zhao and Wan [10] studied the hydrodynamic characteristics of the support platform displacements during wind turbine shutdown conditions utilizing OpenFOAM. The pitch and sway motion of the floating platform is affected by the aerodynamic loads from the turbine. In 2015, Dunbar [11] proposed a six DoF solver coupled with OpenFOAM for the excitation of semi-submersible floating offshore wind turbine platforms. The validation of the CFD simulation results for the DeepCwind semi-submersible platform was performed using experimental data across various sections, encompassing heave and pitch motions. In 2016, Yan and colleagues [12] proposed a computational framework using the finite element method with isogeometric analysis (IGA) to investigate fluid-structure interaction and assess the hydrodynamic forces on floating wind turbine platforms, with computational results validated against experimental data. In 2018, Wang and colleagues [13] conducted an extensive review of the diverse variables associated with offshore wind platforms in relation to specific sample projects, focusing particularly on a novel foundation for wind turbines. The researchers examined the system under diverse combined and extreme loads through numerical simulations and field tests, resulting in an enhanced geometric design that accounts for transportability. In 2020, Zhang and associates [14] performed a comparative analysis of the hydrodynamic performance of three platforms at varying water depths, taking into account second-order hydrodynamic forces. The pitch motion of the DeepCwind4 semi-submersible wind turbine is more responsive to second-order wave loads than the other two wind turbines. In 2021, Johalas and colleagues [15] investigated the performance of a 5 MW reference wind turbine installed on the semi-submersible platforms UMaine3OC and DeepCwind4OC under wind-wave conditions. The researchers analyzed the impact of the interaction between the movement of the support platform and the wind turbine rotor on the average power output, ultimately deriving a straightforward analytical formula for predicting average power in floating turbines at low wind speeds. In 2022, Wang and colleagues [16] conducted a study to validate the DeepCwind semi-submersible model through computational fluid dynamics, which underwent free decay motion analysis. The researchers analyzed the hydrodynamic damping behavior and characteristics of the platform in calm water and validated their results with experimental data. In 2022,

Serjinko and colleagues [17] published a review article analyzing various proposed techniques for advanced floating support structures designed for larger wind energy systems, emphasizing system dynamics. The findings indicated that the mass of the wind turbine, the rated power, and the rotor thrust scale correlate with the square of the rotor diameter. In 2022, Elkafas and colleagues [18] performed a numerical study on the hydrodynamic response of three distinct configurations of the DeepCwind model by altering the number of offset columns from three to five. Statistical findings concerning regular and irregular waves indicate that the wave response is inversely related to the quantity of offset columns. The effect of increasing offset columns on vertical displacements and elevation is minimal. In 2023, Eskilsson and associates [19] performed a numerical study simulating the hydrodynamics of the semi-submersible platform. The implementation of a one-way coupling in the mooring-fluid system yields marginally increased mooring forces, yet it does not substantially influence the motion response of the floating wind turbine. In 2024, Zhou and colleagues [20] investigated the hydrodynamic performance of a co-located farm comprising an array of OC4-DeepCwind FOWT and floating photovoltaic systems (FPVs). Case studies have been conducted to analyze the impact of platform geometric parameters on the hydrodynamic performance of wind and solar platforms. The results offer insights for the optimal design of floating photovoltaic systems and illustrate the potential synergy between wind and solar energy on floating platforms. In 2024, Zeng and colleagues [21] explored the theoretical challenges and progressed research developments associated with nonlinear hydrodynamic issues pertaining to floating offshore wind turbines (FOWT). They examined various nonlinear phenomena associated with their mooring systems, including low-frequency resonance, transient impacts, hydro-elastic coupling, flow effects, and shallow water effects, from both numerical and physical viewpoints. Numerous researchers have performed experimental investigations on FOWT [22, 23], including Chen and colleagues floating turbine model tests on various platforms [24], which assessed the distinctive relative performance of each of the three systems, focusing on structural motions, tower dynamics, and the system's heave response. In 2020, Belloli et al. [25] conducted a wind tunnel analysis of FOWT.

According to the literature review and the authors' expertise, the primary challenge for engineering teams designing these structures is the precise forecasting of the offshore platform's performance under all expected environmental conditions during its operational lifespan. Dynamic stability is the primary criterion for averting the capsizing or submersion of the offshore platform. Consequently, the imperative for additional research to ascertain an optimal solution that guarantees stability and efficiency at minimal expense is crucial. However, in order to analyze all the previously mentioned scenarios within a reasonable timeframe, researchers have consistently prioritized the creation of an engineering tool and a suitable study method based on simplified assumptions. This study examines the dynamic performance of the DeepCWind semi-submersible platform in freely floating conditions. This study aims to illustrate that the proposed method is effective, allowing for the utilization of numerical tools in place of laborious and complex FOWT simulations. The open-source CFD software OpenFOAM has been utilized for simulation to attain this objective, and the findings have been presented in a comparative format.

2. Governing Equations

The current study utilized the open-source software OpenFOAM for computational fluid dynamics simulation. The software, proficient in resolving Reynolds-Averaged Navier-Stokes (RANS) equations, executes dynamic motion simulations within the InterDyMFoam solver. The governing equations are delineated as follows.

In the field of rigid body motion, the transitional movement of the floating body with mass m exposed to the external force fi is as follows:

$$m\frac{dv}{dt} = f \tag{1}$$

where, v shows the velocity of the center of floating mass. Also, the equation of angular motions of a floating body around the center of mass has the following form:

$$M\frac{d\omega}{dt} + \omega \times M\omega = n \tag{2}$$

where, M is the tensor of moment of inertia, ω is the rigid body angular velocity, and n is the excitation force applied to the floating body. In order to dynamic analysis of sandglass, preliminary, according to fluid flow solution and pressure distribution on the submerged surface of the sandglass, excitation forces in Eq. (1 and 2) are derived. Then, body transitional and angular movements are derived by using Eq. (1 and 2). To this accomplishment, fluid flow is simulated by RANS equations. The free surface is also modeled by two-phase approach of fluid volume fraction and artificial density [26]. The conservation of mass and momentum equations in the two-phase fluid motion are as follows:

$$\nabla . U = 0 \tag{3}$$

$$\frac{\partial \rho U}{\partial t} + \nabla \cdot \left(\rho\left(U - U_g\right)U\right) = \tag{4}$$

$$-\nabla p_d - g \cdot \mathrm{x}\nabla\rho + \nabla \cdot \left(\mu_{eff}\nabla U\right) + \left(\nabla U\right) \cdot \nabla \mu_{eff} + f_\sigma$$

here, U and $\underline{U_g}$ are fluid velocity and grid cell movement velocity, respectively. Moreover, P_d is the

dynamic pressure may be computed as $p_d = p - \rho g \cdot x$ (i.e. the difference between total and hydrostatic pressure). The acceleration of gravity is considered *as* $g = (0,0,-9.81)$. Effective dynamic viscosity is also equal with $\mu_{eff} = \rho(v + v_t)$ (i.e., where v_t and v are eddy and kinematic viscosities, respectively), and f_σ is the surface tension as a source term. The approach of fluid volume fraction is a method to estimate the free surface by using:

$$\frac{\partial \alpha}{dt} + \nabla \cdot \left[(U - U_g)\alpha \right] + \nabla \cdot \left[U_r (1-\alpha)\alpha \right] = 0 \quad (5)$$

here, the volume ratio (α) in the Eq.(5) is the properties of the fluid inside each cell as follows:

$$\begin{cases} \alpha = 0 & air \\ \alpha = 0 & water \\ 0 < \alpha < 1 & \text{int } erface \end{cases} \quad (6)$$

The variable U_r in Eq.(5) is the fluid domain velocity which applies the effects of velocity at the boundary of water and air [27]. It is notable that, the surface tension f_σ in Eq (4) is equal $f_\sigma = \sigma k \nabla \alpha$ (i.e., where k is the curvature of the free surface and σ = 0.07 kg/sq.s is the surface tension of water, which can be derived using the definition of volume ratio (α). Therefore, the density and dynamic viscosity of free surface is as follows:

$$\begin{cases} \rho = \alpha \rho_1 + (1-\alpha)\rho_g \\ \mu = \alpha \mu_1 + (1-\alpha)\mu_g \end{cases} \quad (7)$$

It is notable that the shear stress transport (SST) equation is also considered for the simulation of turbulent flow [28].

3. Physics of the Problem and Validation

As the main goal of this study is to analyze the dynamic behavior of offshore floating platforms, it is essential to assess the accuracy of the numerical solution method in comparison to experimental laboratory data. Consequently, prior to examining the calculations, a validation of the dynamic movements of a sand-glass type floating body (STFB) within floating production, storage, and offloading (FPSO) structures has been conducted. Figure 3 presents an illustration of the two-dimensional perspective and geometric characteristics of the STFB. This study presents the dynamic behavior of the STFB floating platform model at a 1:70 scale to evaluate the accuracy of the results obtained through the finite volume method, in comparison with other experimental [29] and numerical data. [30]. Table 1 presents the main physical parameters of the STFB.

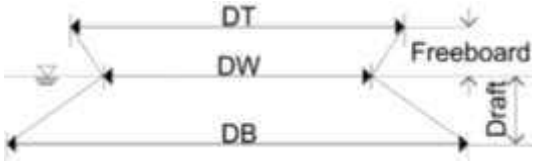

Figure 2. 2D section of STFB

Table 1. Main physical characteristics of considered STFBs

Parameter	Exp.	Model	Unit
Scale (λ)	1	70	-
Diameter of upper deck (D_T)	78.864	1.126	m
Diameter of waterline plane (D_W)	52.4	0.748	m
Radius of lower bottom (D_B)	90.012	1.286	m
Draft (d)	13.168	0.188	m
Freeboard (f)	20	0.286	m
Displacement (Δ)	55000	0.16	ton
Pitch inertia radius	17.550	0.251	m

A numerical wave tank (NWT) has been utilized in OpenFOAM with the InterDyMFoam solver to examine the dynamics of STFB in regular waves. The numerical simulations applied the Reynolds-Averaged Navier-Stokes (RANS) equations using the computational fluid dynamics (CFD) technique and resolved them using the FVM. The initial dimensions of the computational domain are L = 34 meters, B = 10 meters, and H = 14 meters, under deep water assumptions. The dimensions of the computational domain, as per ITTC guidelines for numerical methods and other dynamic analyses [31], are illustrated in Figure 4 for floating platforms. Figure 3 also illustrates the morphology of the mesh structure around the hull. A structural mesh has been employed in all solution domains, except in the regions surrounding the body, where multiple layers of graded structural and non-structural cells have been utilized.

The simulated periodic waves are classified as second-order Stokes waves. Harmonic waves are produced at the inlet boundary x = 10 by virtual alterations in horizontal velocity (i.e., the position of the wave generator), and the resultant regular wave propagates in the negative X direction. On the opposing side, where x = -24 meters, outlet conditions are applied. The center of mass of the STFB is positioned at x = 2.83 meters, utilizing the symmetry condition for the x = 0 plane.

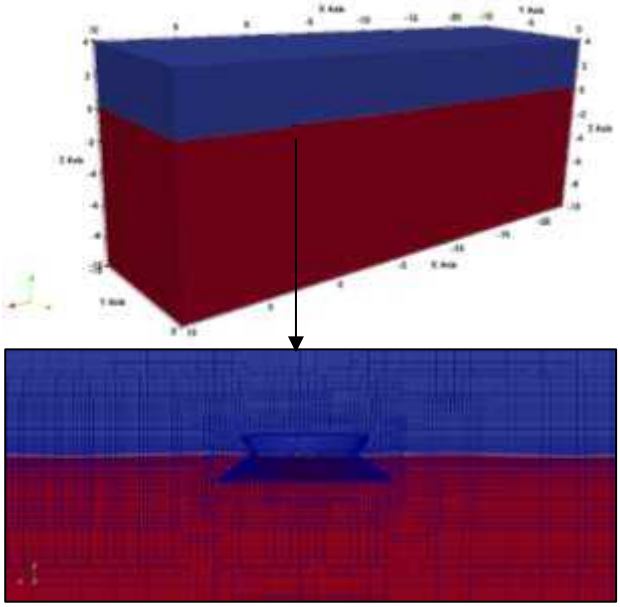

Figure 3. Considered numerical domain and the mesh structure around the STFB.

To validate the uncertainty in the numerical solution, three distinct mesh configurations, A, B, and C, have been evaluated for result accuracy. The numerical findings of this study regarding the heave of the STFB at a frequency of 0.29 have been analyzed using three distinct meshes. Table 2 presents the average values of the heave motion response for each cases. The mesh sensitivity analysis indicated that the total number of cells generated in the solution domain was approximately 1,181,169. This number has also been partially derived from wave characteristics. Due to the geometric characteristics of the model, the symmetry condition was applied to half of the computational domain. Then, the results are generalized for the entire computational domain.

Figures 4 and 5 illustrate the responses for heave RAO and pitch RAO of the STFB, simulated in this study with the FVM, in conjunction with experimental data [29], Boundary Element Method (BEM) results [32], and Boundary Value Problem (BVP) outcomes derived from WAMIT [29]. The current study's simulation demonstrates superior accuracy in both the magnitude and trend of the heave and pitch RAOs compared to the boundary element method and boundary value problem results.

Table 2. Details of mesh sensitivity analysis

Case	Δx [m]	Δy [m]	Δz [m]	Total cells	Run time	Mean value of Heave RAO [-]
A	0.012	0.012	0.012	524633	10 h	1.411
B	0.010	0.010	0.010	1012850	16 h	1.462
C	0.008	0.008	0.008	1485162	22 h	1.470

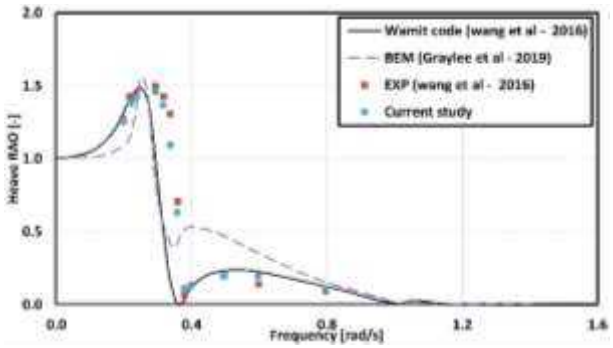

Figure 4. Heave RAO results of STFB

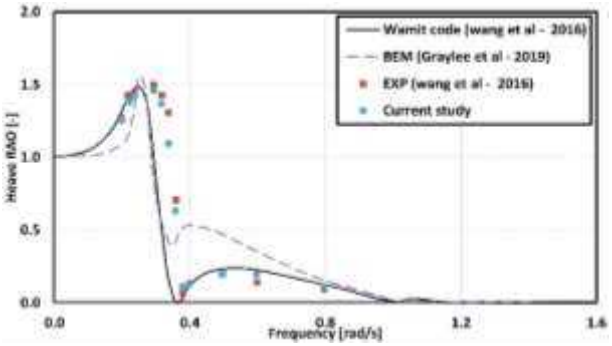

Figure 5. Pitch RAO results of STFB

Tables 3 and 4 present the quantitative discrepancies between the numerical results and the experimental data for the heave and pitch RAOs for each of the wave frequencies in this study. The assessment of the average error rate indicates that the finite volume method is an effective and dependable instrument for analyzing the dynamics of a floating platform in regular waves. The finite volume method has demonstrated a commendable capacity to accurately estimate the trends and recorded values of the floating platform's movements, particularly at critical points.

Table 3. Details of heave RAO compared to the experiment

Frequency [rad/s]	Heave RAO		
	Experimental data [29]	Current study	Error [%]
0.2	1.29	1.26	2.33
0.22	1.44	1.39	2.99
0.24	1.44	1.42	1.93
0.29	1.51	1.46	3.27
0.32	1.44	1.40	2.84
0.34	1.32	1.25	4.88
0.36	0.71	0.68	3.91
0.38	0.08	0.09	16.54
0.40	0.14	0.12	14.86
0.50	0.21	0.20	4.11
0.60	0.14	0.19	31.15
0.80	0.11	0.11	3.96

Table 4. Details of pitch RAO compared to the experiment

Frequency [rad/s]	Pitch RAO		
	Experimental data [29]	Current study	Error [%]
0.24	0.27	0.22	18.07
0.26	0.37	0.28	23.94
0.38	0.52	0.59	13.48
0.40	0.67	0.65	3.59
0.50	0.87	0.84	3.47
0.60	0.91	0.95	3.96
0.69	0.91	0.98	7.92
0.8	0.78	0.81	3.86

Linearized methods are predicted to exhibit considerable discrepancies when compared to experimental results. Consequently, when the objective of the research is to enhance the dynamic behavior of a complex or optimized geometric shape, linearized methods prove to be unreliable. Small deviations in the results are significant concerning the limitations of these methods.

4. Results and Discussion

This section models the DeepCWind concept for the dynamic analysis of the support platform bases subjected to regular waves. The OC4 and OC5 projects conducted testing campaigns for this design at a marine model scale of 1/50. Figure 6 illustrates that the DeepCWind semi-submersible platform comprises three offset columns (consisting of base and upper columns), a central column, and multiple sets of pontoons and cross braces.

Reference [22] details the platform movements and mooring system under wave-only or combined wave and wind conditions. This section presents simulations of the offset semi-submersible DeepCWind bases under free-floating conditions (without mooring) across various scenarios, based on the validation of the solution method and the accuracy of dynamic results in evaluating a floating platform. The primary physical characteristics of the reference platform are detailed in Table 5.

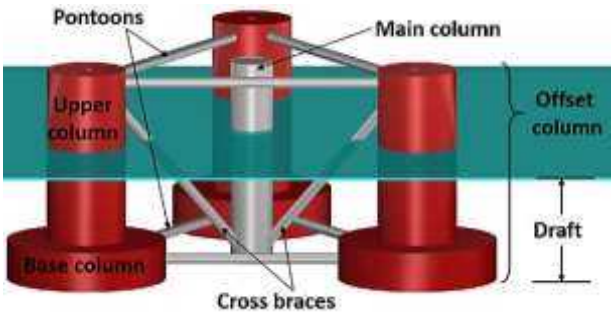

Figure 6. DeepCWind semi-submersible platform

Table 5. Characteristics of the main and the scaled models

Geometrical Characteristics	Exp.	Model
scale [-]	1	50
overall draft [m]	20	0.4
Main column (tower bottom) height above SWL [m]	10	0.2
Offset column height above SWL [m]	12	0.24
Distance among the offset columns [m]	50	1
Top columns length	26	0.52
Base columns length [m]	6	0.12
Distance up top of base columns under SWL [m]	14	0.28
Main columns diameter [m]	6.5	0.13
upper columns diameter [m]	1.2	0.024
Base columns diameter [m]	24	0.48
Cross braces and pontoon diameter [m]	1.6	0.032
Structural Characteristics		
Displacement [m^3]	13986.8	0.112
Center of mass (CM) location below SWL [m]	14.4	0.288
Platform pitch inertia about CM [kg-m^2]	8.01×10^9	25.64
Platform pitch inertia about CM [kg-m^2]	8.01×10^9	25.64
Platform Yaw inertia about platform centerline [kg-m^2]	13.9×10^9	44.51

This study excludes pontoons and cross braces. The simplified geometric configuration of the DeepCWind semi-submersible support platform has been employed to assess its dynamic behavior. The assessment of the two heave modes, reduced (wide) and increased (tight), of the offset bases relative to the original condition in free-floating wave scenarios has been performed. The reference support platform is depicted in three distinct configurations according to Figure 7. A refined state has been implemented to decrease the distance between the offset bases by 20%, while an expanded state has been adopted to increase the distance between the offset bases by 20% relative to the original state. The adjusted distance between the offset bases concerning the platform's center of buoyancy has been implemented. Furthermore, in conjunction with the three delineated models (refer to Figure 7), the dynamic outcomes of one of the platform's foundations (mono-offset column) are also exhibited. The semi-submersible platform models depicted in Figure 7 are incorporated in a comparative analysis to investigate the flow between the offset bases and its effect on the dynamic behavior of the supporting platform.

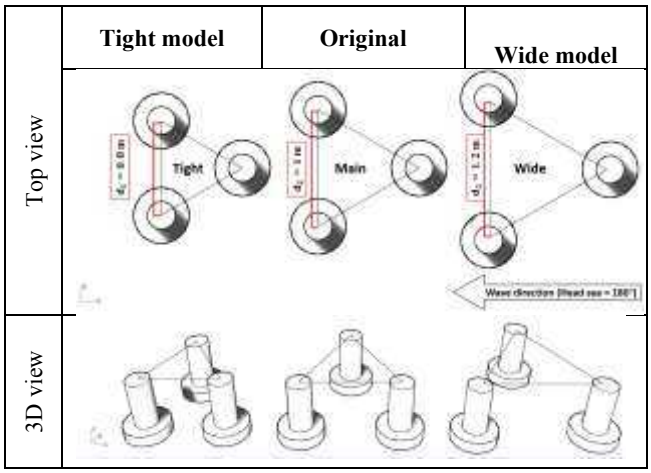

Figure 7. Diagram illustrating the specifications of three semi-submersible platform models: tight, original, and wide model determined by the distances between the offset bases

Figures 8 and 9 present the current study's free-floating condition results against the laboratory results constrained by the DeepCWind semi-submersible platform's mooring system. A comparative analysis of the heave and pitch motions of the platform across varying wave periods has been conducted, with the

horizontal and vertical axes denoting the wave impact periods (spanning from a wavelength of 0.5 to 21 meters) and the response amplitude operator (RAO), respectively. Figures 8 and 9 illustrate the impact of mooring on the amplitude response of the supporting platform's movements. The analysis of the motion curve's slope and the fluctuations in the platform's oscillations in a free-floating state, in comparison to the experimental data of Coulling et al. [22], suggests that the anchoring system is engineered to regulate pitch stability and diminish the amplitude of the platform's vertical oscillations. The maximum amplitude of the platform's longitudinal pitch in a free-floating state was observed at a wave period of 18 seconds; however, upon the application of anchoring effects, the floating platform demonstrated a more consistent pitching motion. In the vertical displacement motion of the support platform, the anchoring effects have resulted in a gradual decrease in the rate of increase of the platform's vertical oscillations, transitioning from shorter wavelength waves to longer wavelength waves (i.e., period interval 14 to 18 seconds).

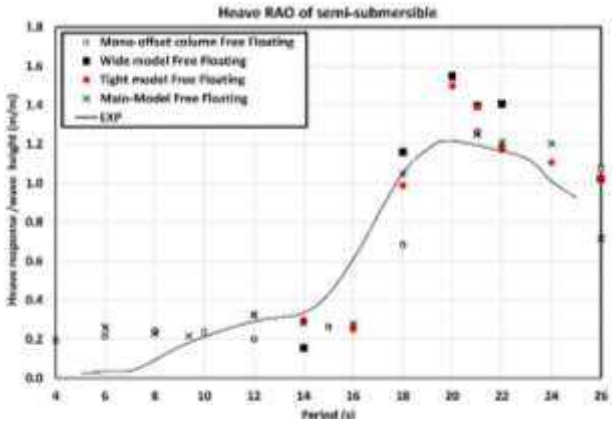

Figure 8. Comparison of heave RAO results of FOWT's platform in free-floating condition

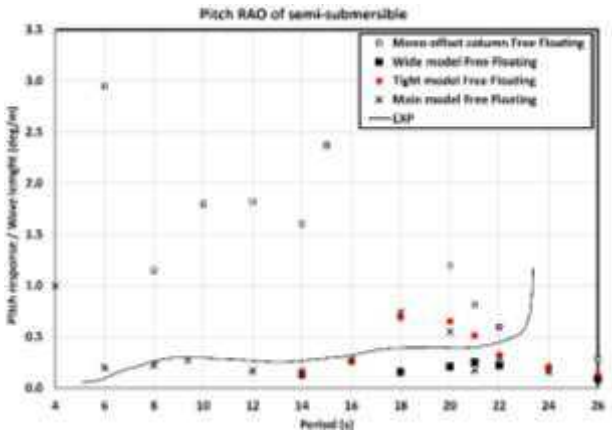

Figure 9. Comparison of pitch RAO results of FOWT's platform in free-floating condition

According to the observations in Figure 8, the primary model under free-floating conditions resembles that under anchored conditions for wave periods exceeding the critical range for certain resonances to manifest. The amplification of the platform's elevation movements at a period of 20 seconds may be attributed to the platform's increased submersion in water.

The dynamic outcomes of the wide and tight model have been analyzed solely within the critical range. Despite the negligible differences in results relative to the original state, discerning the dynamic behavior under various conditions yields valuable insights for the conceptual design of floating wind turbines. The picture in Figure 9 shows that the large semi-submersible platform model has decreased the pitch amplitude at most points within the critical range compared to the original model. However, it has increased the oscillations in heave motion for most wave periods compared to the original model. On the other hand, as shown in Figure 8, the small semi-submersible platform has effectively reduced the largest vertical displacement oscillations within the critical range of larger waves. It is noteworthy that in the pitch movement of the reduced-scale platform model, before the maximum dynamic response (wave period of 18 seconds), it displayed identical behavior to the original model. However, after reaching the apex, the scaled-down platform's curve continued to decline, exhibiting increased fluctuations compared to the original model.

5. Conclusions

Exploring renewable energy sources is crucial for achieving sustainable development. Wind energy serves as an appealing clean alternative to fossil fuels. The offshore wind power sector is experiencing significant growth. Offshore wind turbines offer several benefits in comparison to onshore wind platforms, including higher wind speeds, more consistent airflow with reduced turbulence, and fewer aesthetic concerns. Unlike traditional onshore or fixed offshore wind turbines, a floating offshore wind turbine (FOWT) requires a supporting platform. In a FOWT system, the upper wind turbine is connected to a lower floating platform, and the movements of each component influence one another. The current study highlights the importance of understanding the dynamic behaviors of floating offshore wind turbine (FOWT) platforms, specifically the DeepCWind model, under varying column offsets. The open-source CFD code of OpenFOAM models the three columns of FOWT's platform with various column offsets and free-floating mono-offset columns to achieve this accomplishment. Numerical simulations are conducted using a 3D RANS-VOF model and under regular wavy conditions. Preliminary mesh sensitivity analysis is conducted, and the numerical results of the sandglass-type FOWT platform are validated with experimental data. The main results indicate that increasing the distance between the platform columns significantly reduces heave and pitch motions, thereby enhancing the platform's stability and efficiency in real sea conditions.

6. References

[1] Koutoudjian, G., Diniz, L., Cespedes, R., & UNDP, V. G. (2021). About IRENA The International Renewable Energy Agency (IRENA) is an intergovernmental organisation that supports countries in their transition to a sustainable energy future, and serves as the principal platform for international co-operation, a centre of excellence, and a repository of policy, technology, resource and financial knowledge on renewable energy. IRENA promotes the. *IRENA promotes the*, 24.

[2] Eia, U. S. (2016). Levelized cost and levelized avoided cost of new generation resources in the annual energy outlook 2016. *Washington DC, USA*.

[3] Cozzi, L., Gould, T., Bouckart, S., Crow, D., Kim, T. Y., McGlade, C., ... & Wetzel, D. (2020). World energy outlook 2020. Energy, 2019, 30.

[4] Liu, Y., Xiao, Q., Incecik, A., & Wan, D. C. (2016). Investigation of the effects of platform motion on the aerodynamics of a floating offshore wind turbine. *Journal of Hydrodynamics*, *28*(1), 95-101.

[5] Castro-Santos, L., & Diaz-Casas, V. (Eds.). (2016). *Floating offshore wind farms* (p. 204). Switzerland: Springer International Publishing.

[6] James, R., & Ros, M. C. (2015). Floating offshore wind: market and technology review. *The Carbon Trust*, *439*.

[7] Cermelli, C., Aubault, A., Roddier, D., & McCoy, T. (2010, May). Qualification of a semi-submersible floating foundation for multi-megawatt wind turbines. In *Offshore Technology Conference* (pp. OTC-20674). OTC.

[8] Pinguet, R. (2021). *Hydrodynamics of semi-submersible floater for offshore wind turbines in highly nonlinear waves using Computational Fluid Dynamics (CFD), and validation of overset meshing technique in a numerical wave tank* (Doctoral dissertation, Ecole Centrale Marseille).

[9] Benitz, M. A., Schmidt, D. P., Lackner, M. A., Stewart, G. M., Jonkman, J., & Robertson, A. (2015, May). Validation of hydrodynamic load models using CFD for the OC4-DeepCwind semisubmersible. In *International Conference on Offshore Mechanics and Arctic Engineering* (Vol. 56574, p. V009T09A037). American Society of Mechanical Engineers.

[10] Zhao, W., & Wan, D. (2015). Numerical study of interactions between phase II of OC4 wind turbine and its semi-submersible floating support system. *J. Ocean Wind Energy*, *2*(1), 45-53.

[11] Dunbar, A. J., Craven, B. A., & Paterson, E. G. (2015). Development and validation of a tightly coupled CFD/6-DOF solver for simulating floating offshore wind turbine platforms. *Ocean Engineering*, *110*, 98-105.

[12] Yan, J., Korobenko, A., Deng, X., & Bazilevs, Y. (2016). Computational free-surface fluid–structure interaction with application to floating offshore wind turbines. *Computers & Fluids*, *141*, 155-174.

[13] Wang, X., Zeng, X., Li, J., Yang, X., & Wang, H. (2018). A review on recent advancements of substructures for offshore wind turbines. *Energy conversion and management*, *158*, 103-119.

[14] Zhang, L., Shi, W., Karimirad, M., Michailides, C., & Jiang, Z. (2020). Second-order hydrodynamic effects on the response of three semisubmersible floating offshore wind turbines. *Ocean Engineering*, *207*, 107371.

[15] Johlas, H. M., Martínez-Tossas, L. A., Churchfield, M. J., Lackner, M. A., & Schmidt, D. P. (2021). Floating platform effects on power generation in spar and semisubmersible wind turbines. *Wind Energy*, *24*(8), 901-916.

[16] Wang, L., Robertson, A., Jonkman, J., Kim, J., Shen, Z. R., Koop, A., ... & Yu, K. (2022). OC6 phase Ia: CFD simulations of the free-decay motion of the DeepCwind semisubmersible. *Energies*, *15*(1), 389.

[17] Sergiienko, N. Y., Da Silva, L. S. P., Bachynski-Polić, E. E., Cazzolato, B. S., Arjomandi, M., & Ding, B. (2022). Review of scaling laws applied to floating offshore wind turbines. *Renewable and Sustainable Energy Reviews*, *162*, 112477.

[18] Elkafas, A. G., Ahmed, Y. M., & Elgohary, M. M. (2022). Hydrodynamic analysis of floating offshore wind turbine With different numbers of offset columns. *Marine Technology Society Journal*, *56*(2), 8-19.

[19] Eskilsson, C., Fernandez, G. V., Andersen, J., & Palm, J. (2023, June). Hydrodynamic simulations of a FOWT platform (1st FOWT comparative study) using openfoam coupled to moodycore. In *ISOPE International Ocean and Polar Engineering Conference* (pp. ISOPE-I). ISOPE.

[20] Zhu, K., Shi, H., Tao, J., Gong, H., Han, Z., & Cao, F. (2024). Analytical study on hydrodynamic performance of co-located offshore wind–solar farms. *Physics of Fluids*, *36*(1).

[21] Zeng, X., Shao, Y., Feng, X., Xu, K., Jin, R., & Li, H. (2024). Nonlinear hydrodynamics of floating offshore wind turbines: A review. *Renewable and Sustainable Energy Reviews*, *191*, 114092.

[22] Coulling, A. J., Goupee, A. J., Robertson, A. N., Jonkman, J. M., & Dagher, H. J. (2013). Validation of a FAST semi-submersible floating wind turbine numerical model with DeepCwind test data. *Journal of Renewable and Sustainable Energy*, *5*(2).

[23] Chen, C., Ma, Y., & Fan, T. (2022). Review of model experimental methods focusing on

aerodynamic simulation of floating offshore wind turbines. *Renewable and Sustainable Energy Reviews*, *157*, 112036.

[24] Koo, B. J., Goupee, A. J., Kimball, R. W., & Lambrakos, K. F. (2014). Model tests for a floating wind turbine on three different floaters. *Journal of Offshore Mechanics and Arctic Engineering*, *136*(2), 020907.

[25] Belloli, M., Bayati, I., Facchinetti, A., Fontanella, A., Giberti, H., La Mura, F., ... & Zasso, A. (2020). A hybrid methodology for wind tunnel testing of floating offshore wind turbines. *Ocean Engineering*, *210*, 107592.

[26] Rusche, H. (2002). Computational fluid dynamics of dispersed two-phase flow at high phase fractions. Ph. D. thesis, University of London.

[27] Berberović, E., van Hinsberg, N. P., Jakirlić, S., Roisman, I. V., & Tropea, C. (2009). Drop impact onto a liquid layer of finite thickness: Dynamics of the cavity evolution. Physical Review E—Statistical, Nonlinear, and Soft Matter Physics, 79(3), 036306.

[28] Menter, F. R. (2009). Review of the shear-stress transport turbulence model experience from an industrial perspective. International journal of computational fluid dynamics, 23(4), 305-316.

[29] Wang, W. H., Wang, L. L., Du, Y. Z., Yao, Y. X., & Huang, Y. (2016). Numerical and experimental analysis on motion performance of new sandglass-type floating body in waves. *Marine structures*, *46*, 56-77.

[30] Graylee, A., & Yousefifard, M. (2020). The effects of different cross sections on the hydrodynamic behaviour of sandglass-type FPSOs exposed to regular waves. *Journal of Marine Engineering & Technology*, *19*(4), 197-206.

[31] Yousefifard, M., & Nowruzi, H. (2024). Hydrodynamic performance of sandglass-type floating body with damping appendages. *Ocean Engineering*, *309*, 118579.

[32] Graylee, A., & Yousefifard, M. (2020). The effects of different cross sections on the hydrodynamic behaviour of sandglass-type FPSOs exposed to regular waves. *Journal of Marine Engineering & Technology*, *19*(4), 197-206.

INTERNATIONAL JOURNAL OF
COASTAL, OFFSHORE & ENVIRONMENTAL ENGINEERING IJCOE Vol.10/No. 4/ Autumn 2025 (28-34)

Available online at: www. Ijcoe.org

Characteristics of a Circular Cylinder Response under Vortex-Induced Vibration in a Subcritical Flow Regime

Mohammadreza Vaselali[1], Maryam Soyuf Jahromi[2*], Abolfazl Pourrajabian[3]

[1]Ph.D Student in Physical Oceanography, Department of Nonliving Resources of Atmosphere and Ocean, Faculty of Marine Science and Technology, University of Hormozgan, Bandar Abbas, Iran, vaselali.mr@gmail.com
[2] Associate Professor of Physical Oceanography, Department of Nonliving Resources of Atmosphere and Ocean, Faculty of Marine Science and Technology, University of Hormozgan, Bandar Abbas, Iran, soyufjahromi@hormozgan.ac.ir*
[3] Associate Professor, Department of Energy, Materials and Energy Research Center (MERC), Karaj, Iran, a.pourrajabian@merc.ac.ir

ARTICLE INFO

Article History:
Received : 18 May 2025
Accepted : 14 Jan 2026

Keywords:
Vortex-induced vibration
VIV
Turbulence model
Lift coefficient
Drag coefficient

ABSTRACT

In this study, the characteristics of vortex-induced vibration (VIV) of a rigid, smooth circular cylinder elastically mounted in the water flow are investigated. The cylinder has one degree of freedom and is constrained to oscillate only in the vertical direction. The flow Reynolds number lies within the Transition of Shear Layer 3 (TrSL3) region of the subcritical flow regime. The governing equations, namely the continuity and Navier-Stokes equations, are solved using computational fluid dynamics (CFD). The finite volume method is employed for discretizing the equations, implemented through the ANSYS Fluent software. The Pressure Based solver and the PISO algorithm are utilized to couple the equations. The two-dimensional unsteady Reynolds-averaged Navier-Stokes (URANS) equations are solved using the k-ω SST turbulence model. A simplified mathematical model describes the system dynamics and fluid forces associated with the cylinder's vortex-induced vibration. Examination of the vortices shed in the wake region reveals a P+S vortex shedding pattern. Additionally, the time history of the cylinder's displacement ratio exhibits a sinusoidal shape, whereas the recorded lift and drag coefficient data are non-sinusoidal due to the P+S vortex shedding mode. Frequency analysis of the cylinder's response indicates that the oscillation frequency of the cylinder matches the dominant frequency of the lift force. Furthermore, the dominant frequency of the drag force is twice that of the lift one.

1. Introduction

In engineering research, investigating flow behavior around bluff bodies and the fluid-structure interaction (FSI) effects is of paramount importance. The interaction between a bluff body and a fluid flow, depending on the Reynolds number, can lead to various flow regimes and consequently, flow separation in the wake region, resulting in the formation of vortices. At low Reynolds numbers, flow separation does not occur but as the Reynolds number increases, the flow separation gradually initiates, leading to flow instability and the onset of a phenomenon known as vortex shedding with a characteristic frequency. Consequently, the wake region takes the shape of a vortex street. The periodic shedding of vortices induces fluctuating pressure and hydrodynamic forces on the body. The component of this force perpendicular to the flow direction has a frequency similar to the vortex shedding frequency, while the frequency of the component parallel to the flow is twice the vortex shedding frequency [1,2,3]. If the body is free to move, these forces induce oscillatory motion, known as vortex-induced vibration (VIV) [1]. This phenomenon has numerous applications in civil and marine structures. Of particular interest is its use in renewable energy harvesting devices [4].

In this regard, extensive research has been conducted to advance the knowledge in this field and find the key parameters that factor in. The strong dependence of VIV on the Reynolds number has driven numerous research studies to focus on this aspect [5,6,7]. Studies carried out in recent decades have employed a variety of methods including experimental investigations [5,8] as well as numerical simulations [1,9].

While numerous studies have investigated vortex-induced vibration (VIV) of circular cylinders, predominantly at lower Reynolds numbers or through experimental methods [1,5,8], this research distinguishes itself by employing a two-dimensional computational fluid dynamics (CFD) approach with the k-ω SST turbulence model to examine the characteristics of vortex-induced vibration of a single-degree-of-freedom circular cylinder in the TrSL3 region of the subcritical flow regime, as classified by Zdravkovich [10]. This investigation provides novel insights into the P+S vortex shedding mode, characterized by alternating pair and single vortices, which results in non-sinusoidal lift and drag coefficients, a less commonly reported feature in prior numerical analyses. These findings enhance the understanding of fluid-structure interactions in the TrSL3 regime and underscore the efficacy of two-dimensional URANS simulations in capturing complex VIV phenomena at higher Reynolds numbers. Furthermore, recent reviews [11,12] underscore the need to explore such vortex shedding patterns at higher Reynolds numbers, making this work a distinct contribution to understanding fluid-structure interaction in this challenging flow regime.

2. Materials and Methods

2.1. Physical Model

Figure 1 illustrates the schematic of the physical model. This model comprises a rigid, smooth circular cylinder with a diameter D and mass m, elastically mounted in the fluid flow using two linear springs with a stiffness coefficient K. The damping coefficient c represents structural damping, arising from internal friction and applied to the model. The cylinder is mounted horizontally in a cross-flow and constrained to oscillate only in the y-direction.

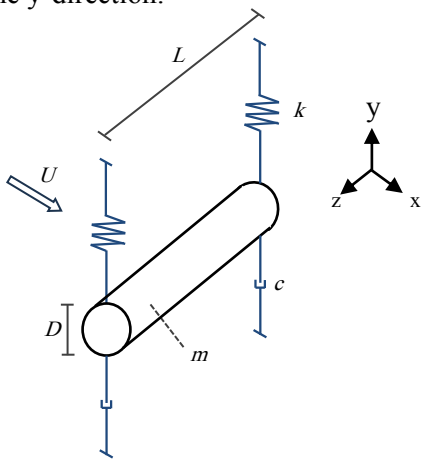

Figure 1. Schematic of the physical model: An elastically mounted circular cylinder with linear spring and damper exposed to a cross-flow.

The water flow is uniform, steady, and directed in the x-direction. Table 1 presents the parameters of the physical model and fluid properties. The system mass includes the effective mass of the spring and the mass of the oscillating cylinder. The Reynolds number of the flow, calculated based on the cylinder diameter D, is 1.25×10^5 which indicates a subcritical flow regime. A characteristic of this regime is a fully turbulent boundary layer and a turbulent wake region.

Table 1. Physical model and the media parameters

Parameter	Symbol	Unit	Value
Cylinder diameter	D	m	0.125
Cylinder length	L	m	0.9144
Total oscillating mass	m_{osc}	kg	12.7
Total system elasticity (stiffness)	K	N/m	1025
System damping	c_{system}	Ns/m	18.5
System natural frequency in water	$f_{n,water}$	Hz	1.04
Fluid dynamic viscosity	μ	Ns/m^2	0.001003
Fluid density	ρ	kg/m^3	998.2
Nondimensional mass, mass ratio	m^*	-	1.12

2.2 Governing Fluid Flow Equations and Turbulence Model

The governing fluid flow equations are the continuity and Navier-Stokes equations. These equations were solved using computational fluid dynamics (CFD). The finite volume method was employed to discretize the equations, implemented through the ANSYS Fluent software. The Pressure Based solver and the PISO algorithm were utilized to couple the equations. The k-ω SST turbulence model was employed to solve the unsteady Reynolds-averaged Navier-Stokes (URANS) equations.

2.3 Mathematical Model

A simplified mathematical model describes the system dynamics and fluid forces associated with the vortex-induced vibration of the cylinder. The motion of the cylinder in the y-direction, perpendicular to both the flow direction and the cylinder's axis, is modeled by a second-order linear equation, as described in Eq. (1).

$$m_{osc}\ddot{y} + c_{system}\dot{y} + K_{spring}y = F_{fluid,y} \quad (1)$$

where y represents the cylinder displacement, m_{osc} is the mass of the oscillating system which includes one third of the spring mass, K_{spring} is the spring stiffness, c_{system} is the system damping coefficient, and $F_{fluid,y}$ is the force exerted by the fluid on the body in the y-direction. Due to the periodic nature of vortex shedding, the pressure on the cylinder surface also undergoes periodic fluctuations. Consequently, there are periodic variations in the forces applied to the cylinder surface. The force resulting from the pressure

distribution can be divided into two components: one perpendicular to the flow (the lift force, F_L) and the other parallel to the flow (the drag force, F_D). The lift force emerges when vortex shedding initiates and oscillates at the same frequency as the vortex shedding. Concurrently, the drag force also oscillates similarly to the lift force. It should be noted that the drag force, in addition to its fluctuating component, also has a constant component that arises from friction and pressure difference.

3. Results

Figure 2 shows the vortices formed in the wake region, which appear as a single vortex on one side of the vortex street and a pair of vortices on the other side.

After the cylinder's transient response, the vortex shedding pattern is such that in one half-period of the cylinder's oscillation, a single vortex forms and sheds, while in the next half-period, two vortices shed into the wake.

The displacement ratio time history (Figure 3, up) demonstrates that the cylinder undergoes oscillatory motion perpendicular to the flow due to periodic forces induced by vortex shedding. The maximum amplitude of cylinder oscillation obtained in this study is 0.086 m, and the maximum non-dimensional oscillation amplitude (ratio of oscillation amplitude to cylinder diameter) is 0.69. These values were determined after the stabilization of cylinder oscillation and following the transient response. According to the calculations, the root mean square value of the nondimensional displacement ($y^*_{R.M.S.}$) is 0.46. Furthermore, this oscillatory motion has a frequency of 1.1 Hz. Figure 3 (down) depicts the FFT analysis of displacement ratio.

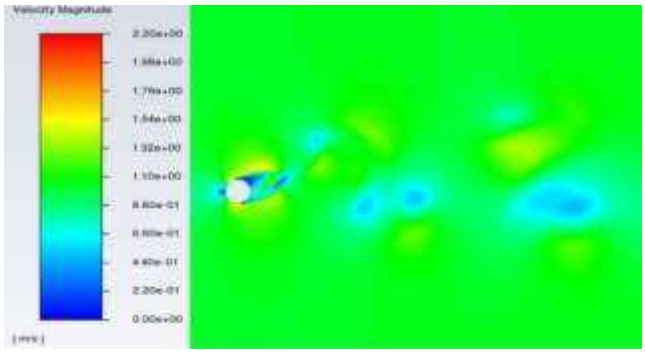

Figure 2. Vortex shedding behind the cylinder according to the velocity magnitude

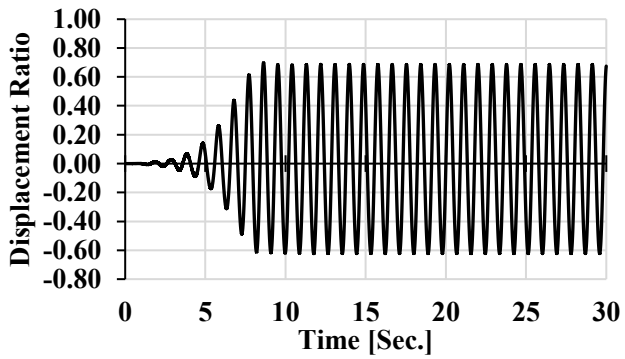

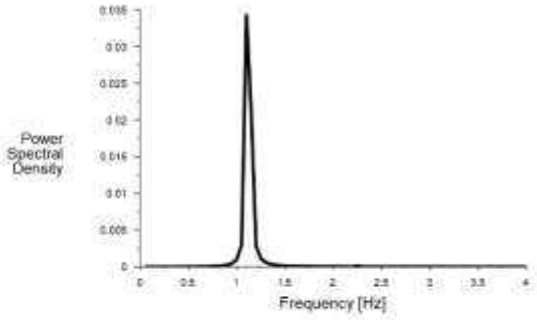

Figure 3. (Up) Time history and (down) frequency spectrum of the cylinder displacement ratio

As mentioned, periodic vortex shedding generates an oscillating lift force, inducing the transverse oscillatory motion of the cylinder. Figure 4 (up) shows time records of the lift coefficient. The maximum value of the lift coefficient after the stabilization of cylinder oscillation is 0.93, and the minimum value is -0.56. Moreover, its time-average value is 0.06. Based on the calculations, the R.M.S. value of the lift coefficient ($C_{l,R.M.S.}$) is 0.44. The FFT analysis indicates that the predominant frequency of the oscillating lift coefficient is 1.1 Hz, with additional frequency components at 2.25 Hz and 3.35 Hz (Figure 4, down).

The maximum value of the drag coefficient after the stabilization of cylinder oscillation is 2.89, and its time-average value is 2.09. Furthermore, the dominant frequency of the drag force, according to the FFT analysis, is 2.25 Hz. The time history of the drag coefficient and its components frequencies are shown in Figure 5.

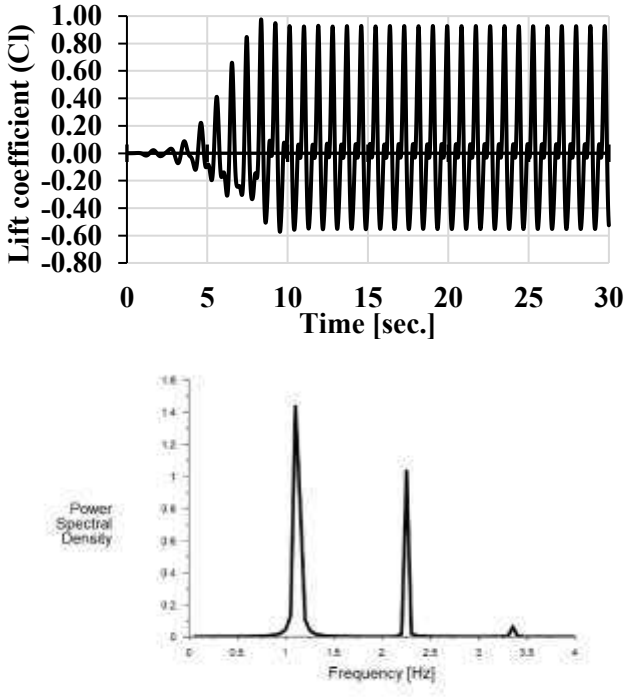

Figure 4. (up) Time records of the lift coefficient and (down) its frequency spectrum

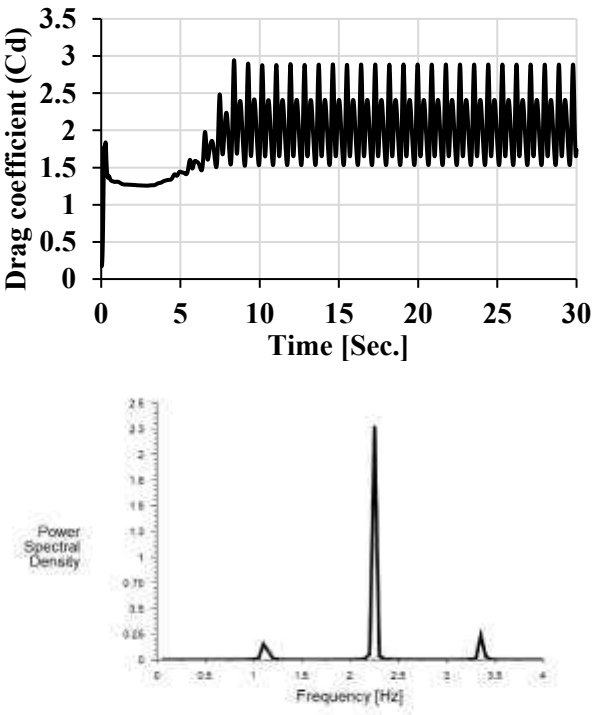

Figure 5. (up) Time records of the drag coefficient and (down) its frequency spectrum

4. Discussion

The Reynolds number of 1.25×10^5 corresponds to a subcritical flow regime. In this regime, the boundary layer transitions from laminar to turbulent, and the wake region is also turbulent. The shedding vortices in the subcritical regime, exhibit a high degree of organization, as evident in Figure 2. Due to the oscillatory motion of the cylinder in the fluid, different wake structures can be created downstream of the flow. These structures are influenced by various factors such as the Reynolds number, cylinder surface roughness, cylinder end conditions, length-to-diameter ratio of the cylinder, and structural characteristics. As observed in Figure 2, in each oscillation period of the cylinder, a pair of vortices is shed on one side of the Kármán Street and a single vortex on the other side, corresponding to the P+S mode.

After the transient response of the cylinder, the displacement ratio time history exhibits a sinusoidal shape, bounded by a value of 0.7. A compilation of data of the displacement ratio from other researchers is presented in Table 2. To interpret the discrepancies in the cylinder response, understanding the characteristics of the flow regime and the near-wake region is crucial.

Table 2. Vortex induced vibration displacement ratio data

Investigators	Reynolds number	m*ζ	A/D
Sahu et al. [13]	50000	N.A	0.51
Abbaspour et al. [9]	80000	N.A	0.62
Vikestad et al. [14]	14000-65000	0.012	1.13
Present experiments	125000	0.066	0.69
Raghavan [15]	8000-150000	0.251	1.97
Ding et al. [16]	70000-250000	N.A	2.0
Sahu et al. [13]	150000	N.A	0.75
Sahu et al. [13]	300000	N.A	0.39

Figure 6 illustrates the phase difference between the displacement ratio of the cylinder and the lift coefficient. The presence of a phase difference between the cylinder displacement and the lift force indicates a time delay in the structural response to the applied forces. The lift coefficient time history (Figure 4, up) does not exhibit a sinusoidal pattern and displays two peaks in each half-period of cylinder oscillation. The values of these two peaks differ significantly, with the smaller peak being less than 0.1. Consequently, the lift coefficient remains near zero for an extended duration. The non-sinusoidal nature of the lift coefficient arises from the vortex shedding pattern in the wake. The vortex shedding, in accordance with a specific pattern and interactions between shed vortices, generates multiple oscillatory components within the lift force, each characterized by distinct frequency, phase, and amplitude. Figure 4 (down) illustrates the power spectral density of the lift coefficient. The frequencies of components with lower power are approximately 2 and 3 times the dominant frequency. The dominant frequency of the lift coefficient is 1.1 Hz, which coincides with the frequency of the cylinder oscillation. The non-zero time-averaged lift coefficient, resulting from the difference between its maximum and minimum magnitudes, indicates an asymmetry in the time-series data of the lift coefficient. This asymmetry in the positive and negative amplitudes of cylinder motion stems from the wake structure and the presence of the P+S mode in vortex shedding. In other words, the alternation in the number of vortices shed in successive half-periods of cylinder oscillation results in unequal pressure forces being applied to the cylinder in the positive and negative amplitudes of oscillation. The positive values of the lift coefficient are bounded by a value of 1, and the negative values by -0.6.

Table 3 compares the C_l with results reported by other researchers in the subcritical flow regime. In this regime, the boundary layer transitions from laminar to turbulent. This transition influences the vortex shedding frequency, vortex strength, and, consequently, the lift forces. It can be observed that the lift coefficient increases with increasing Reynolds number. Figure 7, presented by Norberg [17], also illustrates $C_{l,\,R.M.S}$ versus Re. The results of the present study align with this figure.

Table 3. Vortex induced vibration Maximum and R.M.S. lift coefficient data

Investigators	Reynolds number	$C_{l,max}$	$C_{l,R.M.S.}$
Khalak and Williamson [18]	1700	-	0.03
Khalak and Williamson [18]	9750	-	0.25
Khalak and Williamson [18]	12500	-	0.29
Abbaspour et al. [9]	80000	0.80	-
Present experiments	125000	0.93	0.44
Sahu et al. [13]	150000	-	1.25

The rapid increase in the drag coefficient at the beginning of the its time history diagram (Figure 5, up) is attributed to the development of the initial flow and the formation of the boundary layer. After the transition from initial conditions, leading to the development of a stable wake behind the cylinder, periodic fluctuations in the drag coefficient occur, which is a characteristic of VIV and a consequence of the periodic shedding of vortices from the cylinder surface.

The drag force, like the lift one, is composed of several oscillatory components with different frequencies, caused by vortex shedding from the cylinder surface. As a result, the drag coefficient exhibits a non-sinusoidal oscillation, as shown in Figure 5 (up). The periodic part of the drag coefficient time history is bounded by the values of 1.5 and 2.9. Frequency analysis of the drag coefficient (Figure 5, down) reveals that the dominant frequency is 2.25 Hz, with contributions from other significant components at 1.1 and 3.35 Hz.

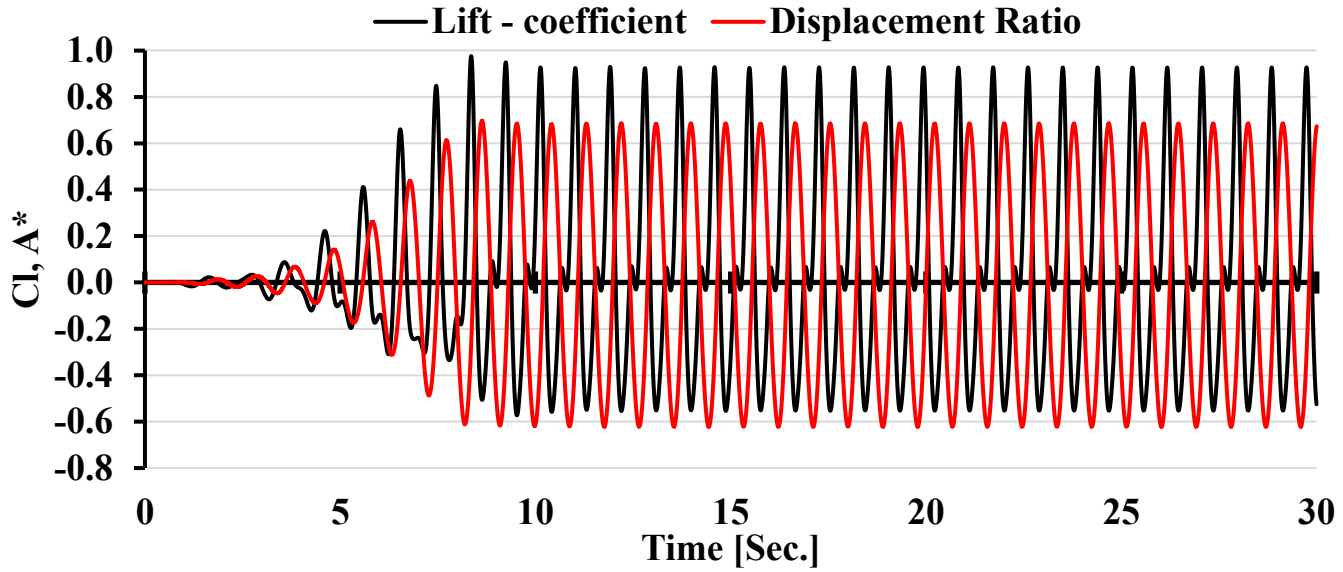

Figure 6. Time records of the lift coefficient and displacement ratio

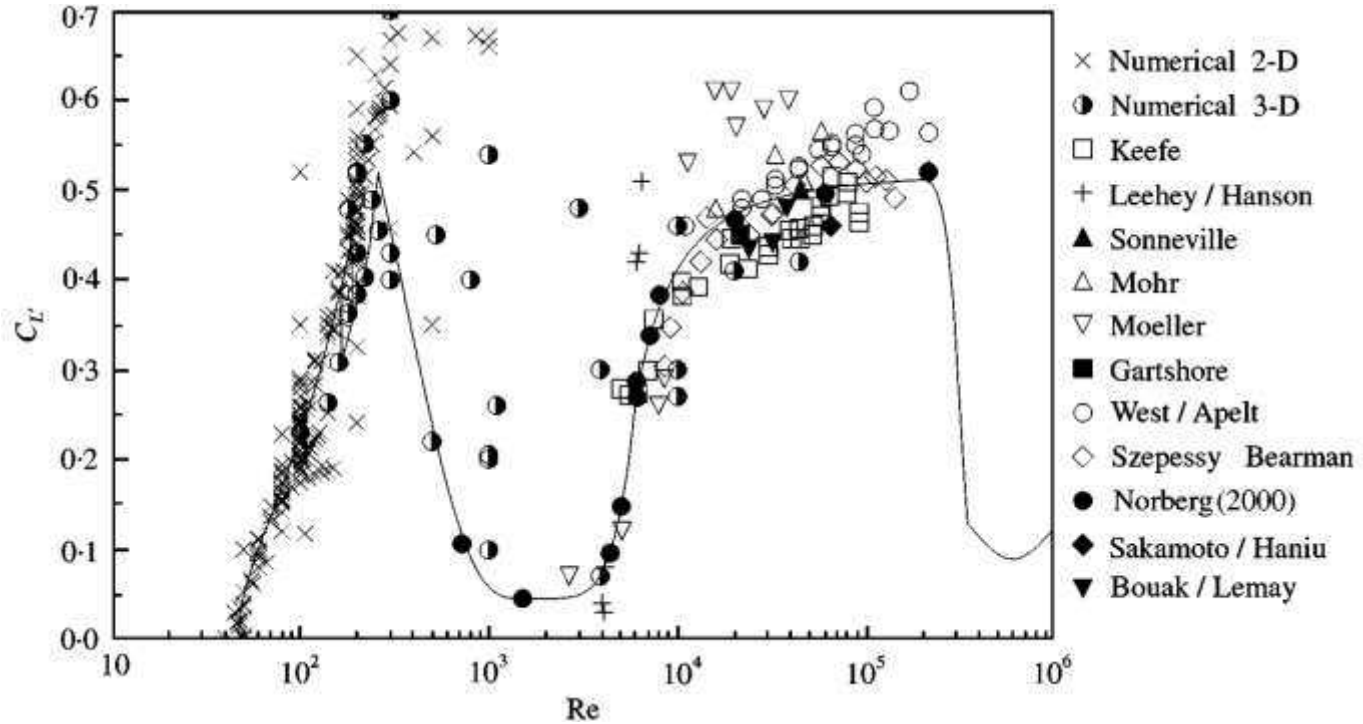

Figure 7. Fluctuating lift coefficient plotted versus Reynolds number [Reproduced from Norberg (2000)]

The drag coefficient oscillates at roughly double the frequency of the lift coefficient. This is because the lift force requires a full cycle of vortex shedding from both sides of the cylinder to complete its oscillation. In contrast, the drag force undergoes a full oscillation cycle with vortex shedding from each side of the cylinder [19]. Table 4 presents the mean drag coefficient (C_d) values at the end of the subcritical regime. With increasing Reynolds number and approaching the critical regime, the drag coefficient decreases. This is due to the elongation of the vortex formation region [10]. The high value of the drag coefficient results in increased energy dissipation within the fluid-structure system, influencing the amplitude of cylinder oscillation. Consequently, the displacement ratio of the cylinder (Table 2) in the present study is lower than that reported by Sahu et al. [13].

Table 4. Vortex induced vibration mean drag coefficient data

Investigators	Reynolds number	$\overline{C_d}$
Present study	125000	2.09
Sahu et al. [13]	150000	0.95

5. Conclusions

Simulation of the single degree of freedom vortex-induced vibration (VIV) of a rigid circular cylinder elastically mounted was implemented by solving unsteady Reynolds-averaged Navier-Stokes equations using the k-ω SST turbulence model in the Transition of Shear Layer 3 (TrSL3) region of the subcritical flow regime. The following results were obtained and discussed. First of all, the vortices shed in the wake were well-organized. The vortex shedding pattern was shown in one period of cylinder oscillation. In this regard, P+S vortex pattern mode was observed. Second, the cylinder exhibited a sinusoidal oscillatory motion perpendicular to the flow direction, driven by the periodic forces induced by vortex shedding. Oscillatory motion occurs at the same frequency as the dominant frequency of lift force fluctuations, but with a time lag caused by structural delays in responding to the applied force. In the presence of the P+S vortex shedding mode, the time histories of the lift and drag forces exhibited non-sinusoidal behavior. Instead, they were composed of the superposition of multiple oscillatory components with varying frequencies and amplitudes. FFT analysis of the lift and drag coefficients revealed the dominant frequency as well as other frequencies. According to this analysis, the dominant frequency of the drag coefficient was twice that of the lift coefficient. And finally, compared to previous studies, it was observed that a larger drag coefficient was associated with a smaller amplitude of oscillation. This is attributed to the fact that higher drag coefficients result in greater energy dissipation from the system, which in turn affects the displacement of the cylinder.

6. Acknowledgment

The authors express profound gratitude to Dr. Narges Amrollahi Biuki, associate professor of University of Hormozgan, for her exceptional contributions to this work.

7. References

1. Williamson, C.H.K., & Govardhan, R., (2004). Vortex-induced vibrations. Annu Rev Fluid Mech 36, 413–455. https://doi.org/10.1146/annurev.fluid.36.050802.122128.
2. Sarpkaya, T., (2004). A critical review of the intrinsic nature of vortex-induced vibrations, Journal of Fluids and Structures, 19(4), 389–447. https://doi.org/10.1016/j.jfluidstructs.2004.02.005
3. Zhang, J., & Tang, Y., (2022). Numerical study on vortex-induced vibration of a circular cylinder near a plane boundary at low Reynolds numbers, Applied Ocean Research, 119, 103028. https://doi.org/10.1016/j.apor.2021.10302
4. Hafizh, M., Muthalif, A.G.A., Renno, J., Paurobally, M.R., Bahadur, I., Ouakad, H., Sultan Mohamed Ali, M., (2022). Vortex induced vibration energy harvesting using magnetically coupled broadband circular-array piezoelectric patch: Modelling, parametric study, and experiments, Energy Conversion and Management, 276 (2023) 116559**.** https://doi.org/10.1016/j.enconman.2022.116559
5. Raghavan, K, & Bernitsas, M.M., (2011). Experimental investigation of Reynolds number effect on vortex induced vibration of rigid circular cylinder on elastic supports., Ocean Eng 38(5–6), 719–731. https://doi.org/10.1016/j.oceaneng.2010.09.003
6. Martins, F.A.C., Avila, J.P.J., (2019). Effects of the Reynolds number and structural damping on vortex-induced vibrations of elastically-mounted rigid cylinder, International Journal of Mechanical Sciences, Volume 156, June 2019, Pages 235-249. https://doi.org/10.1016/j.ijmecsci.2019.03.024
7. Gu, J., Fernandes, A.C., Han, X., Kuang, X., Chen, W., (2022). Numerical investigation of Reynolds number effects on vortex-induced vibrations at low and moderate Re regimes, Ocean Engineering, Volume 245, 1 February 2022, 110535. https://doi.org/10.1016/j.oceaneng.2022.110535
8. Narendran, K., Murali, K., & Sundar, V., (2014). Vortex-induced vibrations of elastically mounted circular cylinder at Re of the O (10^5), J Fluids Struct 54:503–521. https://doi.org/10.1016/j.jfluidstructs.2014.12.006

9. Abbaspour, M., Nematikourabbasloo, N., & Mohtat, P., (2022). Numerical simulation of vortex-induced vibration of a smooth circular cylinder at the subcritical regime, Proceedings of the Institution of Mechanical Engineers, Part M: Journal of Engineering for the Maritime Environment. 236(4), 916-937. https://doi.org/10.1177/14750902221088
10. Zdravkovich, M. M., (1990). Conceptual Overview of Laminar and Turbulent Flows Past Smooth and Rough Circular-Cylinders, Journal of Wind Engineering and Industrial Aerodynamics, 33(1-2), 53-62. https://doi.org/10.1016/0167-6105(90)90020-D
11. Hong, K. S., Shah, U. H., (2018). Vortex-induced vibrations and control of marine risers: A review. Ocean Engineering, 152, 300–315. https://doi.org/10.1016/j.oceaneng.2018.01.086.
12. Zhao, M., (2023). A review of recent studies on the control of vortex-induced vibration of circular cylinders. Ocean Engineering, 285(Part 2), 115389. https://doi.org/10.1016/j.oceaneng.2023.115389.
13. Sahu, T.R., Chopra, G., & Mittal, S., (2021). Vortex-Induced Vibration of a Circular Cylinder at High Reynolds Number, In: Braza, M., Hoarau, Y., Zhou, Y., Lucey, A.D., Huang, L., Stavroulakis, G.E. (eds) Fluid-Structure-Sound Interactions and Control, FSSIC 2019. Lecture Notes in Mechanical Engineering. Springer, Singapore. https://doi.org/10.1007/978-981-33-4960-5_30
14. Vikestad, K., Vandiver, J. K., & Larsen, C. M., (2000). Added Mass and Oscillation Frequency for a Circular Cylinder Subjected to Vortex-Induced Vibrations and External Disturbance, Journal of Fluids and Structures, 14(7), 1071-1088. https://doi.org/10.1006/jfls.2000.0308
15. Raghavan K., (2007). *Energy Extraction from a Steady Flow Using Vortex Induced Vibration*, Ph.D. thesis, University of Michigan.
16. Ding, J., Balasubramanian, S., Lokken, R., & Yung, T., (2004). *Lift and Damping Characteristics of Bare and Staked Cylinders at Riser Scale Reynolds Numbers*, [Paper presentation]. Proceedings of Offshore Technology Conference, Houston, Texas, May 2004, Paper No. 16341. https://doi.org/10.4043/16341-MS
17. Norberg, C., (2000). Flow around a Circular Cylinder: Aspects of Fluctuating Lift, Journal of Fluids and Structures, 15(3-4), 459-469. https://doi.org/10.1006/jfls.2000.0367
18. Khalak, A., & Williamson, C. H. K., (1999). Motions, Forces and Mode Transitions in Vortex-Induced Vibrations at Low Mass-Damping, Journal of Fluids and Structures, 13(7-8), 813-851. https://doi.org/10.1006/jfls.1999.0236
19. Rafati Zarkak, M., Barati, E., & Abolfazli Esfahani J., (2019). Numerical Study of Energy Harvesting of Vortex Induced Vibration Phenomenon of Circular Cylinder with Various Sectors at Low Reynolds Number, Modares Mechanical Engineering. 19(7), 1687-169. DOR: 20.1001.1.10275940.1398.19.7.6.2

INTERNATIONAL JOURNAL OF
COASTAL, OFFSHORE & ENVIRONMENTAL ENGINEERING IJCOE Vol.1 •/No. 4/ Autumn 2025 (35-45)

Available online at: www. Ijcoe.org

Numerical Simulation of Plate Scour Around Offshore Platforms and Strategies to Prevent it

Seyed Amirhosein Mirabotalebi[1], Mehdi Nezhadnaderi[2]* and Reza Zahedi [3] Mohammad Gholami[4], Taha Mehrzad[5] andAli Sheykhbahaei[6]

[1)] Department of Civil Engineering, To.C., Islamic Azad University, Tonekabon, Iran. 2270123301@gmail.com
[*2)] Department of Civil Engineering, To.C., Islamic Azad University, Tonekabon, Iran. (Corresponding Author).
*mehdi.nezhadnaderi@iau.ac.ir
[3)] Department of Civil Engineering, To.C., Islamic Azad University, Tonekabon, Iran.
2219185427@iau.ir
[4)] Department of Civil Engineering, Tonekabon Branch, Islamic Azad University, Tonekabon,
2092366262@iau.ir
[5)]Department of Civil Engineering, To.C., Islamic Azad University, Tonekabon, Iran.
22701499114@iau.ir
[6)] PhD Candidate in Physical Oceanography at university of Hormozgan/ Iranian National Institute for Oceanography and Atomospheric science, Ali.sheykhbahaei@inio.ac.ir
*mehdi.nezhadnaderi@iau.ac.ir (*Corresponding author's email)

ARTICLE INFO

Article History:
Received: 25 MAY 2025
Accepted: 20 JAN 2026

Keywords:
Offshore platform baselines, flow patterns, scouring, barrier plates, pressure gradient.

ABSTRACT

With the increase in construction in the sea, protective structures are considered to prevent their instability in the marine environment. Among the coastal protective structures, submerged plates are used in marine structural engineering to prevent scour. Therefore, it is very important to study and understand the erosion and sedimentation process in the area of the offshore platform base lines in terms of design, protection and maintenance. In this research, using the computational fluid dynamics method and Fluent software, the flow around the submerged offshore platform base was simulated with different Reynolds number states. The results of the iso velocity lines, m/s, show that the speed decreases behind the offshore platform base. The maximum speed is below the offshore platform base line, which will cause scour. By increasing the Reynolds number from 3000 to 7000, the maximum speed in this state increases. The results of the iso pressure lines in Pascals show that the pressure behind the base presses and decreases above and below it. The maximum negative pressure is below the base line of the offshore platform, which will cause scouring. As the Reynolds number increases from 3000 to 7000, the negative pressure in this case increases from -0.07 to -0.3 in Pascal, which will cause scouring. The maximum pressure is below the base line of the offshore platform, which is significantly higher than the case without the use of plates, which reduces the risk of scouring around the base.

1. Introduction

Much research has been done on the investigation of scour around offshore platform baselines, but the main

1,3, 4, MSc
2) Associate Professor
5) MSc student

difference of this research from previous similar cases is the consideration of subsurface slabs under the offshore platform base. Installing impermeable slabs causes the underground flow lines formed under the bed, located under the offshore platform baselines, to be lengthened, as a result of which the pressure gradient across the offshore platform base is reduced. Reducing the pressure gradient is one of the main and most fundamental factors in the formation and development of scour under the offshore platform baselines and the formation of the sluice phenomenon in the bed under the offshore platform baselines. This phenomenon is considered as one of the results of the pressure gradient prevailing over the submerged weight of bed sediment particles.

With the increase in construction in the sea, the use of protective structures to prevent their instability in the marine environment is of interest. Among the coastal protection structures, submerged slabs are used to prevent scour, which are used in marine structural engineering.

There is a hydraulic perspective that studies the distribution of hydrodynamic components around the offshore platform baseline. In fact, this perspective discusses and studies the formation and expansion of eddy currents around the offshore platform baseline through numerical simulations and attempts to accurately estimate the effect of this phenomenon on the amount of hydrodynamic components and the intensity of the effect of eddy formation. Sumer and Fredsoe (1997) studied various environmental conditions (waves and currents) and their effects on the forces acting on the offshore platform baseline. In their research, these researchers often compared their results with the laboratory work of other researchers and confirmed their research based on that. According to the research of these researchers, waves and currents have two completely separate effects on the environment around the offshore platform baseline, the intensity of which can be expressed by the dimensionless Reynolds numbers for the flow and the Cloghan-Carpenter number for the wave. These two dimensionless numbers represent the behavioral properties of the flow and wave, respectively. They also showed that the forces acting on the offshore platform baseline are caused by the effects of environmental conditions in a completely dynamic manner, and the studies conducted by Morrison only calculated the average force acting on the offshore platform baseline. They also introduced the use of the Strouhal number as a suitable method for obtaining the frequency of eddy currents. On the other hand, Cheng and Chew in 2002, using the numerical solution of the fundamental laws of fluids, came up with various hydrodynamic components in the area around the offshore platform baseline. They simulated the conditions of the flow effect in the environment around the offshore platform baseline by formulating and precisely defining the boundary conditions and using the k-4 turbulence model. Cheng and Chew investigated the self-burial effect for unburied offshore platform baselines by adding a rectangular appendage to the offshore platform baseline and comparing the results of the pressure distribution under the new conditions and before adding the appendage. The research of these authors showed that using a numerical model by considering an appropriate turbulence model can easily obtain the amount of various hydrodynamic components around the offshore platform baseline. Liang also stated in his research, which he conducted in collaboration with Cheng in 2004, that the vertical simulation of the flow around the offshore platform baseline using the basic laws of fluids and using one of the types of turbulence modeling methods, is very effective in reducing the cost of studies by various researchers. They confirmed the accuracy of their simulation by comparing their results with the laboratory work done by Jessen (1986). It should be noted that according to Jessen's studies, changing the scale of the problem from the real situation and only considering the ratio of water depth to the diameter of the offshore platform baseline and maintaining the Reynolds number is quite practical and acceptable. In the following, it is necessary to introduce some of the concepts and tools of this division based on which these researchers studied eddy currents.

Reynolds number

This number is used to determine the range of motion of eddies (choi 2000).

$$Re=UD/\upsilon \quad (1)$$

where υ: kinematic viscosity of the fluid, U: flow velocity perpendicular to the offshore platform baseline and D: outer diameter of the offshore platform baseline. Based on the Reynolds number and the observations that researchers made by studying the formation mechanism around the offshore platform baseline, the intensity and formation of vortices can be classified based on the Reynolds number. Among the most important research in this perspective, we can also mention the studies conducted by Sumer Fredose in 1997. These researchers, by dividing the type of fluid space around the offshore platform baseline into two types: permanent and non-permanent

for two different general cases of the presence of the flow effect and the presence of the wave effect, tried to investigate the formation and expansion of vortical flows around the offshore platform baseline resulting from this phenomenon.

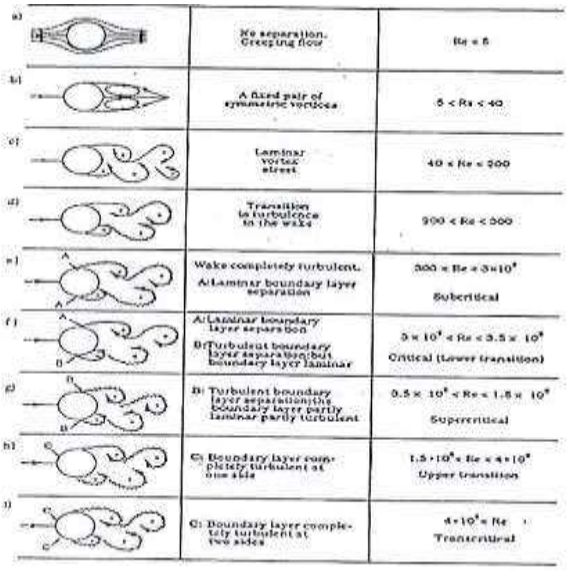

Figure (1): Intensity and formation of vortices based on the Reynolds number (Fredsoe and Sumer in 1997)

shows these different classifications based on the Reynolds number.

As can be seen in Figure (1), for low Reynolds numbers, no separation will be observed behind the offshore platform baseline. In fact, for Zeinolds numbers greater than 5 to 40, a pair of vortices with a fixed shape will be created behind the offshore platform baseline, and the length of the turbulent effect will increase with increasing Reynolds number (Batchelor in 1967). When the Reynolds number of the flow is greater than 40, the shadow of the vortices behind the offshore platform baseline becomes unstable and the turbulence behind the offshore platform baseline is defined by a phenomenon called eddy currents, as a result of which the shadow of the flow appears with eddy lines. When the Reynolds number is in the range (40>Re>200), the eddy lines will appear as layered flows behind the offshore platform baseline. In these cases, the shadow of the eddies is defined as two-dimensional.

With further increase in the Reynolds number, the type of flow behind the offshore platform base changes from a transition flow to a turbulent flow. According to Bloor (1964), when the Reynolds number of the flow is in the range between (200>Re>300) in the area behind the offshore platform base line, the turbulent flow behind the offshore platform base moves towards the offshore platform base line and when the Reynolds number of the flow reaches 400, a turbulent eddy is formed. Observations have shown that a two-dimensional eddy formed in the Reynolds number range (200>Re>40) changes from a two-dimensional state to a three-dimensional state.

The flow with Reynolds number around the offshore platform base line remains completely stratified, and for the flow condition with Reynolds number (3×10^5>Re>40), the flow in the area behind the offshore platform base line is known as the subcritical state. When the flow Reynolds number exceeds this value, the boundary layer state will change from a transitional to a turbulent state. This transition occurs first at the separation point and then moves upstream. For limited flow conditions, when the Reynolds number is in the range (3.5×10^5>Re>3×10^5), the boundary layer at the separation point appears completely turbulent. However, these two states occur only on one side of the offshore platform base and on the other side (the upstream side) it will remain a calm layer. This state is known as the critical flow regime and causes the lift force to be opposite to zero.

When the Reynolds number of the flow reaches 1.5×10^6, the boundary layer on one side of the offshore platform baseline becomes completely turbulent, while on the other side of the offshore platform baseline the flow becomes semi-turbulent. This type of flow regime is known as the upper-transition region, and finally, when the Reynolds number exceeds 4.5×10^6, the boundary layer located on the offshore platform baseline will become completely turbulent at all points.

Mechanism of Vortex Movement

As mentioned, for Reynolds values higher than 40, the boundary layer located on the offshore platform baseline will be separated from the offshore platform baseline due to the unfavorable pressure gradient behind the offshore platform baseline by the formation of a pair of stationary vortices. In this case, a phenomenon as shown in Figure (2) will be formed behind the offshore platform baseline. As can be seen in Figure (2), the boundary layer formed around the offshore platform baseline has characteristic values of local vorticity.

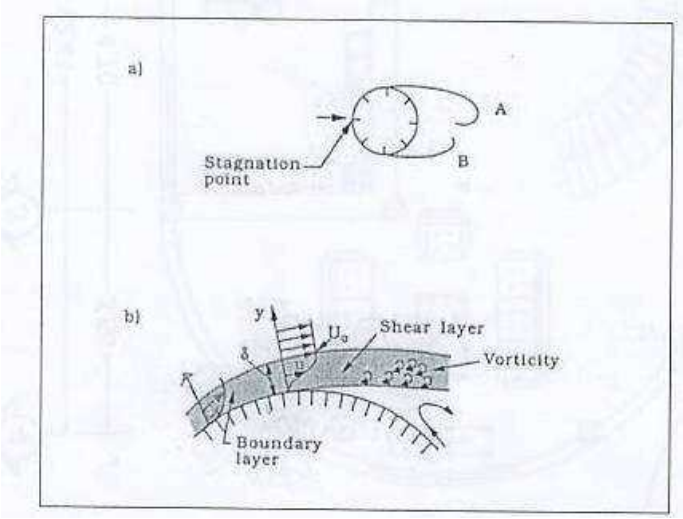

Figure (2): Location of the separation point in front of the offshore platform baseline and the development of the shear layer behind the offshore platform baseline.

These vortices are formed within the boundary layer, develop, and cause rotation of a vorticity with a specific shape above and below the offshore platform baseline.

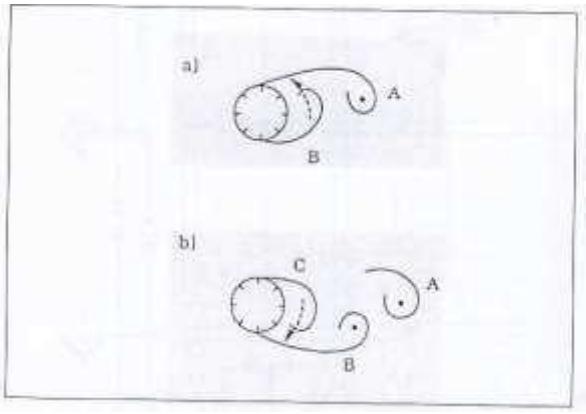

Figure (3): How vortical flows develop behind the offshore platform baseline
(Gerrard in 1966)

In fact, the motion of vortices is unstable for flow Reynolds numbers greater than 40, and the direction and manner of motion of vortices can be justified based on the opinion of Gerrard in 1966. Based on Figure (3), he assumed that vortex A starts earlier than vortex B and the direction of vortex formation is opposite to each other. If vortex A is expanding clockwise and vortex B is expanding counterclockwise, vortex B will cause vortex A to break away from the boundary layer and vortex A will separate and move downstream as a free vortex. This expansion will then produce vortex C and similarly, in the opposite direction, will cause vortex B to separate from its source of generation. This process will be repeated periodically over time behind the offshore platform baseline.

In fact, the motion of vortices is unstable for flow Reynolds numbers greater than 40, and the direction and manner of motion of vortices can be justified based on the opinion of Gerrard in 1966. Based on Figure (3), he assumed that vortex A starts earlier than vortex B and the direction of vortex formation is opposite to each other. If vortex A is expanding clockwise and vortex B is expanding counterclockwise, vortex B will cause vortex A to break away from the boundary layer and vortex A will separate and move downstream as a free vortex. This expansion will then produce vortex C and similarly, in the opposite direction, will cause vortex B to separate from its source of generation. This process will be repeated periodically over time behind the offshore platform baseline. The motion of water particles in a wave is a continuous unsteady flow. When this unsteady flow collides with a rigid body of a submerged structure, a force is exerted on the body due to the flow velocity and the flow acceleration.

The flow velocity creates a drag force Fd that acts on the body of the submerged structure and is due to the frictional shear stress and the total pressure, which is usually calculated by the following formula:

$$F_d = \frac{C_d}{2}\rho A u^2 \quad (2)$$

A is the distance of the cross section perpendicular to the flow surface. In equation (2) u is the flow velocity reaching the body, ρ is the density of the liquid, cd is the drag coefficient that depends on the cross section shape, flow direction, surface roughness and the Reynolds number of the flow.

For a cylinder, the Reynolds number is R=UD/υ, where D is the diameter of the cylinder and υ is the kinematic viscosity of the flow.

When a flow is accelerated over a surface, the flow velocity and hence the Reynolds number and, in some cases, the continuous elastic coefficient change. Therefore, since u and Cd are both variable in an accelerated flow, the elastic force of equation (2) can change considerably.

The acceleration of the flow produces an additional force on the body, in addition to that given in equation (2). This acceleration or inertial force has two components. The first component is due to the acceleration of the flow due to the pressure difference in the accelerating flow field. This pressure difference creates a variable pressure on the surface of the body of the body, which creates a net force on the body. Also, when an accelerated flow passes over a body, an additional mass of fluid is created due to the presence of the body in motion. When the flow passing over a stationary surface is accelerated, there will be an additional mass that creates a force on the body. This second component is related to the inertial force, a function of the density and acceleration of the fluid, as well as the shape of the object and its volume.

Therefore, when there is an unsteady flow, the total instantaneous hydrodynamic force F on the object can be written as:

$$F = \frac{C_d}{2}\rho A u^2 + \int_A P_x dA + K\rho V \frac{du}{dt} \quad (3)$$

The second term on the right, where Px is the pressure exerted on the body of the object in the direction of the flow and dA is the change in the area of the place where the pressure is exerted, is the inertial force due to the acceleration of the pressure difference of the flow field. The third term on the right is the added mass (Khosro Bargi).

In the present study, first the effect of offshore platform baselines with their different diameters on the scouring process is investigated; then by installing an impermeable subgrade sheet in front of the offshore platform baselines, the effect of this sheet on the scouring phenomenon is studied.

In this study, the flow simulation after the construction of the submerged sheet was investigated using the computational fluid dynamics method and Fluent software.

2. Methods

A critical review of available turbulence models with the aim of evaluating their suitability for use in hydraulic problems is valuable and needed. This

was done by Professor Wolfgang Reddy with years of experience in the development and application of these models. In the book ((turbulence models and their application in hydraulics)), he introduced the topic of turbulence modeling in a simple way that can be understood by any reader with basic knowledge in the field of fluid mechanics and summarized the latest published articles in this field. is In the first chapter, the role of turbulence models is explained (Salehi Nishabouri and Nasiri Saleh, 2017).

Basic conservation laws are expressed by exact equations (Navier-Stokes equations). They describe all the details of fluid movement. Since there is little hope to solve these equations and also due to the lack of interest of engineers in the details of oscillatory motion, a statistical approximation (which was first proposed by Asburn Reynolds) was used and these equations, on the time scale - which in The comparison with the time scale of turbulent motion is large - they were averaged.

Unfortunately, the averaging operation creates a new problem that the equations cannot form a closed system, because they contain unknown sentences that describe the transfer of the amount of motion, heat, and average mass by means of turbulent motion. This system of equations can be closed only by using experimental input, therefore, calculation methods based on averaged flow equations are semi-empirical.

The so-called field methods - which use the original partial differential equations - require the specifications of the turbulent transfer terms that appear in the equations at every point of the flow. This specification is defined by using the equations (algebraic or differential) that determine the turbulent transfer terms in the average flow equations, and the system of equations is closed using those equations. The basis of chaos models are hypotheses about chaotic processes that require experimental input in the form of constants or functions. They do not simulate the details of the turbulent motion, but simply "simulate the effect of turbulence on the behavior of the average flow" (Salehi Nishabouri and Nasiri Saleh, 2017).

In this study, flow is unsteady with two-dimensional turbulence form. Velocity and pressure are a function of time and space. To model of the velocity and pressure fluctuations is the integrated from the Navier Stokes equation at time. Integration of Navier Stokes equations at time is known Reynolds equations (Reynolds, 1984). Turbulence model equations are two equation models k-ε (Standard) that have be averaged in depth (Rastogi and Reddy, 1978). ε equation is as one of the main sources of the limitations of accuracy of the standard version of the k-ε model and the Reynolds stress model. It is interesting that k-ε model includes a correction term that is dependent to strain with c13 constant in the ε equation of RNG model (Yakhot et al, 1992). WillCox provided turbulence equations of k-ω (standard) model (WillCox, 1988).

$$\frac{\partial u}{\partial x}+\frac{\partial v}{\partial y}+\frac{\partial w}{\partial z}=0 \quad (4)$$

$$\frac{\partial \rho u}{\partial t}+\frac{\partial \rho uu}{\partial x}+\frac{\partial \rho uv}{\partial y}+\frac{\partial \rho uw}{\partial z}-\rho f_c v=-\frac{\partial P}{\partial x}+\frac{\partial \tau_{xx}}{\partial x}+\frac{\partial \tau_{xy}}{\partial y}+\frac{\partial \tau}{\partial z} \quad (5)$$

$$\frac{\partial \rho v}{\partial t}+\frac{\partial \rho uv}{\partial x}+\frac{\partial \rho vv}{\partial y}+\frac{\partial \rho vw}{\partial z}+\rho f_c u=-\frac{\partial P}{\partial y}+\frac{\partial \tau_{yx}}{\partial x}+\frac{\partial \tau_{yy}}{\partial y}+\frac{\partial \tau_{y}}{\partial z} \quad (6)$$

$$\frac{\partial \rho w}{\partial t}+\frac{\partial \rho uw}{\partial x}+\frac{\partial \rho vw}{\partial y}+\frac{\partial \rho ww}{\partial z}=-\frac{\partial P}{\partial z}+\frac{\partial \tau_{zx}}{\partial x}+\frac{\partial \tau_{zy}}{\partial y}+\frac{\partial \tau_{zz}}{\partial z}-\rho g \quad (7)$$

Turbulence model equation

Known two-equation model of k-ε (Standard) are presented for averaged form in depth as follows: (Rastogi and Reddy, 1978).

$$\frac{\partial hk}{\partial t}+\frac{\partial U_j hk}{\partial x_j}=\frac{\partial}{\partial x_j}[(\nu+\frac{\nu_t}{\sigma_k})h\frac{\partial k}{\partial x}]+hP_k+hP_{kv}-h\varepsilon \quad (8)$$

$$\frac{\partial h\varepsilon}{\partial t}+\frac{\partial U_j h\varepsilon}{\partial x_j}=\frac{\partial}{\partial x_j}[(\nu+\frac{\nu_t}{\sigma\varepsilon})h\frac{\partial \varepsilon}{\partial x}]+hc_{1\varepsilon}\frac{\varepsilon}{k}P_k+hP_{\varepsilon v}-hc_{2\varepsilon}\frac{\varepsilon^2}{k}$$

(9) $$\frac{\partial h\varepsilon}{\partial t}+\frac{\partial U_j h\varepsilon}{\partial x_j}=\frac{\partial}{\partial x_j}\left[\left(\nu+\frac{\nu_t}{\sigma_\varepsilon}\right)h\frac{\partial \varepsilon}{\partial x}\right]+hc_{1\varepsilon}\frac{\varepsilon}{k}P_k+hP_{\varepsilon v}-hc_{2\varepsilon}\frac{\varepsilon^2}{k}$$

$$\nu_t=c_\mu\frac{k^2}{\varepsilon},P_k=2\nu_t S_{ij}.S_{ij} \quad (10)$$

$$P_{kv}=c_k\frac{k^2}{\varepsilon},c_k=\frac{1}{c_f^{1/2}},P_{\varepsilon v}=c_\varepsilon\frac{u_f^4}{h^2},c_\varepsilon=\frac{1}{\sqrt{e_*\sigma_t}}\frac{c_{2\varepsilon}c_\mu^{1/2}}{c_f^{3/4}},c_f=\frac{u_f^2}{u^2+v^2+w^2}=\frac{n^2g}{h^{1/3}} \quad (11)$$

$$c_\mu=0.09,c_{\varepsilon1}=1.44,c_{\varepsilon2}=1.92,\sigma_k=1.0,\sigma_\varepsilon=1.31$$

P_{kv} and P_{kv} are production terms as result of non-uniform distribution velocity in depth that is stronger near-bed. P_k is production term of turbulent kinetic energy averaged in depth as result of velocity gradients in the plan. ν_t is the vortex viscosity. Turbulence model is used for calculation of lateral flow into one channel and is achieved much better results in comparison with ν_t for fixed parameters of rotational flow (MCGurik and Rodi, 1978). c_f is the bed friction coefficient. σ_t is Schmidt number that shows relationship between turbulence viscosity and turbulent diffusion coefficient according to the following equation:

$$\varepsilon_d=\frac{\nu_t}{\sigma_t} \quad (12)$$

Amount of σ_t is considered 0.5 (Keller and Rodi, 1988). Although values of σ_t are 0.5 to 2 in variable references (Gibson and launder, 1978). e_* is coefficient that gives turbulence diffusion coefficient in depth by following equation (Keller and Rodi, 1988).

$$\varepsilon_d=e_*hu_f \quad (13)$$

Direct measurement of color broadcasting in the fixed-width channels offers 0.15 for e_*. Although Keller and Rodi achieved better solutions for the velocity and stress within the composite channels (Keller and Rodi, 1988). On the other hand Biglari and Sturm have been assumed e_* equaled to 0.3 to get the better answer within the composite channels (Biglari and Sturm, 1998). MCGurik and Rodi have considered $\frac{1}{\sqrt{e_*\sigma_t}}$

equaled to 3.6 (MCGurik and Rodi, 1978). In ε equation of RNG model includes a correction term $c_{\varepsilon 1}$ that is *constant strain-dependent (Yakhot et al, 1992). For k-ε (RNG), we have:*

$$\frac{\partial h\varepsilon}{\partial t}+\frac{\partial U_j h\varepsilon}{\partial x_j}=\frac{\partial}{\partial x_j}[(\nu+\frac{\nu_t}{\sigma\varepsilon})h\frac{\partial\varepsilon}{\partial x}]+hc^*_{1\varepsilon}\frac{\varepsilon}{k}P_k+hP_{\varepsilon\nu}-hc_{2\varepsilon}\frac{\varepsilon^2}{k} \quad (14)$$

$$c_\mu=0.0845, c^*_{1\varepsilon}=c_{1\varepsilon}-\frac{\eta(1-\frac{\eta}{\eta_0})}{1+\beta\eta^3}, c_{1\varepsilon}=1.68, \sigma_k=1.39, \beta=0.012, c_{1\varepsilon}=1.42,$$

$$\eta=(2E_{ij}.E_{ij})^{1/2}\frac{k}{\varepsilon}, \eta_0=4.377 \quad (15)$$

Only constant β is adjustable, high levels of turbulent data are obtained near-wall. All other constants are calculated explicitly as part of the RNG process.

$$\frac{\partial hk}{\partial t}+\frac{\partial U_j hk}{\partial x_j}=\frac{\partial}{\partial x_j}[(\nu+\frac{\nu_t}{\sigma_k})h\frac{\partial k}{\partial x}]+P_k+P_b-h\varepsilon \quad (16)$$

$$\frac{\partial h\varepsilon}{\partial t}+\frac{\partial U_j h\varepsilon}{\partial x_j}=\frac{\partial}{\partial x_j}[(\nu+\frac{\nu_t}{\sigma\varepsilon})h\frac{\partial\varepsilon}{\partial x}]+hc_{1\varepsilon}\frac{\varepsilon}{k}P_k+hc_1S_\varepsilon-hc_2\frac{\varepsilon^2}{k+\sqrt{\nu\varepsilon}}+S_\varepsilon \quad (17)$$

$$c_1=Max[0.43,\frac{\eta}{\eta+s}], \eta=s\frac{k}{\varepsilon}, s=\sqrt{2s_{ij}s_{ij}}, \mu_t=hc_\mu\frac{k^2}{\varepsilon}, P_k=-\rho\overline{u_i^{'}u_j^{'}}\frac{\partial u_j}{\partial x_i^{'}},$$

$$P_k=\mu_t s^2, P_b=\beta g_i\frac{\mu_t}{\Pr_t}\frac{\partial T}{\partial x_i}, \mu_t=\rho c_\mu\frac{k^2}{\varepsilon}, c_\mu=\frac{1}{A_0+A_s\frac{KU^*}{\varepsilon}}, U^*=\sqrt{s_{ij}s_{ij}+\overline{\Omega_{ij}}\,\overline{\Omega_{ij}}}, \quad (18)$$

$$\overline{\Omega_{ij}}=\Omega_{ij}-\varepsilon_{ijk}\omega_k, A_0=4.04, A_s=\sqrt{6}\cos\Phi, \Phi=\frac{1}{3}\cos^{-1}(\sqrt{6}\omega), \omega=\frac{s_{ij}s_{jk}s_{ki}}{\tilde{s}^3}, \tilde{s}=\sqrt{s_{ij}s_{ij}},$$

$$s_{ij}=\frac{1}{2}(\frac{\partial u_j}{\partial x_i}+\frac{\partial u_i}{\partial x_j}), c_{1\varepsilon}=1.44, c_2=1.9, \sigma_k=1, \sigma_\varepsilon=1.2, \beta=-\frac{1}{\rho}(\frac{\partial P}{\partial T})p, \Pr_t=0.85$$

WillCox, turbulence model k-ω (standard) equation to be provided as follows: (WillCox, 1988):

$$\frac{\partial k}{\partial t}+U_j\frac{\partial k}{\partial x_j}=\tau_{ij}\frac{\partial U_i}{\partial x_j}-\beta^*k\omega+\frac{\partial}{\partial x_j}[(\nu+\sigma^*\nu_T)\frac{\partial k}{\partial x_j}] \quad (19)$$

$$\frac{\partial\omega}{\partial t}+U_j\frac{\partial\omega}{\partial x_j}=\alpha\frac{\omega}{k}\tau_{ij}\frac{\partial U_i}{\partial x_j}-\beta\omega^2k\omega+\frac{\partial}{\partial x_j}[(\nu+\sigma\nu_T)\frac{\partial\omega}{\partial x_j}] \quad (20)$$

$$\frac{\partial k}{\partial t}+U_j\frac{\partial k}{\partial x_j}=\tau_{ij}\frac{\partial U_i}{\partial x_j}-\beta^*k\omega+\frac{\partial}{\partial x_j}[(\nu+\sigma^*\nu_T)\frac{\partial k}{\partial x_j}] \; \nu_t=\frac{k}{\omega}, \alpha=\frac{5}{9}, \beta=\frac{3}{40}, \beta^*=\frac{9}{100}, \sigma=\frac{1}{2}, \varepsilon=\beta^*\omega k$$

3. Result and discussions

The values of the physical properties of water are considered as a default respectively, for density, viscosity, heat capacity and thermal conductivity. Solutions of all governing equations are subject to assignment of variables correctly in the boundary nodes. In steady state problems required only boundary condition but in unsteady state problems is required the initial conditions for all nodes in the network. Common boundary conditions in hydraulic issues include (Soltani and Rahimi Asl, 2003):

A- Inlet boundary condition: numerical models can fit the model by means of the various boundary conditions such as velocity, mass flow, etc. For example, in modeling of flow inside a closed or open channel can be used velocity inlet as input boundary condition.

B- The outlet boundary condition is considered pressure outlet equals the atmospheric pressure. If the output is chosen at a far distance from geometric constraints, and no change in direction of flow then the flow state is developed full. Using this model is caused the output surface is perpendicular to the flow and gradient is zero in the perpendicular direction on the output surface (Soltani and Rahimi Asl, 2003).

C - Wall boundary condition: the wall boundary condition is used to limit the area of between fluid and solid. The model is ready for simulation by Solutions set and defining the model. The following steps show the simulation process (Versteeg and Malalasekera, 2007): selection methods of discretization equation: In this paper first order upstream difference method is used for discretization of momentum, k, ε and ω equations and the standard method is used to find the pressure. Selection methods of the relation velocity - Pressure: this step is only be studied segregated. In this paper is used from SIMPLE method for velocity - pressure coupling. Determine the discount factors: the discount factor values are used for control of calculated variables in the each iteration. In this paper, the default values are used respectively for the pressure, density, momentum, k, ε and turbulent viscosity. In this paper, the initial values of the relative pressure is considered zero And the initial values of velocity components close to the average values presented in the input stream. By completing the steps in the numerical model, we can start the introduced process of problem by defining of repeat process. The frequency of reporting of results can be introduced before computing the numerical model. During solution process can be seen convergence of solution by the control of residues, integral of surface, statistics and values of the force. After finishing solution the computation of the unknown quantities and the results can be calculated at any point of the field and can be displayed by vector in the form, contour and profile views (Versteeg and Malalasekera, 2007). In this paper for solution of flow is usually introduced initial number repeat 1000 with report of every step of the calculation that conditions for convergence of the unknown parameters were satisfied after 300 to 350 iterations.

5. Discussion

In this research, Gambit software version 16.3.2 has been used to generate the geometry and mesh it. The mesh pattern is Quad element and map type is used for the surfaces. The existing boundary conditions are velocity input from the left side from the top of the arc and pressure output boundary condition at the bottom of the arc outlet. The simulation results are seen in Figures 5 to 21.

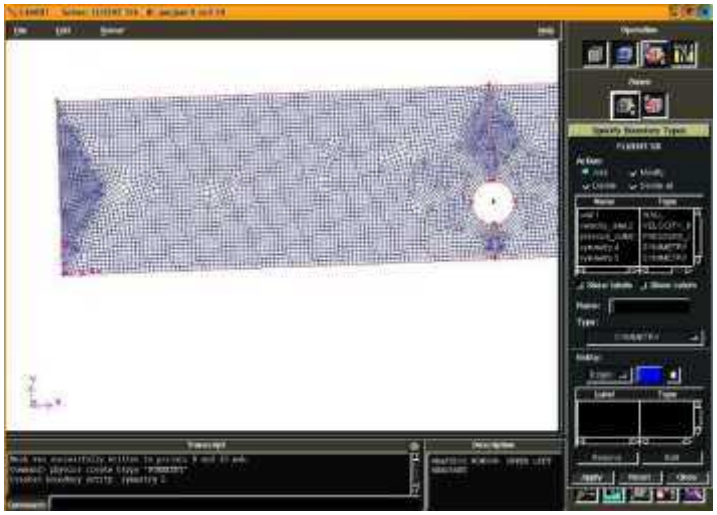

Figure 5 - Model geometry in Gambit software

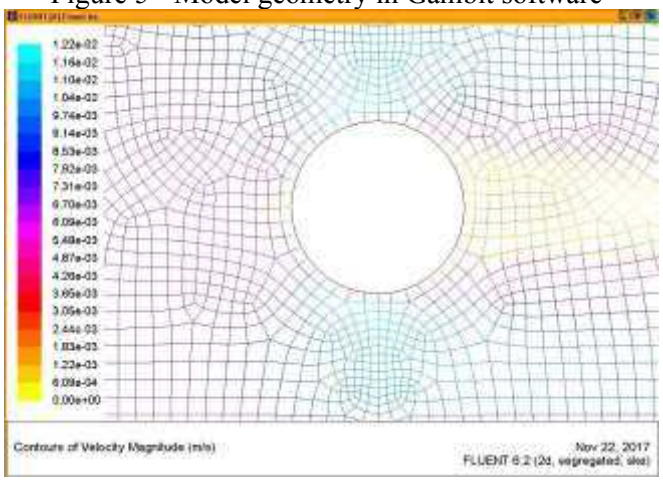

Figure 6 - The velocity curve, m/s, shows that the velocity values decrease behind the offshore platform base. The maximum velocity value is below the offshore platform base line, which will cause scour.

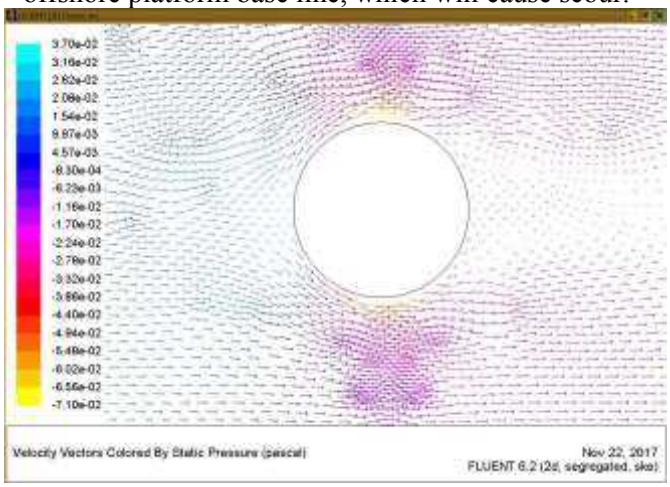

Figure 7 - The iso pressure in Pascals show that the pressure values decrease behind the offshore platform base and above and below it. The maximum negative pressure is below the offshore platform base line, which will cause scour.

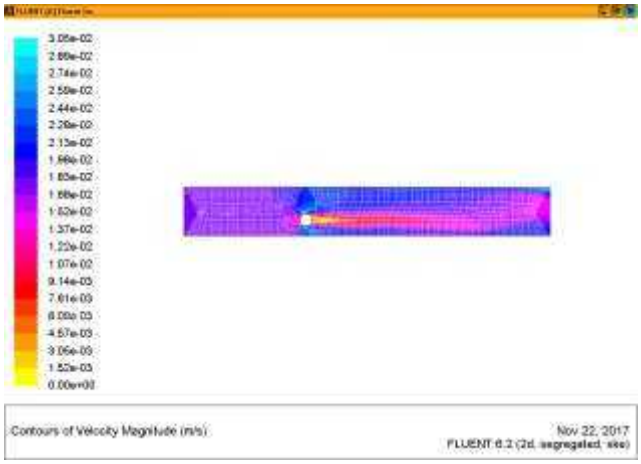

Figure 8- Lines of constant velocity, m/s, results show that the velocity values decrease behind the offshore platform base. The maximum velocity value is below the offshore platform base line, which will cause scour.

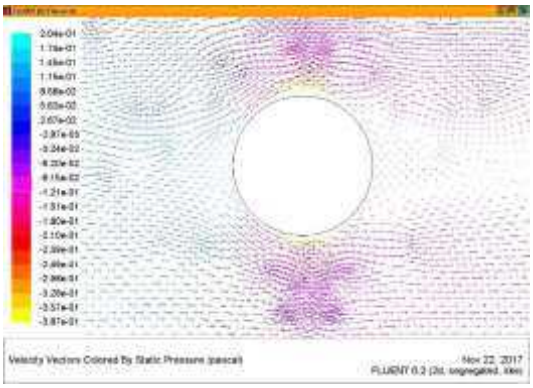

Figure 9- Iso pressure lines in Pascal, the results show that the pressure values behind the offshore platform base and above and below it decrease. The maximum negative pressure value is below the offshore platform base line, which will cause scouring. By increasing the Reynolds number from 3000 to 7000, the negative pressure value in this case increases.

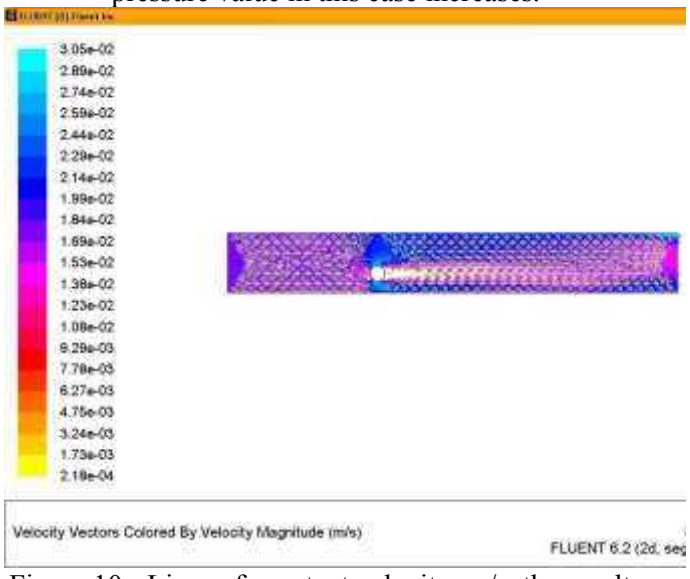

Figure 10 - Lines of constant velocity, m/s, the results show that the velocity values decrease behind the offshore platform base. The maximum velocity value is below the offshore platform base line, which will cause scour. By increasing the Reynolds number from 3000 to 7000, the maximum velocity value in this case increases.

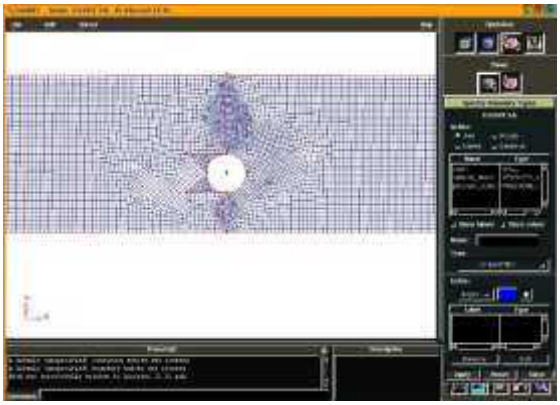

Figure 11 - Meshing and geometry of the model created for the impact of barrier plates in front of the offshore platform base.

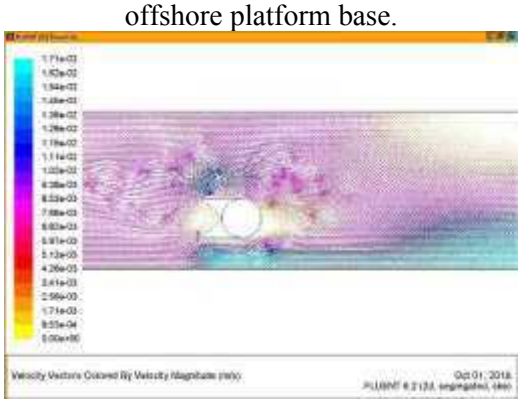

Figure 12 - Lines of constant velocity, m/s, results show that the velocity values decrease behind the offshore platform base. The maximum velocity value is below the offshore platform base line, which will cause scouring at a distance further from the base due to the presence of barrier plates.

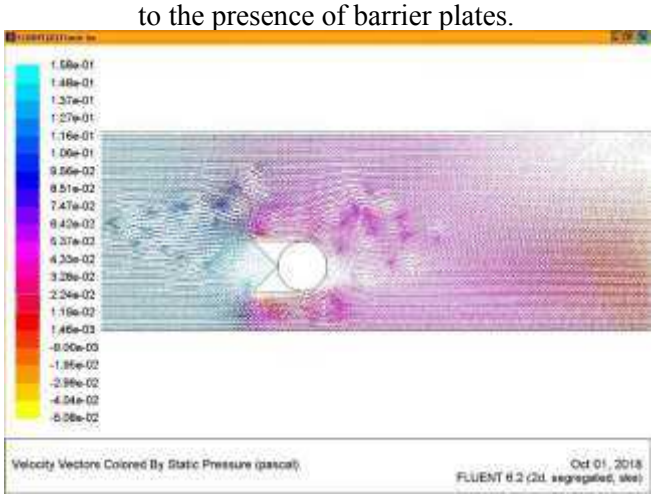

Figure 13- Isobaric lines in Pascal, the results show that the pressure values behind the offshore platform base and above and below it decrease. The maximum negative pressure value is below the offshore platform base line, which is significantly reduced compared to the case without the use of barrier plates.

4. Conclusion

The reduction of the pressure gradient is one of the most important and fundamental factors in the formation and development of scour around the base of an offshore platform and the formation of the sluice phenomenon in the bed around the base of the offshore platform. This phenomenon is considered as one of the results of the pressure gradient prevailing over the submerged weight of bed sediment particles.

In the present study, the effect of the offshore platform base lines with their different diameters on the scour process is first investigated; then, by installing an impermeable sheet in front of the offshore platform base lines, the effect of this sheet on the scour phenomenon is studied.

Laboratory results indicate that the use of impermeable sheets in front of the offshore platform base lines to some extent prevents the formation of scour tunnels around the offshore platform base lines and protects them from the dangers caused by scour.

In this study, the simulation of the flow around the submerged offshore platform base with different Reynolds number states was investigated using the computational fluid dynamics method and Fluent software.

The results of the first model for the isovelocity lines, m/s, show that the velocity values behind the offshore platform base decrease from 0.006 to 0.00006.

The maximum velocity value is below the offshore platform base line, which will cause scouring. By increasing the Reynolds number from 3000 to 7000, the maximum velocity value increases in this case.

The results of the isopressure lines in Pascals show that the pressure values behind the offshore platform base and above and below it decrease. The maximum negative pressure value is below the offshore platform base line, which will cause scouring. By increasing the Reynolds number from 3000 to 7000, the negative pressure value in this case increases from minus 0.07 to minus 0.3 in Pascals, which will cause scouring. The maximum negative pressure value is below the offshore platform base line, which is significantly reduced compared to the case without the use of barrier plates.

5. References

1. Sorenson Robert M. - 1938 - Principles of Marine Engineering - Khosrow Bargi - Tehran University Publications Institute.
2. [1]Fredsoe, J., E. A. Hansen, Ye Mao, and B. M. Sumer. "Three-dimensional scour below pipelines." Journal of Offshore Mechanics and Arctic Engineering110, no. 4 . 373-379, 1988.
3. Chiew, Yee-Meng. "Mechanics of local scour around submarine pipelines."Journal of Hydraulic Engineering 116, no. 4. 515-529, 1990. [3] Sumer, B. Mutlu, and Jørgen Fredsøe. "Scour around pipelines in combined waves and current ". No. CONF-9606279--. American Society of Mechanical Engineers, New York, NY (United States), 1996.
4. Yang, Bing, Fu-Ping Gao, Dong-Sheng Jeng, and Ying-Xiang Wu. "Experimental study of vortexinduced vibrations of a pipeline near an erodible sandy seabed." Ocean engineering 35, no. 3.301-309, 2008.
5. Gao, Fu-Ping, Bing Yang, Ying-Xiang Wu, and Shu-Ming Yan. "Steady current induced seabed scour around a vibrating pipeline." Applied Ocean Research 28, no. 5.291-298, 2006.
6. Zhao, Ming, and Liang Cheng. "Numerical investigation of local scour below a vibrating pipeline under steady currents." Coastal Engineering 57, no. 4 .397-406, 2010.
7. Zhou, Chunyan, Guangxue Li, Ping Dong, Jinghao Shi, and Jishang Xu. "An experimental study of seabed responses around a marine pipeline under wave and current conditions." Ocean Engineering 38, no. 1 .226-234, 2011.
8. Yang, Lipeng, Bing Shi, Yakun Guo, Lixiang Zhang, Jisheng Zhang, and Yan Han. "Scour protection of submarine pipelines using rubber plates underneath the pipes." Ocean Engineering 84 .176-182, 2014.
9. Yang, Lipeng, Bing Shi, Yakun Guo, and Xianyun Wen. "Calculation and experiment on scour depth for submarine pipeline with a spoiler." Ocean Engineering 55 .191-198, 2012.
10. Sumer, B. M., and J. Fredsoe. "Onset of scour below a pipeline exposed to waves." In The First International Offshore and Polar Engineering Conference. International Society of Offshore and Polar Engineers, 1991.
11. Li, Fangjun, and Liang Cheng. "Prediction of lee-wake scouring of pipelines in currents." Journal of waterway, port, coastal, and ocean engineering (2001).
12. Sumer, B. Mutlu, Christoffer Truelsen, T. Sichmann, and Jørgen Fredsøe. "Onset of scour below pipelines and self-burial." Coastal engineering 42, no. 4 .313-335, 2001.
13. *Reynolds, O., 1984. On the dynamical theory of incompressible viscous fluids and the determination of the criterion. Phil. Trans. Roy. Soc. London, 123-161.*
14. *McGurik, J.J. and Rodi, W., 1978. A depth-averaged mathematical model for the near fluid of side discharge into open- channel flow. Journal of Fluid Mechanics, 864, 761-781.*
15. *Keller, R.J. and Rodi, W., 1988. Prediction of flow characteristics in main channel/floodplain flows. Journal of Hydraulic Research, IAHR, 26(4), 425- 441.*

16. *Biglari, B. and Sturm, T.W., 1998. Numerical modeling of flow around bridge abutments in compound channel. Journal of Hydraulic Engineering, ASCE, 124(2), 156-163.*
17. *Gibson, M.M. and Launder, B.E., 1978. Ground effects on pressure fluctuations in the atmospheric boundary layers. Journal of Fluid Mechanics, 86, 491-511.*
18. *Rastogi A. K. and Rodi, W., 1978. Prediction of heat and mass transfer in open channels. Journal of Hydraulics Division, ASCE, 104(3), 397- 420.*
19. *Yakhot V., Orszag S.A., Thangam, S., Gatski, T.B. and speziale, C.G., 1992. Development of turbulence models for shear flows by a double expansion technique. Physics of Fluids A, Vol. 4, No. 7, pp1510-1520.*
20. *Wilcox D.C., 1988. Re-assessment of the scale-determining equation for advanced turbulence models. AIAA Journal, vol. 26, pp. 1414- 1421.*
21. *Versteeg, H.K. and Malalasekera, W., 2007. An Introduction to Computational Fluid Dynamics: The Finite Volume Method, Prentice Hall, Feb 16, 503 pages.*
22. *Soltani, M.V. and Rahimi Asl, R., 2003. Computational fluid dynamics by Fluent software, Tehran, Tarrah issues.*

INTERNATIONAL JOURNAL OF
COASTAL, OFFSHORE & ENVIRONMENTAL ENGINEERING IJCOE Vol.10/No. 4/ Autumn 2025 (45-54)

Available online at: www. Ijcoe.org

Field Investigation of Water Mass Stratification and Variability in the Strait of Hormuz

Samad Hamzei*[1], Amirmahdi Zarboo[1], Emad Koochaknejad[1]

[1] *Iranian National Institute for Oceanography and Atmospheric Sciences (INIOAS), Tehran, 1411813389, Iran*
sh_hamzei@yahoo.com , amirmahdizarboo@gmail.com, emad.koochaknejad@inio.ac.ir

ARTICLE INFO

Article History:
Received: 16 Sep 2025
Accepted: 18 Feb 2026

Keywords:
Persian Gulf water mass
Indian Ocean water mass
Seasonal thermocline
Water stratification
Strait of Hormuz

ABSTRACT

The Persian Gulf is a shallow basin characterized by high evaporation rates, resulting in the formation of one of the saltiest water bodies in the world. To compensate for the evaporative water loss, a less saline water mass enters the Gulf through the Strait of Hormuz, known as the Indian Ocean Surface Water (IOSW). Due to its high density, the hypersaline Persian Gulf Water (PGW) sinks toward the seabed and exits the Gulf through the deeper layers of the Strait of Hormuz, flowing toward the Gulf of Oman. To identify and characterize the water masses present in the Persian Gulf, Strait of Hormuz, and Gulf of Oman, hydrographic surveys were conducted during the summer and winter seasons of the 2102 and 2201 expeditions aboard the Persian Gulf Explorer. Using CTD profiling, physical and chemical parameters of seawater were measured. Analysis of temperature, salinity, and potential density anomaly across isopycnal layers—surface, intermediate, and deep—along north-south and east-west vertical transects enabled the evaluation of water mass structure and distribution in the region. Results indicate that during summer, surface water mixing is intense due to atmospheric conditions such as the monsoon, and stratification primarily occurs below depths of 30 meters. In contrast, winter stratification weakens, and due to lower temperatures, horizontal layering is observed from the eastern Strait of Hormuz to the western end of the Persian Gulf—marked by increasing salinity and density, and decreasing temperature. The IOSW enters the Persian Gulf through the Strait of Hormuz and propagates along the northern coastline. In summer, cyclonic eddies in the Gulf induce southward flow in several central regions. The PGW is observed in the deep central Gulf during summer, while surface mixing between IOSW and Gulf waters reduces salinity in the upper layers. The summer PGW mass is detectable in the western Gulf of Oman at approximately 100 meters depth near the Strait of Hormuz. However, in winter, the inflow into the Gulf weakens due to reduced wind forcing and strong horizontal stratification of salinity and density, which limits the penetration of incoming water.

1. Introduction

The Persian Gulf is considered the third largest gulf in the world, following the Gulf of Mexico and Hudson Bay. The Strait of Hormuz is one of the most strategic maritime corridors globally, serving as the primary gateway for oil exports and a major route for non-oil trade between Southeast Asia and the Middle East. Together, the Persian Gulf and the Gulf of Oman form a vital geopolitical and commercial zone for Iran, encompassing diverse marine ecosystems and substantial oil and gas reserves (Raeisi et al., 2020).

The Persian Gulf is a shallow, semi-enclosed basin with an average depth of 35 meters and a maximum depth of 90 meters, connected to the Gulf of Oman via the Strait of Hormuz. It is recognized as one of the principal sources of hypersaline water masses in the global ocean. The Gulf of Oman, located in the northwestern part of the Indian Ocean near the Arabian Sea, has an L-shaped configuration. The Strait of

Hormuz lies approximately at 26°30′N and 56°30′E, with a width of 56 km and depths ranging from 90 to 110 meters. The regional meteorology is dominated by northwesterly winds with seasonal variability, which also influence the Gulf of Oman. Sea surface temperatures in the Strait of Hormuz range from 32–34°C in summer and 18–20°C in winter. Due to high evaporation rates exceeding freshwater input from precipitation and river discharge, the Persian Gulf functions as a reverse estuary (Reynolds, 1993).

Geographically, the Persian Gulf extends in a northwest–southeast direction between 25°–30°N and 48°–56°E, while the Gulf of Oman spans 26°–32°N and 56°–62°E. Although the maximum depth of the Persian Gulf is 90 meters, depths exceeding 100 meters are observed in the Strait of Hormuz. Pous et al. (2004) conducted hydrographic measurements in the eastern Strait of Hormuz during October and early November 1999, analyzing physical water properties, current profiles, sea level fluctuations, and surface circulation. Their findings indicated that inflow to the Persian Gulf occurs through the northern sector of the strait, while dense Persian Gulf Water (PGW) exits through the southern deep layers.

In more recent studies, Azizpour et al. (2016) deployed four subsurface mooring systems during field campaigns in November 2012 and January 2013, identifying tidal dynamics in the Strait of Hormuz as a combination of semi-diurnal and diurnal standing wave patterns. Hunter (1982), using data from a UK meteorological vessel in 1981, observed a surface inflow of approximately 0.1 m/s along the Iranian coast. Seasonal analysis revealed stronger inflow during summer (~0.2 m/s) and weaker currents in autumn and winter. These estimates were supported by ship drift observations along the Iranian coastline.

Sonu (1979), based on April 1977 measurements, documented an inflow penetrating up to 200 km into the Persian Gulf via the Strait of Hormuz. The density contrast between the Persian Gulf and the Gulf of Oman, intensified by the summer monsoon, drives water exchange, as previously noted by Schott (1918), Barlow (1932), and others. The outflow of PGW into the Gulf of Oman has been reported by Sewell (1934), Emery (1956), Duing & Koske (1967), and more recently by Ramak (2022).

Sugden (1963) proposed a surface inflow above the outflow layer, accompanied by cyclonic circulation within the Persian Gulf. Pous et al. (2004) confirmed that PGW exits through the southern deep layers of the strait, while IOSW enters through the northern sector. Their 1999 GOGP99 cruise data revealed that PGW outflow follows a southeastward trajectory below 200 meters in the Gulf of Oman, later deflecting southwestward near the continental slope and continuing along the Omani coast at ~0.2 m/s. Temperature and salinity of PGW decrease from 27°C and 39.75 psu in the Gulf to 21°C and 37.1 psu in the northern Arabian Sea, with non-uniform mixing in localized regions.

Five major water masses were identified:

- Seasonal Thermocline Water (TW): ~30°C, 37 psu at ~25 m depth (summer)
- Indian Ocean Surface Water (IOSW): 20–22°C, 36–36.5 psu at 50–100 m
- Persian Gulf Water (PGW): 20–22°C, 37.25–37.5 psu at 150–300 m
- Red Sea Water (RSW): 10–12°C, 35.5 psu at ~800 m
- North Indian Deep Water (NIDW): ~2°C, 34.8 psu at 2000–4000 m

Hunter (1982) attributed PGW formation to intense evaporation in the northwest Gulf, with PGW descending and moving southward under the influence of Coriolis deflection. He noted that sea level reduction due to evaporation and limited rainfall is compensated by inflow along the Iranian coast from the Gulf of Oman.

2. Methodology

To investigate the spatial distribution and interaction of water masses in the Strait of Hormuz, data from two hydrographic cruises conducted in 2021 (1400 SH) were analyzed.

The summer cruise, titled “Oceanographic Monitoring of the Persian Gulf and Gulf of Oman,” was conducted by the Iranian National Institute for Oceanography and Atmospheric Science aboard the Persian Gulf Explorer during September–October 2021 (PGE2102). Measurements were taken at 67 stations from the Arvand River mouth (Sept 7) to Chabahar (Oct 1).

The winter cruise, also titled “Oceanographic Monitoring of the Persian Gulf and Gulf of Oman,” was conducted in two legs during January–February 2022 (PGE2201). A total of 86 stations were sampled from the northernmost point of the Persian Gulf (Jan 12) to near Chabahar (Feb 12), under varying atmospheric and oceanic conditions.

Table 1. Specifications of CTD Measurements Conducted During Research Cruises

Cruise Code	Survey Area	Number of Stations	Measurement Period
PGE2102	Persian Gulf, Strait of Hormuz, Gulf of Oman	67	September 7 to October 1, 2021
PGE2201	Persian Gulf, Strait of Hormuz, Gulf of Oman	86	January 12 to February 12, 2022

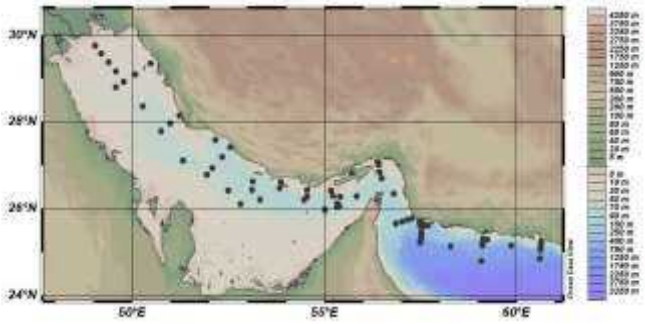

Figure 1. Locations of Sampling Stations During summer and winter Cruises

Through the analysis of temperature, salinity, and density fields, the distinct characteristics and boundaries of various water masses were identified. By plotting isotherms, isohalines, and isopycnals across different depth layers, the spatial extent and presence of water masses were delineated using contour mapping. For this purpose, a depth of 5 meters was selected to represent the surface layer, and 50 meters for the deep layer of the Persian Gulf.

Using vertical profiles of temperature, salinity, and density, the location, intrusion extent, and lens-like structure of water masses were determined. These profiles were extracted along east–west transects across the central Strait of Hormuz and north–south transects across the western, central, and eastern sectors of the strait.

3. Results and Discussion

Water masses are generally classified into deep and bottom waters, intermediate waters, and surface waters. Their nomenclature and spatial boundaries vary depending on the oceanic basin in which they form. To identify and trace water masses, researchers rely on tracers, their position relative to the global ocean, and their vertical distribution (Emery and Meincke, 1986).

This section focuses on the identification and tracking of water masses, as well as the analysis of horizontal and vertical mixing and stratification in the Persian Gulf and Gulf of Oman during warm and cold seasons, based on CTD measurement data.

3.1. Salinity Fields

Figure 2 illustrates isohaline distributions at depths of 5 meters and 50 meters from the PGE2102 (summer) and PGE2201 (winter) research cruises. In summer, the highest salinity values are observed along the southern Arabian coastline and the northwestern sector of the Persian Gulf. Lower salinity values appear in the central Gulf and along the northern coast of the Strait of Hormuz. In the Gulf of Oman, surface salinity is generally below 37 psu, while salinity in the Strait of Hormuz approaches 38 psu, and in the Persian Gulf ranges from 39 to 40 psu.

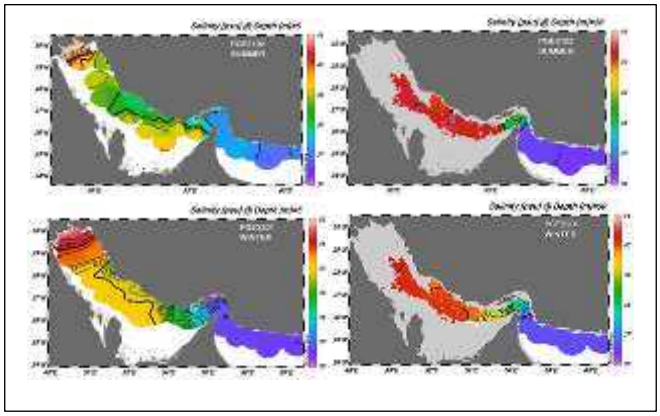

Figure 2. Isohaline surfaces in the Persian Gulf and the Gulf of Oman at depths of 5 and 50 meters during cruise PGE2102 in summer and cruise PGE2201 in winter

At 50 meters depth during summer, most areas of the Persian Gulf with depths exceeding 50 meters exhibit salinity values above 40 psu, with two distinct high-salinity cores located in the northern and central Gulf. A pronounced salinity gradient is evident in the western Strait of Hormuz, where salinity increases from 37.5 psu in the east to over 40 psu in the west. This depth reveals the interaction between the inflowing IOSW and the outflowing PGW, with a sharp salinity contrast clearly delineating the two water masses.

In winter, surface salinity data from PGE2201 show the highest values in the northwestern extremity of the Persian Gulf. Lower salinity is observed in the central and southern Gulf. In the Gulf of Oman, surface salinity drops below 36.8 psu, and in the northern Strait of Hormuz, it falls below 36 psu, attributed to heavy rainfall in January 2022, which introduced significant freshwater into the region.

At 50 meters depth, near-bottom waters in the Persian Gulf maintain salinity levels above 40 psu, but salinity decreases toward the Strait of Hormuz. In the Gulf of Oman, a more uniform salinity field is observed, with a clear east–west salinity gradient extending across the Strait of Hormuz.

3.2. Temperature Fields

Figure 3 presents isotherm distributions from cruises PGE2102 and PGE2201. Surface temperatures during the summer cruise (September–October 2021) exceed 35.5°C in the Persian Gulf, making it warmer than adjacent oceanic waters. In two northern zones near the Iranian coastline, temperatures reach up to 35°C. In the Strait of Hormuz, surface temperatures are more moderate, while in the Gulf of Oman, they drop below 31°C.

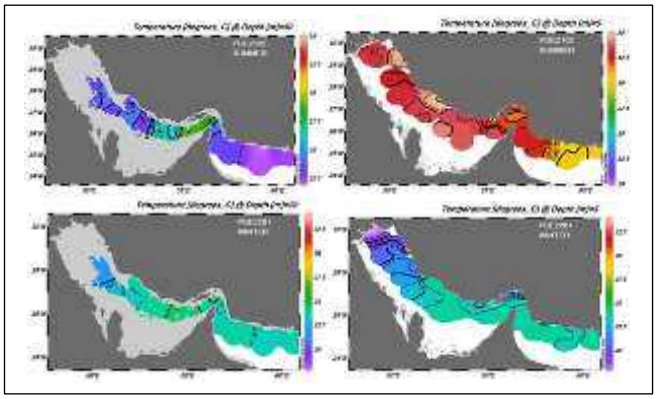

Figure 3. Isothermal surfaces in the Persian Gulf and the Gulf of Oman at depths of 5 and 50 meters during cruise PGE2102 in summer and cruise PGE2201 in winter

At 50 meters depth in summer, a noticeable temperature decline is observed in both the Persian Gulf and Gulf of Oman, whereas the Strait of Hormuz retains relatively higher temperatures. Temperatures fall below 25°C in the Persian Gulf and below 24°C in the Gulf of Oman, while the Strait of Hormuz shows values above 27°C. This pattern suggests enhanced vertical mixing in the Strait of Hormuz compared to the Persian Gulf and Gulf of Oman, resulting in a weaker summer thermocline in the strait.

Winter temperature variations across different depths reveal that at 5 meters, surface temperatures decrease from the central Gulf toward the northwestern end. From the central Gulf to the midsection of the Strait of Hormuz, temperatures remain relatively uniform, but in the northern coastal areas of the strait, temperatures drop to 20°C. The Gulf of Oman exhibits relatively homogeneous temperatures throughout. The strongest horizontal temperature gradients are found in the northwestern Persian Gulf and northern Strait of Hormuz.

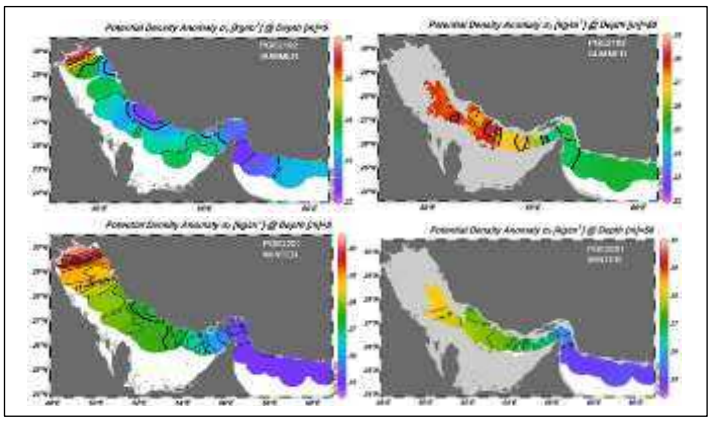

Figure 4. Isopycnal surfaces in the Persian Gulf and the Gulf of Oman at depths of 5 and 50 meters during cruise PGE2102 in summer and cruise PGE2201 in winter

At 50 meters depth in winter, temperatures vary slightly. Lower temperatures are observed in the central and northwestern Gulf, while warmer zones exceeding 24°C appear in the western and central Gulf, indicating the presence of a distinct water mass—likely the dense Persian Gulf Water (PGW)—characterized by its unique thermal signature.

3.3. Potential Density Anomaly (σ_0)

During the summer season, the highest values of potential density anomaly (σ_0) at the surface are observed in the northwestern Persian Gulf. Following this region, the southern sectors of the Gulf exhibit elevated density values, while the Strait of Hormuz and the central axis of the Gulf, near the Hormozgan–Bushehr boundary, show the lowest surface densities. Since seawater density is a function of both temperature and salinity, areas with higher salinity and lower temperature tend to exhibit greater potential density.

The lowest summer density values are recorded in the eastern Strait of Hormuz, but density increases again toward the Gulf of Oman and the Persian Gulf. This increase is attributed to higher salinity in the Gulf and lower surface temperatures in the Gulf of Oman compared to the Strait of Hormuz.

In winter, potential density anomaly at 5 meters depth shows maximum values in the northwestern Persian Gulf, reaching up to 30 kg/m³. From the Gulf toward the Strait of Hormuz, density decreases, stabilizing around 25.5 kg/m³ in the eastern Strait and adjacent Gulf of Oman. The strongest density gradients are observed in the western Strait of Hormuz and the northwestern Gulf.

At 50 meters depth, density anomaly in the Persian Gulf is generally higher than in the Strait of Hormuz and Gulf of Oman. However, due to the presence of warmer PGW in deeper layers, the density anomaly is not excessively high. In the Gulf of Oman, density values remain relatively uniform, but increase slightly toward the Strait of Hormuz.

3.4. Vertical Profiles

Figure 5 presents vertical sections T1, T2, and T3 across the western, central, and eastern Strait of Hormuz, and section L1 spanning west to east across the Persian Gulf, constructed to identify water masses and their interactions during summer and winter.

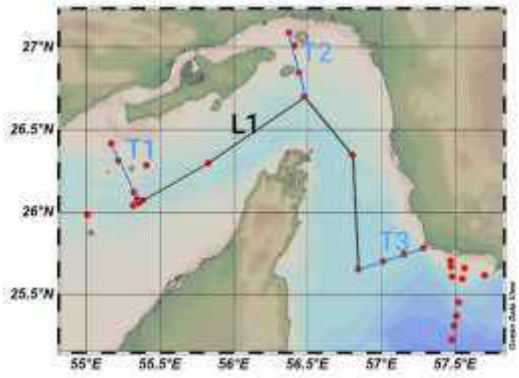

Figure 5. The plotted profiles T1, T2, and T3 illustrate conditions in the western, central, and eastern parts of the Strait of Hormuz, while profile L1 represents a transect from the western to the eastern Strait of Hormuz

Figure 6 shows vertical profiles from the Iranian coast to the central Persian Gulf in both seasons. The winter salinity profile reveals lower surface salinity near the Iranian coast and higher salinity in deeper layers near the central and southern Arabian coasts.

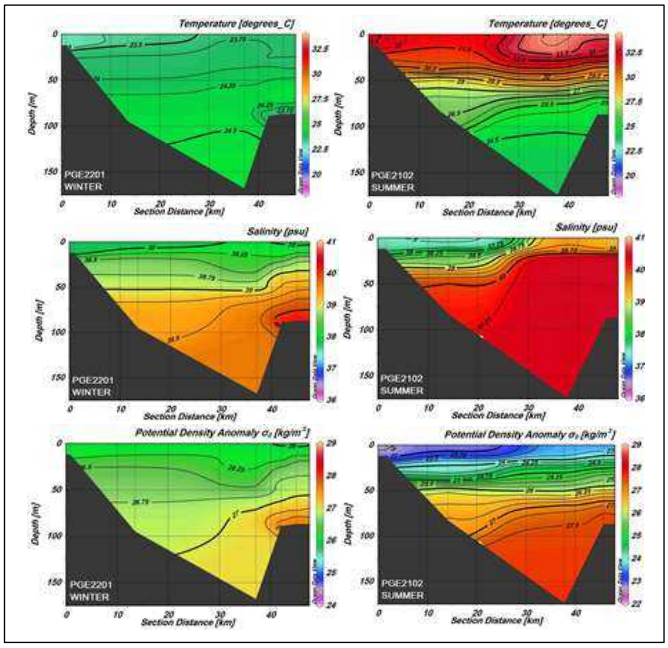

Figure 6. Plotted profiles of salinity, temperature, and potential density anomaly along transect T1 in the western part of the Strait of Hormuz

In summer, low-salinity waters from the northeastern Gulf extend toward the central basin, indicating the inflow of IOSW. Salinity increases from north to south, and also with depth in the eastern Gulf, suggesting the formation of a high-salinity bottom water mass, particularly in the southern Gulf.

The summer temperature profile shows a well-mixed surface layer down to ~20 meters due to turbulence and interaction. The thermocline develops between 30 and 50 meters, marking the transition to cooler, denser waters.

The potential density anomaly profile in summer indicates a progressive increase with depth, with the highest values in the southeastern deep Gulf, confirming the presence of a dense bottom water mass.

The winter profiles in Figure 6, from northeast to southeast, show a gradual salinity increase from surface to bottom in the northeast, rising from 38 psu to over 39 psu near the seabed. Moving from the northwestern Strait of Hormuz to the central Gulf, surface salinity increases slightly to 38.5 psu.

In the central Gulf stations, salinity variation with depth is minimal, remaining just above 40 psu. Near the Iranian coast, a two-layer structure is evident: fresher surface waters overlying saltier bottom waters.

Thermally, lower temperatures are recorded near the Iranian coast, with warmer waters in the central Gulf. Toward the southern coast, temperatures decrease slightly. Temperature inversion is observed in northern stations, where surface waters are cooler than deeper layers, forming a two-layer thermal structure. In the central Gulf, a warm water lens with temperatures near 24°C extends from surface to near-bottom.

Potential density anomaly profiles show a consistent increase from surface to bottom, with a slight rise in density from northern to central stations in the Strait of Hormuz.

Figure 7 illustrates vertical profiles of salinity, temperature, and potential density anomaly from north to central Strait of Hormuz. In summer, the northern strait exhibits homogeneous water properties, with surface salinity decreasing toward the center, likely due to the presence of a fresher water mass extending to ~30 meters depth.

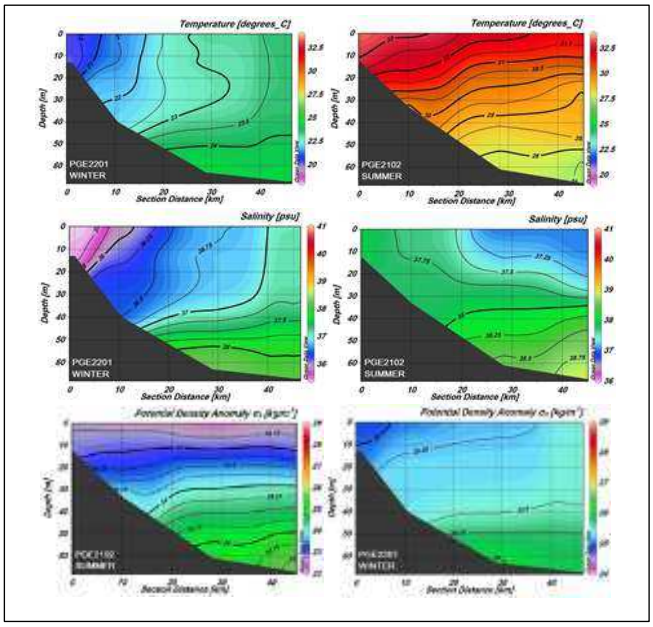

Figure 7. Plotted profiles of salinity, temperature, and potential density anomaly along transect T2 from north to south in the central part of the Strait of Hormuz

In the central strait, salinity increases with depth, forming a strong halocline between 30 and 60 meters. The presence of high-salinity bottom waters indicates the outflow of PGW through the southern and mid-depth layers of the strait.

The temperature section shows higher surface temperatures in the northern strait compared to the center, due to shallower depths and seasonal heating. Surface temperatures decrease toward the center, with the lowest values near the seabed.

Potential density anomaly in the northern strait remains relatively uniform, while in the central strait, density increases with depth.

The bottom panel of Figure 7 shows north–south vertical profiles across central Strait of Hormuz during winter. Northern stations exhibit very low salinity (~35.4 psu), increasing toward the center. This is attributed to rainfall prior to sampling, introducing freshwater into the northern strait.

In central stations, bottom salinity exceeds 38 psu, while surface layers remain below 37 psu, indicating a two-layer structure. In contrast, the northern strait displays a single-layer structure of locally fresh water. The strongest winter halocline is observed between 40 and 60 meters depth.

3.5. Vertical Profiles and Water Mass Structure

Winter temperature measurements in the vertical profile reveal a pronounced thermal inversion in the Strait of Hormuz, where surface waters are colder than deeper layers. A distinct warm water zone is observed below 50 meters near the seabed. A clear horizontal temperature gradient is evident from northern stations toward the central strait. The thermocline in the northern Strait of Hormuz appears inverted, while in the central stations, a uniform temperature layer extends to 50 meters, followed by a slight increase in temperature with depth.

The potential density anomaly (σ_0) profile shows lower density values in the northern stations and higher densities near the bottom in the central Strait of Hormuz. A weak pycnocline is observed between 40 and 60 meters in the central stations. Large portions of this profile are occupied by homogeneous water masses, with density values ranging from 25.2 to 25.4 kg/m³, indicating the presence of uniform water in the mid-strait region.

Figure 8 presents vertical profiles of salinity, temperature, and potential density anomaly from the coastal zone to the central Gulf of Oman. The salinity profile shows higher surface salinity compared to subsurface layers below 25 meters. Between 25 and 80 meters, a low-salinity zone is evident. As the profile extends from the Iranian coast toward the southern and Arabian coasts, salinity increases near the seabed. The compression of isohalines at the terminal station near the bottom indicates the presence of hypersaline PGW, with salinity approaching 40 psu. Above this layer, a low-salinity lens between 40 and 70 meters suggests the intrusion of Indian Ocean Surface Water (IOSW) into the Gulf of Oman.

Temperature variations in this profile are most pronounced between 15 and 40 meters, where a strong vertical gradient and seasonal thermocline are formed. Near the seabed in the central Gulf of Oman, a temperature increase is observed, attributed to the warmer PGW, which contrasts with surrounding waters.

Regarding potential density anomaly, the upper layers exhibit homogeneous density, while between 20 and 40 meters, density increases. The highest density values are found near the bottom in the central Gulf of Oman, where PGW is present.

The lower panel of Figure 8 shows a winter vertical profile across the eastern Strait of Hormuz, from the Iranian coast to the central strait. Salinity remains uniform and below 36.8 psu from the surface to 60 meters. Toward the Iranian coast, salinity remains stable. However, in stations closer to the Arabian coast, salinity increases sharply below 70 meters, reaching over 39.5 psu within the PGW lens.

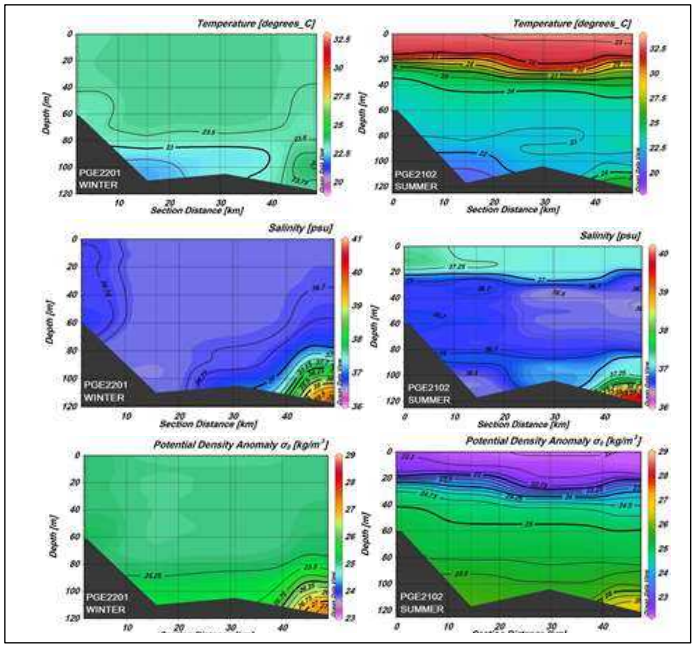

Figure 8. Plotted profiles of salinity, temperature, and potential density anomaly along transect T3 in the eastern part of the Strait of Hormuz

The compression of isohalines and presence of a halocline between 80 and 110 meters are clearly visible in the terminal stations of this transect. Temperature profiles in the eastern Strait of Hormuz show stable values (~23.5°C) in both surface and deep layers up to 70 meters. On the Iranian side, temperatures drop to 22.5°C below 80 meters, while on the Arabian side, temperatures increase with depth, forming a thermal lens (~24°C) at 100 meters—likely associated with PGW intrusion.

The potential density anomaly profile in the eastern Strait of Hormuz reveals a homogeneous layer from surface to 80 meters with density near 25 kg/m³. Below 80 meters, density increases, and in the terminal stations, a sharp rise is observed near the seabed, exceeding 27 kg/m³. This confirms the presence of PGW, characterized by elevated salinity, temperature, and density in the central and southeastern Strait of Hormuz.

Figure 9 displays a vertical profile from west to east across the central Strait of Hormuz. The summer salinity profile shows a progressive increase with depth in the western strait, with values exceeding 40 psu in deeper layers. A clear horizontal salinity gradient from west to east is evident. In the central strait, a two-layer structure emerges: a low-salinity surface layer and a

high-salinity bottom layer, with both horizontal and vertical gradients well defined.

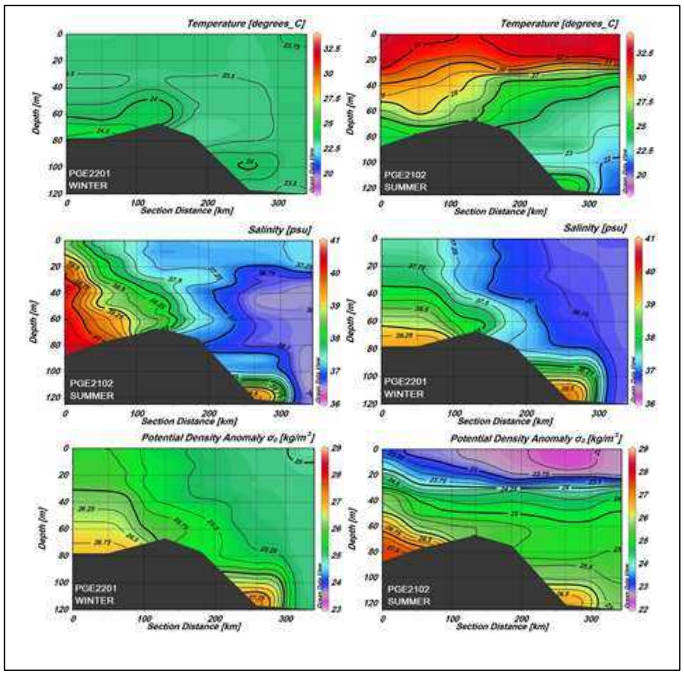

Figure 9. Plotted profiles of salinity, temperature, and potential density anomaly along transect L1 from west to east in the central part of the Strait of Hormuz

In the eastern Strait of Hormuz, a three-layer structure is observed:

- A surface layer with salinity around 37 psu
- An intermediate layer with salinity near 36.5 psu
- A deep layer with salinity exceeding 39 psu

This stratification indicates the presence of a three-layer water mass system extending from the Strait of Hormuz into the Gulf of Oman.

3.6. Potential Density Anomaly Profiles and T–S Diagrams

The vertical profile of potential density anomaly (σ_0) in the western Strait of Hormuz reveals a strong density gradient from surface to near-bottom layers, indicating pronounced water column stratification. In the central strait, a sharp pycnocline is observed at approximately 30 meters, separating low-density surface waters from denser bottom waters. In the eastern Strait of Hormuz, the structure consists of a low-density surface layer, a pycnocline at ~25 meters, and a high-density bottom layer.

The lower panel of Figure 9 presents a winter vertical profile from central eastern Persian Gulf to central western Gulf of Oman. Salinity increases significantly with depth in the eastern Persian Gulf, rising from 37.8 psu to 40 psu at 85 meters. In the Strait of Hormuz, surface salinity is around 37 psu, increasing to 38 psu near 60 meters, then slightly decreasing to 37.5 psu. A saline tongue is observed at 60 meters, extending from the central strait toward the Gulf of Oman, likely indicating intrusion of IOSW. Further into the Gulf of Oman, a saline lens exceeding 39.8 psu is detected, with strong horizontal and vertical salinity gradients, suggesting interaction between IOSW and PGW.

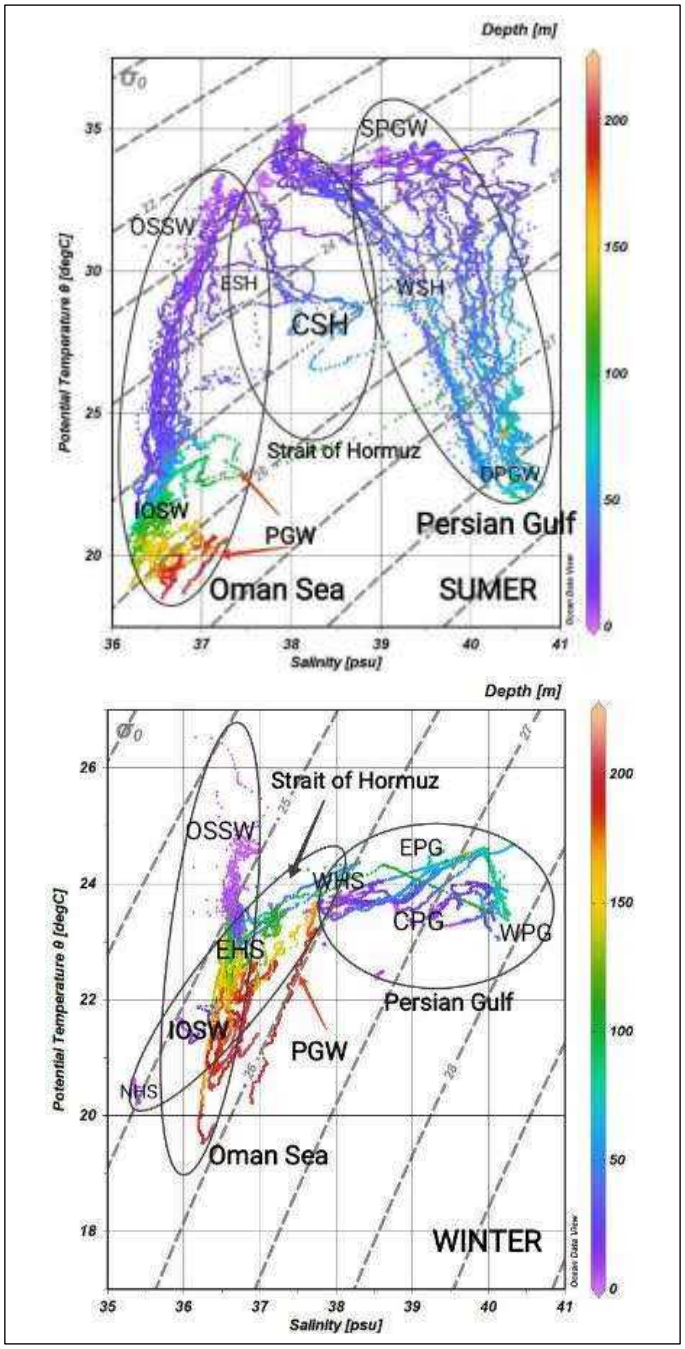

Figure 10. Temperature–salinity (T–S) diagrams for the Persian Gulf, the Strait of Hormuz and the Gulf of Oman during the summer cruise (PGE2102) and the winter cruise (PGE2201)

The temperature profile from eastern Persian Gulf to western Gulf of Oman shows uniform surface temperatures around 33.5°C. In the deeper layers of the western Gulf, temperature increases from 50 meters to the seabed, attributed to the presence of PGW. A similar temperature rise is observed at 80 meters in the eastern Strait of Hormuz, confirming PGW intrusion. This warmer water mass creates thermal inversion

zones, and due to the presence of isothermal layers, no distinct thermocline is observed.

The potential density anomaly profile from eastern Persian Gulf to western Gulf of Oman shows a surface decrease in σ_0 from 26 kg/m³ to 25 kg/m³. In the Persian Gulf, density increases with depth, peaking near the seabed in the Gulf of Oman at 27.5 kg/m³, indicating PGW presence. Toward the central Gulf of Oman, density decreases again, forming a strong horizontal gradient. PGW intrusion generates a pronounced pycnocline between 90 and 115 meters.

3.7. Temperature–Salinity (T–S) Diagrams

T–S diagrams are used to distinguish water mass characteristics. In winter, the Persian Gulf exhibits diverse thermal and salinity conditions across regions. In the northwestern Gulf (WPG), cold and highly saline waters dominate. In the central Gulf (CPG), both salinity and temperature decrease, though some stations show localized increases. In the eastern Gulf (EPG), both temperature and salinity increase with depth. In certain depressions, temperature initially rises with depth before declining, while salinity consistently increases.

In the Strait of Hormuz, northern stations (NHS) show the lowest temperature and salinity due to heavy rainfall prior to sampling. In western stations (WHS), both temperature and salinity increase with depth, though some deep layers show temperature decline. In eastern stations (EHS), salinity is lower than in the west, and temperature remains relatively constant with depth. Temperature increases with depth only in stations influenced by PGW.

In the Gulf of Oman, three distinct water masses are identified:

- Oman Sea Surface Water (OSSW): Low salinity, relatively warm (24–26°C)
- Indian Ocean Surface Water (IOSW): 21–24°C, 36–37 psu, found at 70–140 meters
- Persian Gulf Water (PGW): Very high salinity, temperature up to 24°C, found at 120–180 meters

Overall, T–S diagrams effectively differentiate regional water masses. In winter, PGW is identifiable by higher salinity and lower temperature compared to Oman Sea Water (OSW), which is warmer and less saline. Hormuz Strait Water (HSW) exhibits intermediate salinity and temperature, bridging the Gulf and the open ocean.

4. Summary and Conclusions

Comparative analysis of Persian Gulf water masses in summer and winter reveals that PGW consistently exhibits higher temperatures than surrounding waters in both seasons. In the northwestern Gulf, summer salinity is lower than in winter, while temperatures are warmer in summer and colder in winter. In winter, dense waters form in surface and deep layers of the northwestern Gulf, reaching densities above 30 kg/m³, whereas in summer, densities drop below 26 kg/m³.

Seasonal differences in the Strait of Hormuz are pronounced. In summer, a thermally and salinity-balanced zone forms between the Gulf and the Gulf of Oman. In winter, lower temperatures dominate the northern strait, while moderate temperatures persist in the south. Rainfall in the northern strait disrupts regional water properties during winter sampling.

In terms of stratification, salinity and density layering remain relatively consistent across seasons, but thermal stratification varies significantly. In summer, Persian Gulf waters are warmer than those in the Gulf of Oman, while in winter, the opposite occurs. This is due to the shallowness of the Persian Gulf, which heats and cools more rapidly than the deeper Gulf of Oman. Summer thermoclines are more pronounced in the Gulf of Oman due to its depth, though isotherm compression is stronger in the Persian Gulf. Monsoonal activity in summer enhances mixing in the Gulf of Oman and the Strait of Hormuz, leading to more moderate vertical temperature gradients compared to the Persian Gulf.Results of the work and discussions are presented here.

5. Conclusions

A comparative analysis of Persian Gulf water masses during summer and winter reveals that the Persian Gulf Water (PGW) consistently exhibits higher temperatures than surrounding waters in both the Strait of Hormuz and the Gulf of Oman. In summer, dense and saline waters form near the seabed, while fresher waters occupy the upper layers. In the Gulf of Oman, a three-layer structure emerges, consisting of Oman Sea Surface Water, Indian Ocean Surface Water (IOSW), and outflowing PGW. In contrast, the central water structure of the Strait of Hormuz is notably complex, with pronounced variations in salinity, temperature, and density across vertical layers.

During summer, potential density anomaly (σ_0) increases with depth, forming a dense bottom water mass in the Persian Gulf. In the Gulf of Oman, cooling and salinity elevation contribute to water densification. The PGW core becomes the densest feature in the southwestern Gulf of Oman, while deeper, colder waters below 150 meters further enhance density.

In both seasons, temperature elevation near the seabed in the central Gulf of Oman is attributed to PGW intrusion, which contrasts thermally with ambient waters. In the Persian Gulf, a sharp density increase between 30 and 50 meters creates a compressed pycnocline, which gradually weakens toward the Strait of Hormuz and fully dissipates in the Gulf of Oman.

In winter, PGW reaches salinity levels of 40 psu in the eastern Strait of Hormuz, a value also observed in deep, intermediate, and surface layers of the Persian Gulf. In summer, salinity exceeding 40 psu is confined to deep zones below 30 meters and the northwestern extremity of the Gulf.

Winter density anomaly values in the Gulf of Oman remain relatively stable, but increase toward the Strait of Hormuz. A two-layer structure forms in the central strait, while northern stations, influenced by local low-salinity waters, exhibit a single-layer configuration. The strongest halocline and salinity gradient are observed between 40 and 60 meters.

Thermal inversions are evident in the northern and western Strait of Hormuz during winter, while a warm tongue appears in the eastern sector, driven by PGW with elevated temperature and salinity. From east to west, a broader region of cooler surface waters is observed near the Iranian coast, extending toward the central and southwestern strait, representing the incoming IOSW.

Author contribution

Three authors contributed to this article, whose primary focus was on seasonal stratification patterns in the Persian Gulf resulting from the interaction of water masses during warm and cold seasons in the Persian Gulf and Gulf of Oman.

Acknowledgements

The author gratefully acknowledges the support of the Iranian National Institute for Oceanography and Atmospheric Science, who facilitated the execution of the Persian Gulf Explorer research cruises across the Persian Gulf and Gulf of Oman. Figures were generated using Schlitzer, R. (2021). Ocean Data View (ODV).

8. References

1. Raeisi, A., Bidokhti, A. A., Nazemossadat, S. M. J., and Lari, K. (2020). Impact of mesoscale eddies on climate and environmental changes in the Persian Gulf, *Research in Marine Sciences,* 5 (4), 823-836. https://resmarsci.com/wp-content/uploads/2020/12/Research-in-Marine-Sciences-17-5.pdf

2. Ramak H, soyufjahromi M, Akbari P. Persian Gulf Water mass tracking by surface temperature and salinity properties. joc. 2022; 12 (48):13-28 URL: http://joc.inio.ac.ir/article-1-1616-fa.html

3. Al-Hajri, K. R. (1990). *The circulation of the Arabian (Persian) Gulf: A model study of its dynamics*. The Catholic University of America. https://search.proquest.com/openview/379894904f395b1c07e4a7ad1f9bd0bf/1?pq-origsite=gscholar&cbl=18750&diss=y

4. Reynolds, R. M. (1993). Physical oceanography of the Gulf, Strait of Hormuz, and the Gulf of Oman—Results from the Mt Mitchell expedition. *Marine pollution bulletin*, *27*, 35-59. https://www.sciencedirect.com/science/article/pii/0025326X93900077

5. Pous, S. P., Carton, X., & Lazure, P. (2004). Hydrology and circulation in the Strait of Hormuz and the Gulf of Oman—Results from the GOGP99 Experiment: 1. Strait of Hormuz. *Journal of Geophysical Research: Oceans*, *109*(C12). https://agupubs.onlinelibrary.wiley.com/doi/abs/10.1029/2003JC002145

6. Azizpour, J., Siadatmousavi, S. M., & Chegini, V. (2016). Measurement of tidal and residual currents in the Strait of Hormuz. *Estuarine, Coastal and Shelf Science*, *178*, 101-109. https://www.sciencedirect.com/science/article/abs/pii/S0272771416301780

7. Hunter J. R. (1982). The physical oceanography of the Persian Gulf: a review und theoretical interpretations of previous observations. Paper presented at the First Gulf Conference on Environment and Pollution. Kuwait, 7-9 February 1982.

8. Sonu C. J., (1979). Oceanographic study in the Strait of Hormuz and over the Iranian shelfin the Persian Gulf U.S. Office of Naval Research, Final report, contract no. N00014_76+0720, Tc3675. https://apps.dtic.mil/sti/citations/ADA089144

9. Schott, G. (1918). Ozeanographie und Klimatologie des Persischen Golfes und des Golfes Von Oman. Annalen der Hydrographie und Maritirnen Meteorologic, 4&l-6. https://books.google.com/books?hl=en&lr=&id=uiwzAQAAMAAJ&oi=fnd&pg=PA1&dq=Schott,+G.+(1918).+Ozeanographie+und+Klimatologie+des+Persischen+Golfes+und+des+Golfes+Von+Oman.+Annalen+der+Hydrographie+und+Maritirnen+Meteorologic,+4%26l-6.&ots=LT0gU5JktR&sig=_s2Esb0AjL1IusJD75L2SrJRh14#v=onepage&q&f=false

10. Barlow E. W. (1932) Currents in the Persian Gulf, northern portion of the Arabian Sea, Bay of Bengal etc. I. Summary of previous knowledge. The Marine Observer, 9 (99).

11. Emery K. 0. (1956). Sediments and water of Persian Gulf. Bulletin of the American Association of Petroleum Geologists, 48 (lo), 2354-2383. https://pubs.geoscienceworld.org/aapgbull/article-abstract/40/10/2354/34178

12. Sugden, W. (1963). Some aspects of sedimentation in the Persian Gulf. *Journal of Sedimentary Research*, *33*(2), 355-364. https://pubs.geoscienceworld.org/sepm/jsedres/article-abstract/33/2/355/113017

13. SZEKIELDA, K. H., Salomonson, V., & Allison, L. J. (1972). Rapid variations of sea surface temperature in the Persian Gulf as recorded by Nimbus 2 HRIR. *Limnology and Oceanography*, *17*(2), 307-309. https://aslopubs.onlinelibrary.wiley.com/doi/abs/10.4319/lo.1972.17.2.0307

14. Purser B. H. and E. Seibold, (1973). The principal environmental factors influencing Holocene sedimentation and digenesis in the Persian Gulf. In: The Persian Gulf,

Holocene carbonate sedimentation and digenesis in a shallow epicontinental sea, B. H. Pursur, editor, Springer-Verlag, Berlin, pp. l-9. https://link.springer.com/chapter/10.1007/978-3-642-65545-6_1

15. Grasshoff K. (1976). Review of hydrographical and productivity conditions in the Gulf region in Marine Sciences in the Gulf Area. UNESCO Technical Papers in Marine Science, 26, pp. 39-62. https://ci.nii.ac.jp/naid/10006584248/

16. Sewell, R. B. (1934). The John Murray Expedition to the Arabian Sea. *Nature*, *133*(3351), 86-89. https://ui.adsabs.harvard.edu/abs/1934Natur.133...86S/abstract

17. Emery, W. J., & Meincke, J. (1986). Global water masses-summary and review. *Oceanologica acta*, *9*(4), 383-391. https://archimer.ifremer.fr/doc/00110/22090/19731.pdf

18. Duing W. and P. K. Koske, (1967). Hydrographic observation in the Arabian Sea during the N.E. monsoon period 1964-1965. "Meteor" Forschungsergebnisse A, 8, l-43

19. Duing W. and W. D. Schwill, (1967). Spreading and mixing of the highly saline water of the Red Sea and the Persian Gulf. "Meteor" Forschungsergebnisse A, 8,44-66.

20. Dabestani M, MOHAMMAD MAHDIZADEH M, Azizpour J. Comparison of surface salinity of Persian Gulf water using field data and FVCOM numerical model. joc. 2020; 11 (43):81-87 http://joc.inio.ac.ir/article-1-1602-en.html

21. Emery, W. J., & Meincke, J. (1986). Global water masses-summary and review. *Oceanologica acta*, *9*(4), 383-391. https://archimer.ifremer.fr/doc/00110/22090/19731.pdf

22. Hunter J. R. (1983). Aspects of the dynamics of the residual circulation of the Persian Gulf. In: Coastal oceanography, M.G. Gade, A. Edward and H. Svendsen, editors. Plenum Press, New York, pp. 31-12. https://link.springer.com/chapter/10.1007/978-1-4615-6648-9_3

23. Schlitzer, R. (2021). Ocean data view. http://www.vliz.be/imisdocs/publications/360848.pdf#page=169

24. Swift, S. A., & Bower, A. S. (2003). Formation and circulation of dense water in the Persian/Arabian Gulf. *Journal of Geophysical Research: Oceans*, *108*(C1), 4-1. https://agupubs.onlinelibrary.wiley.com/doi/abs/10.1029/2002JC001360

25. Thoppil, P. G., & Hogan, P. J. (2010). A modeling study of circulation and eddies in the Persian Gulf. Journal of Physical Oceanography, 40(9), 2122-2134. https://journals.ametsoc.org/view/journals/phoc/40/9/2010jpo4227.1.xml

26. Yao, F., & Johns, W. E. (2010). A HYCOM modeling study of the Persian Gulf: 1. Model configurations and surface circulation. Journal of Geophysical Research: Oceans, 115(C11). https://agupubs.onlinelibrary.wiley.com/doi/abs/10.1029/2009JC005781